HIGH-POWER, COAXIAL VIRCATOR GEOMETRIES

by

KEVIN SCOTT WOOLVERTON, B.S.E.E., M.S.E.E.

A DISSERTATION

IN

ELECTRICAL ENGINEERING

Submitted to the Graduate Faculty
of Texas Tech University in
Partial Fulfillment of
the Requirements for
the Degree of

DOCTOR OF PHILOSOPHY

Approved

Accepted

May, 1998

TABLE OF CONTENTS

ABSTRACT

High-power microwave research is an area that has been of interest due to its applicability in an ever-increasing range of fields. Virtual cathode oscillators (vircators) are devices capable of producing microwaves at levels above 1 giga-watt (GW) for short duration, less than a micro-second, and have been used in military applications, by universities as research tools in high-energy physics experiments and more recently, high-power microwaves are beginning to be used in commercial applications. Conventional vircators are broadband, usually containing many modes, and very inefficient, with efficiencies around one to two percent.

The vircator at Texas Tech University is a coaxial geometry believed to be able to increase the efficiency. Previous work on the coaxial vircator has shown promising possibilities and the current research is aimed at understanding the physics of the coaxial vircator to be able to increase the efficiency. The work at Texas Tech involved making changes that kept the device simple in its operation while increasing the effectiveness of its operation. The changes made on the device were changes on the diode and included the testing of various screen materials, placement of collection rods on-axis in the diode, placement of a hole on axis in the center of the anode base, various voltages applied to the diode, and variations of the size and position of the emitting material.

Numerical simulations were first performed to test a wide variety of geometries and see how the vircator functioned with the changes made without having to physically perform the experiments. MAGIC, a 2½-dimensional particle-in-cell code, was the tool used in the numerical simulations. From these simulations, a set of test geometries were implemented on the vircator at Texas Tech, for a total of eleven geometries at two different operating voltages.

Through these experiments, the operation of the coaxial vircator became better understood. The results showed that the highest power microwaves could be obtained with narrow emitting surfaces. Microwave levels close to 3 GW were obtained at a power efficiency of 13 %. With the understanding gained, future improvements may be made that could increase the output power and efficiency even further.

LIST OF TABLES

LIST OF FIGURES

CHAPTER 1
INTRODUCTION

Virtual cathode oscillators, commonly called vircators, are high-power microwave sources based on the bremsstrahlung radiation of relativistic electrons oscillating in electrostatic fields and are important microwave sources due to their simplicity and the fact that no external magnetic field is required for their operation. They require no heavy external coils with high-current power supplies, no complex slow wave structure and require no critical timing of magnetic sources. Vircators have also been shown to be tunable over a range of about two octaves and able to be phase locked. The main drawback to vircators is their low efficiency of beam power to microwave power, 2% for vircators with axial extraction and 0.6% for vircators with transverse extraction [1].

Even though vircators have low efficiencies, they have the advantage of being rugged, not requiring much maintenance, and do not require critical timing of magnetic sources. Vircators often work the first time they are put together and tested. The output microwave power is high, in the hundreds of megawatts to gigawatts range for a single pulse with pulse lengths up to a microsecond, and can be used for many applications, such as window breakdown experiments, high energy particle accelerators, and electronic warfare to name a few. These advantages often outweigh their disadvantage of low efficiency and they are used as a microwave source for many experiments. Hence, much of the research on vircators has been aimed at understanding the physical basis of their operation so as to be able to increase the efficiency.

The virtual cathode is formed by exceeding the space charge limiting current, resulting in a depressed electrostatic field which is large enough to overcome the kinetic energy of incoming electrons. The electrons decelerate giving up energy to the microwave field. Then the electrons are accelerated away from the virtual cathode back toward the anode and toward the real cathode in a process called reflexing. This reflexing continues and produces microwaves at a frequency proportional to the square root of the applied potential and inversely proportional to the anode-cathode gap spacing. But this is not the only mechanism for microwave production. When the virtual cathode

forms, it changes in potential and position, which is another mechanism of microwave production. This occurs at the plasma frequency of the virtual cathode.

The original vircators studied were in geometries with flat cathode emitters and flat, semi-transparent anodes called planar vircators. The beginning experiments on the planar geometry were aimed at modifying the vircator in an attempt to increase the efficiency. Figure 1.1 shows various planar geometries that have been investigated. In a planar geometry when the virtual cathode electron magnitude is large, electrons accelerated toward the virtual cathode, get repelled and oscillate in the region near the anode. This starves the virtual cathode and the number of electrons in the virtual cathode decreases. When the virtual cathode electron magnitude is lower, fewer electrons are repelled, allowing the electron beam to propagate past the virtual cathode, hence bunches of electrons are lost every cycle of the virtual cathode giving it a low efficiency. If these electrons could be recovered, efficiency could be improved. The coaxial vircator on the other hand provides a built-in mechanism for electron recovery which should increase the efficiency.

It is believed that vircators produce microwaves by two mechanisms, one is the action of the electrons reflexing between the real and virtual cathodes and the other is from the change in position of the virtual cathode and the magnitude of electrons in the virtual cathode. Some experiments, in an attempt to increase the efficiency, prevent one form of microwave production and let the other dominate. The reditron, Figure 1.1c, is an example. The reditron possesses a thick anode and any electron incident upon it, and not the holes, would get collected and not propagate through. The electron beam would pass through the holes in the anode and an axial magnetic field would then guide the electrons away from alignment with the holes and be collected in the anode or the walls of the device, thus eliminating the reflexing and the microwaves produced from it. Reported efficiencies from the reditron range from 5.5 to 6.0 percent [1].

The reflex triode, Figure 1.1d, is a planar vircator geometry with an electron near the virtual cathode at a potential close to the potential of the cathode. In Figure 1.1d, the wall has the same potential as the cathode. Didenko reported a 46% efficiency which is much larger than the efficiencies claimed by experimenters in the U.S. using the other

geometries. It has been suggested that Didenko's method of measurement is inaccurate and it is really about 3 to 5% efficient [1]. A recent machine derived from the vircator and with high efficiency is the virtode. A schematic of the virtode is shown in Figure 1.2 and has reported efficiencies as high as 17% at microwave powers of 600 MW [2].

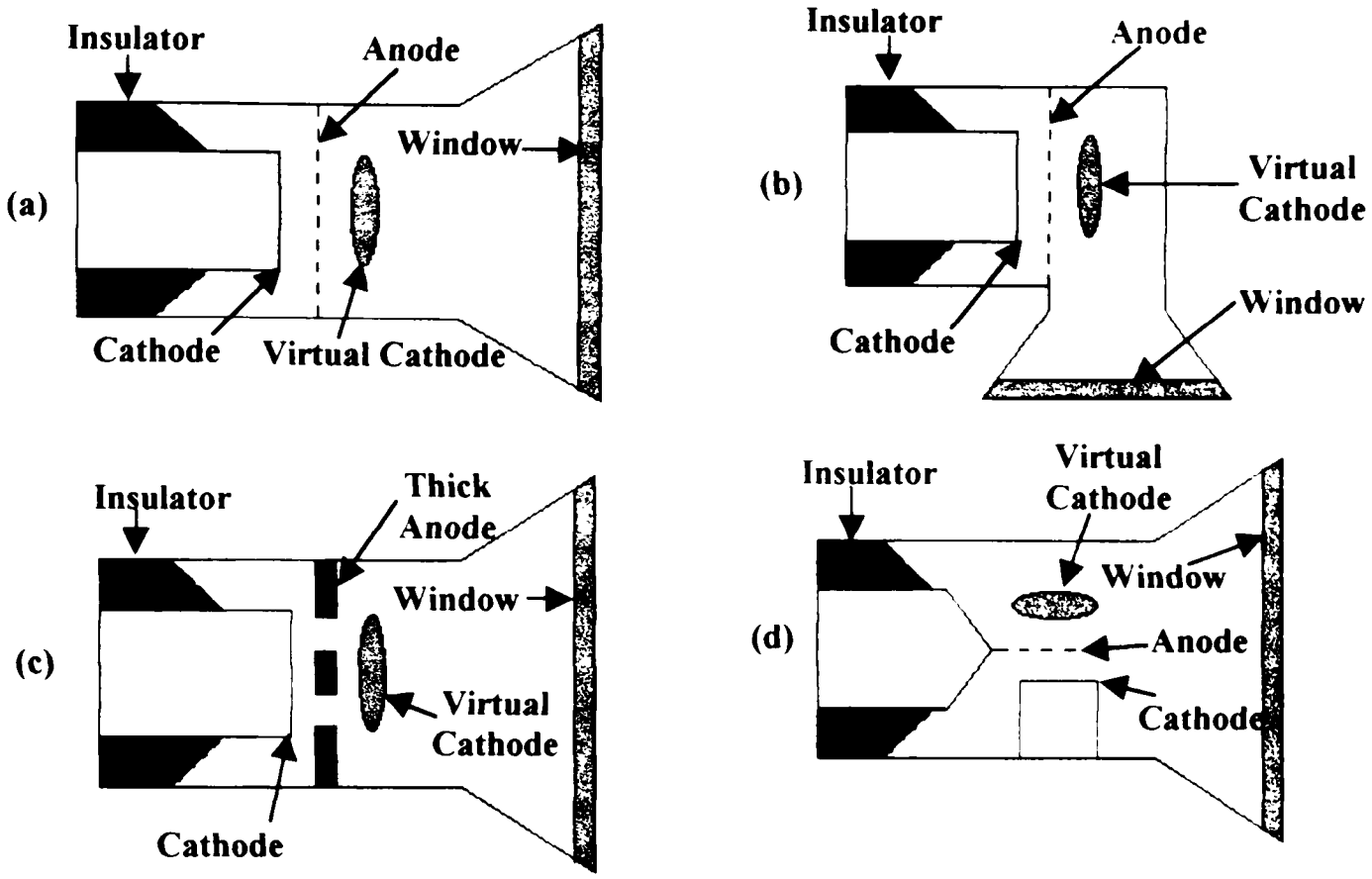

Figure 1.1. Planar Vircator Geometries. (a) axially extracted vircator, (b) transverse extracted vircator, (c) reditron, (d) reflex triode

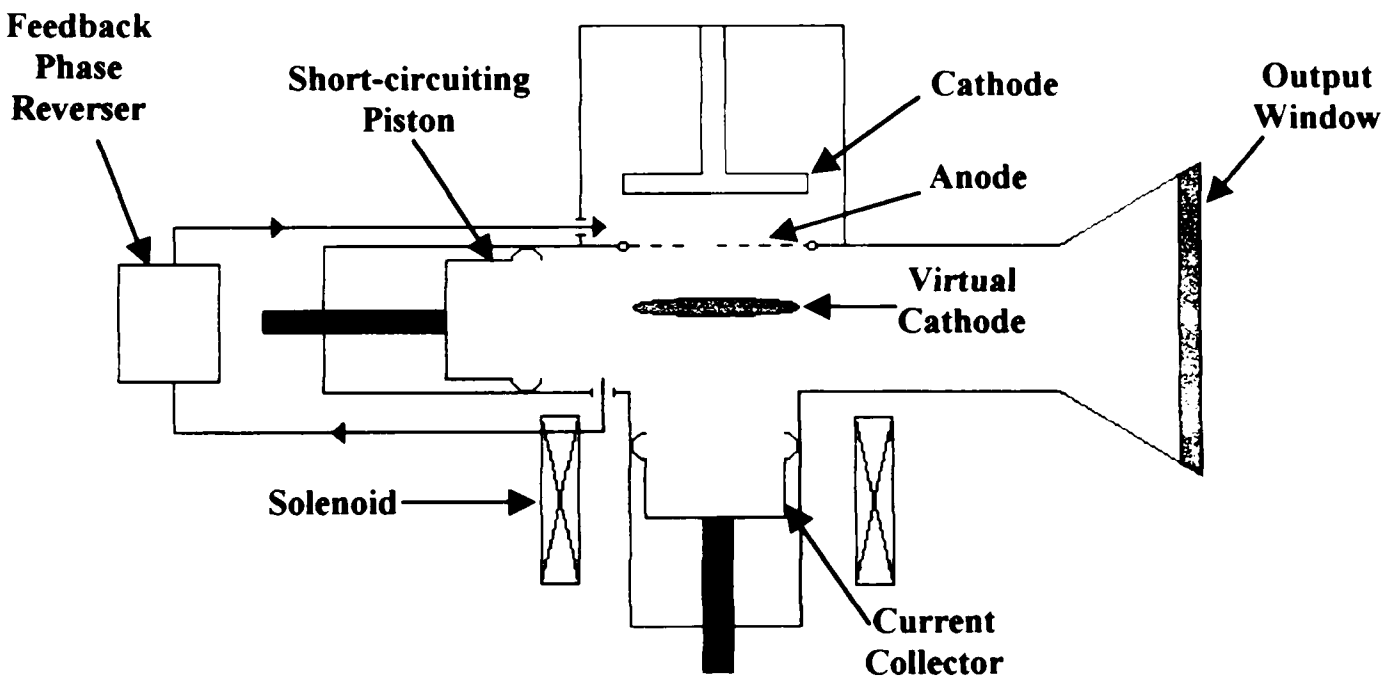

Figure 1.2: Schematic of the Virtode

The virtode operates by extracting some of the radiated microwave power and feeding it back into the acceleration region. The microwave signal fed back into the acceleration region causes the electron beam to become modulated at the oscillation frequency of the virtual cathode, which increases the gain. The modulation of the electron beam in the virtode plays the same role as cavities in other microwave devices. A tuning plunger controls the phase of the signal fed back into the acceleration region.

The coaxial vircator has a geometry similar to the reflex triode, twisted to a cylindrical form. It was believed that the coaxial vircator might have the ability to produce high efficiencies like the planar reflex triode. Initial studies of the coaxial vircator at Texas Tech University showed power efficiency results below one percent but still showed promise as a high power microwave source and the study was continued. Later studies, however, produced power efficiencies as high as 13%. The research performed was aimed at studying the operation of the coaxial vircator to gain an understanding of how it works and then make changes to the diode region to increase the microwave output, raising the efficiency.

The next chapter contains the theory of operation for the coaxial vircator at Texas Tech University. Radiation produced from the coaxial vircator is also analyzed and characterized. Then the hardware of the coaxial vircator is illustrated. Finally, the diode region and its geometry parameters are specified.

Chapter 3 contains the simulation results on the vircator under investigation. The inclusion of bipolar flow in the simulations is also described. MAGIC, a 2.5 dimensional, particle-in-cell code is used to simulate the various geometries and changes to the original geometry. From these simulations, geometries were obtained that were believed to be able to produce an increased efficiency.

After the test geometries were established from the simulations, the tests were performed. Diagnostics are a very important aspect of the tests performed and are described in Chapter 4 with the results from the experiments given in Chapter 5. Finally, Chapter 6 gives conclusions and suggestions for future studies.

CHAPTER 2
EXPERIMENTAL SYSTEM

2.1 Coaxial Vircator Theory

The vircator is a high-power microwave device unlike any other. The driving mechanism for vircators is the requirement that the space charge limited current flow, in the diode region, must be exceeded. The space charge limiting current is the current where the potential energy of the virtual cathode exceeds the kinetic energy of the beam, causing any new electrons to be reflected back towards the cathode. The diode region of the experiment at Texas Tech is shown in Figure 2.1. The cathode of the diode is covered with velvet that acts as an explosive emitter and the anode is covered with various semi-transparent materials that allow a large portion of the electrons to pass through. Stainless steel, mesh screen and aluminum foil are common materials for the anode.

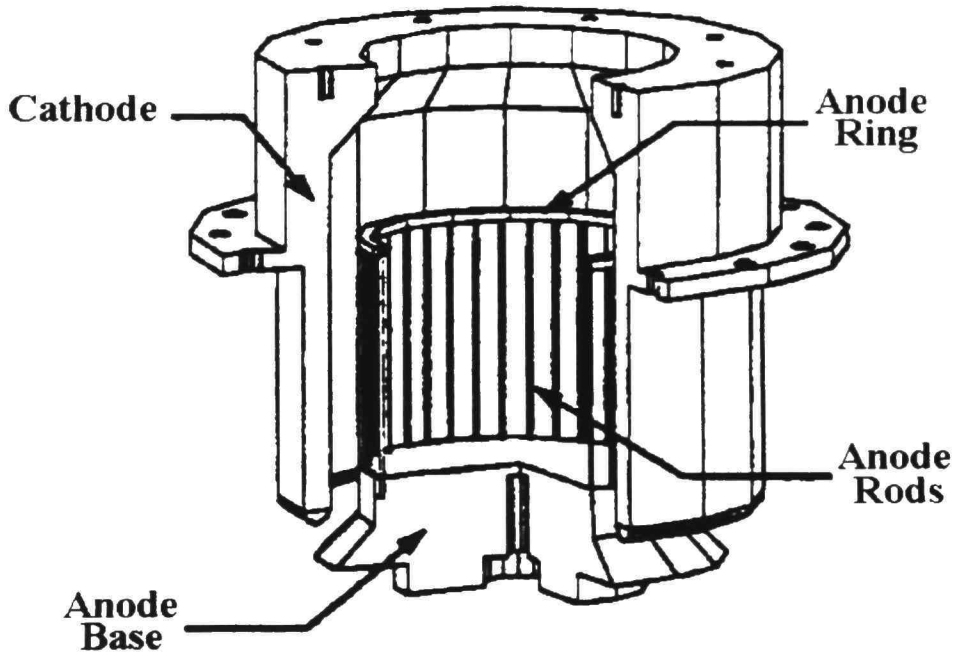

Figure 2.1: Diode Region

In vircators, the mechanism for electron beam generation is by an explosive field emission process. Field emission was originally studied by Fowler and Nordheim in 1928. Their study was on the tunneling of conduction electrons through the potential barrier at a flat metal surface. They found that an application of an external field at the

surface causes the width of the potential barrier to decrease, which enabled electrons to tunnel through the barrier more easily [3]. The estimated electric field required for electrons to tunnel through a typical barrier of 1 nano-meter width is approximately $3x10^7$ V/cm [4]. But this flat, smooth surface is not a realistic picture of real surfaces. Typical surfaces, at the microscopic level, are rough with many microprotrusions. Figure 2.2 shows the geometry at the microscopic level.

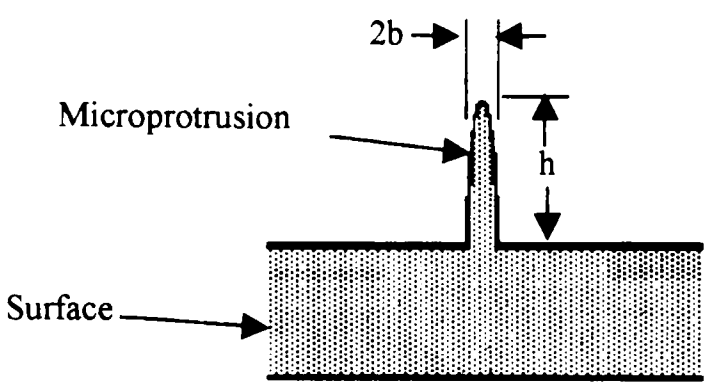

Figure 2.2: Microscopic Microprotrusion

With the application of a large voltage, the field lines converge on the tip of the microprotrusion, enhancing the localized fields, enabling electrons to tunnel through the decreased width of the potential barrier. The localized electric field at the tip can be expressed as:

$$E_{local} = fE, \tag{2.1}$$

where f is the field enhancement factor and E is the electric field in the absence of microprotrusion. The field enhancement factor for the example shown in Figure 2.2 can be written as [5]:

$$f = \frac{\left(\lambda^2 - 1\right)^{1.5}}{\lambda \ln\left[\lambda + \left(\lambda^2 - 1\right)^{\frac{1}{2}}\right] - \left(\lambda^2 - 1\right)^{\frac{1}{2}}}, \tag{2.2}$$

where λ=h/b ($\lambda > 1$) as seen in Figure 2.2.

With the beginning of field emission, the flow of these tunneling electrons increases the temperature of the microprotrusion due to Joule heating and eventually

melts the whisker into a vapor state. This vapor state quickly ionizes and creates plasma flares close to the microprotrusion. The individual flare quickly expands and combines with other flares that rapidly covers the entire cathode. This plasma cloud near the cathode can then be considered as an electron source with a work function of zero. The applied field extracts electrons and accelerates them across the diode gap. The amount of electrons extracted is limited by the space charge limiting current. Analytical equations for the space charge limited current for a coaxial geometry given was given by Langmuir and Blodgett [6] as:

$$J_{sc} = \frac{2\sqrt{2}}{9}\sqrt{\frac{e}{m}}\frac{V^{\frac{3}{2}}}{r\beta^2} \quad , \tag{2.3}$$

where J_{sc} is the current per unit length, e is the charge of an electron, m is the mass of an electron, V is the voltage at a point of observation, and r is the radius at the observation point. The factor β is a geometrical correction factor and was tabulated by Langmuir and Blodgett for various ratios of anode to cathode and also cathode to anode radii [6]. To use the formula to calculate the space charge limited current for the coaxial vircator, the voltage and radius must be known. Since the virtual cathode forms somewhere inside the anode, the space charge limited current can not be calculated, but with the aid of simulations, it can be found.

The virtual cathode, a cloud of bunched electrons, is formed by the space charge limiting current being exceeded, resulting in a depressed electrostatic field which causes incoming electrons to decelerate giving up their kinetic energy to the microwave field. Then the electrons are accelerated away from the virtual cathode back toward the anode and toward the real cathode in a process called reflexing. The reflexing frequency was calculated for a one-dimensional model and is given by [7]:

$$f_{reflex} = \frac{c}{2\pi d}\cosh^{-1}(\gamma) \quad , \tag{2.4}$$

where c is the speed of light, and d is the anode-cathode gap distance. The relativistic factor, γ, is given by:

$$\gamma = 1 + \frac{eV}{mc^2} \quad , \tag{2.5}$$

where c is the speed of light, e and m are the charge and mass of an electron, respectively, and V is the applied potential.

The plasma frequency is the second mechanism for microwave production. In the planar geometry, the pulsating potential of the virtual cathode associated with the plasma frequency allows electrons to be lost when the virtual cathode potential is low, which decreases the efficiency. The coaxial vircator on the other hand provides a built-in mechanism for electron recovery, which it was believed would increase the efficiency. But the electrons that propagate inward past the virtual cathode in the coaxial geometry have been termed wrong-phased electrons and decrease the efficiency. Phase separation for vircators is based upon the requirements for energy transfer from an electron beam to microwave energy. These requirements are that a mechanism must exist to cause a bunching of electrons and an electric field for these electrons to pass through such that the phase of the electric field slows down the bunch of electrons. The electrons that are in the correct phase and are slowed down by the electric field are termed right-phased electrons and those electrons that are accelerated are termed wrong-phased electrons. These wrong-phased electrons cause a decrease in the microwave output power, since energy must be used to accelerate the electrons away from the virtual cathode.

The pulsating frequency of the virtual cathode is the plasma frequency of the virtual cathode and is given by [1]:

$$f_{plasma} = \frac{1}{2\pi}\sqrt{\frac{ne^2}{\gamma m\varepsilon}} \quad , \tag{2.6}$$

where n is the electron beam density, e and m are the charge and mass of an electron, respectively, γ is the relativistic factor, and ε is the permittivity. Though this is

the form of the plasma frequency, it is not exact for a vircator. One dimensional, diode models have been used to find a range of values for the plasma frequency of a virtual cathode. The range of values is given by [8]:

$$\sqrt{\frac{3}{8}}\pi f_{plasma} < f_{plasma} < \sqrt{\frac{108}{200}}\pi f_{plasma} \qquad (2.7)$$

This sets a range of values for the frequency of the virtual cathode between $1.924 f_{plasma}$ and $2.309 f_{plasma}$.

Since vircators have two frequencies of operation, a reflexing and a plasma frequency, an optimum design for any vircator is to have the operation occur where these two frequencies match. For the coaxial vircator at Texas Tech University, geometry parameters are input into the two frequency equations, Equations (2.4) and (2.7), and a plot of the two frequencies as a function of applied potential is shown in Figure 2.3. In this calibration, the impedance is taken as constant which is approximately true for a given geometry.

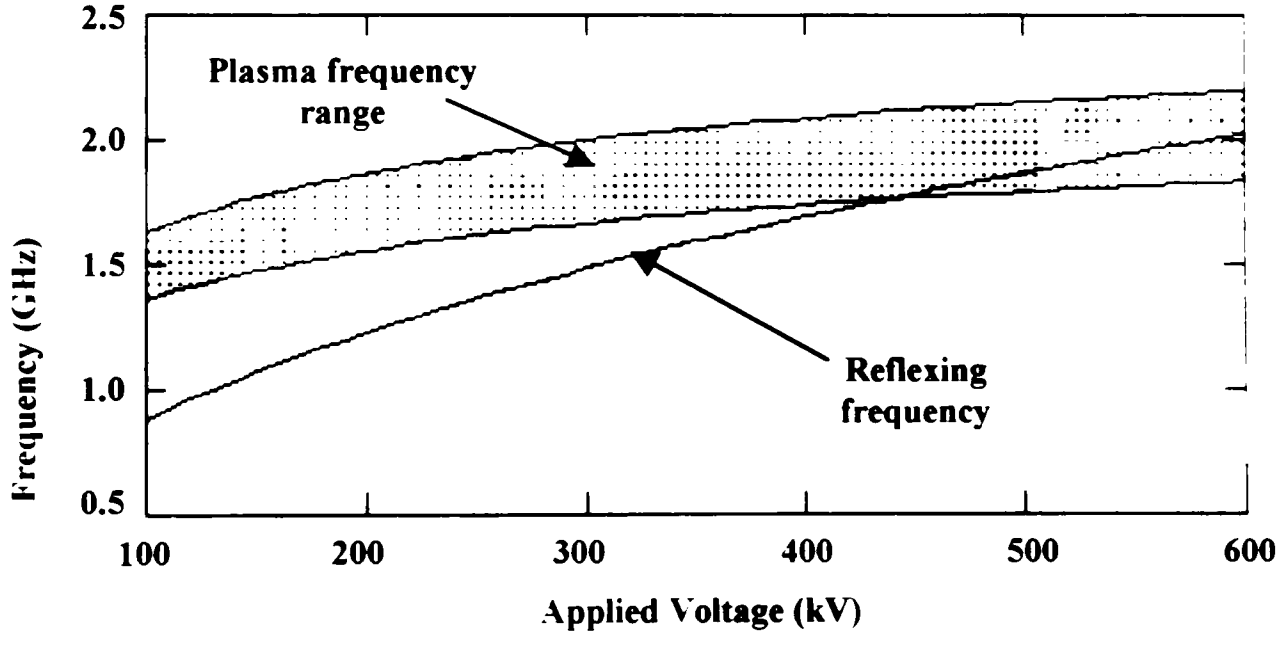

Figure 2.3: Vircator Frequencies vs. Applied Voltage

Experiments were performed on the vircator at Texas Tech to allow the determination of the plasma and reflexing frequencies with the aid of the graph in Figure 2.3. If, for example, we are on the lower plasma frequency curve in Figure 2.3, we could apply a potential of about 550 kilovolts and obtain, from Figure 2.3, a plasma frequency of about 1.82 gigahertz and a reflexing frequency of about 1.95 gigahertz. If the

geometry and the source allow two different modes at these frequencies, we should see two frequency spikes for the two modes in an FFT of the radiated field, one mode at the plasma frequency and another mode at the reflexing frequency. Two groups of frequencies from a carefully aligned diode are seen in Figure 2.4. The values of the group of frequencies do not exactly match the values in Figure 2.3 but are close. Many differences between the actual device and the equations modeling the device exist and it would be surprising if they matched exactly.

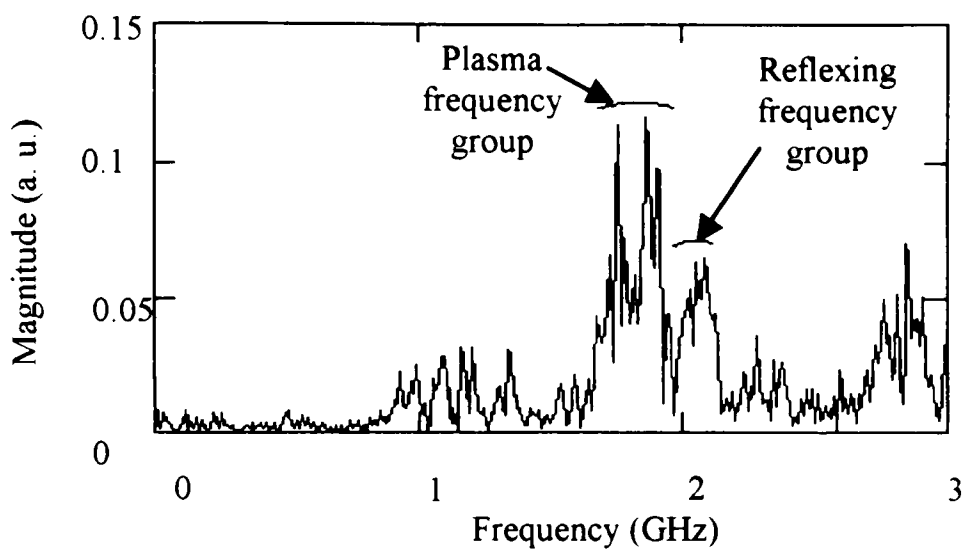

Figure 2.4: FFT Showing Plasma and Reflexing Frequencies (V = 550 kV)

The applied voltage was then lowered in steps of approximately 20 kilo-volts down to a level of about 425 kilo-volts. The resultant FFT of the various voltage levels showed only the two groups of frequencies. As the voltage was decreased, the magnitude of the FFT peak of the higher frequency decreased until it completely disappeared. Since the frequency did not shift but remained fixed, it indicated that these are resonant frequencies, or close to the resonant frequencies of the geometry. The FFT where the two frequencies match is shown in Figure 2.5.

The reason the reflexing frequency eventually disappears can be seen in Figure 2.3. As the applied voltage decreases, the reflexing frequency decreases to a value larger than the plasma frequency but smaller than before, and since the goemetry has two resonant frequencies, power begins to shift to the lower resonant frequency from the higher resonant frequency as the applied voltage decreases. The plasma frequency, over this range of potentials, remains approximately constant. Eventually, the plasma and reflexing frequencies matched. A direct consequence of this is a higher output for a

lower applied voltage and this can be seen in the relative magnitudes of the FFTs in Figures 2.4 and 2.5.

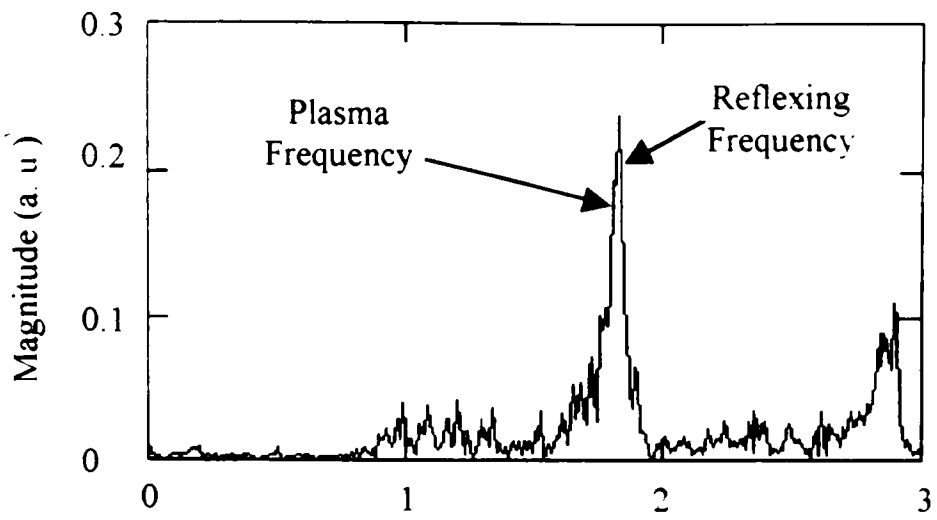

Figure 2.5: FFT with Matching Plasma and Reflexing Frequencies (V = 425 kV)

This shows that it is possible to design an optimized system, where the plasma and reflexing frequencies match, with a combination of adjustments in the anode-cathode gap spacing and adjustment of the applied voltage. But in addition to these adjustments is the presence of resonant frequencies of the geometry itself. A given geometry may have frequencies that it likes to resonate at for different modes. This is what is believed to be the cause for the peaks in the FFT's. Hence, matching the resonant frequencies of the device with the plasma and reflexing frequencies is a requirement for large microwave output. The third frequency, around 2.85 giga-hertz in the FFT's, is another resonant frequency of the device and always occurred after the main pulse and only in a well-aligned diode.

The resonant frequencies of the coaxial vircator were found from cavities created by the anode screen and the virtual cathode. Figure 2.6 shows the anode region. Since the impedance of the diode is in the range of ten to twenty ohms and the wave impedance of any mode generated and being coupled into the waveguide is on the order of hundreds of ohms, reflections from the impedance mismatch will cause the diode to appear like a cavity with variable height. The cavity height will appear larger for a lower waveguide impedance, fewer reflections, and smaller for a larger waveguide impedance, more reflections. The lower limit for the height of the cavity is the length of the physical anode screen. The equation for the resonant frequency of the cavity is given by:

$$f_r = \frac{1}{2\pi\sqrt{\mu\varepsilon}}\left[\left(\frac{\chi_{mn}}{r}\right)^2 + \left(\frac{p\pi}{h}\right)^2\right]^{\frac{1}{2}} \quad , \qquad (2.8)$$

where μ is the permeability, ε is the permittivity, r is the radius of the cavity, χ_{mn} is the n^{th} zero of the derivative of the Bessel function, J_m, of the first kind of order m for a TE mode set up in the cavity or the n^{th} zero of the Bessel function J_m of the first kind of order m for a TM mode set up in the cavity, h is the height of the cavity and p is number of half cycles of the mode in the z-direction.

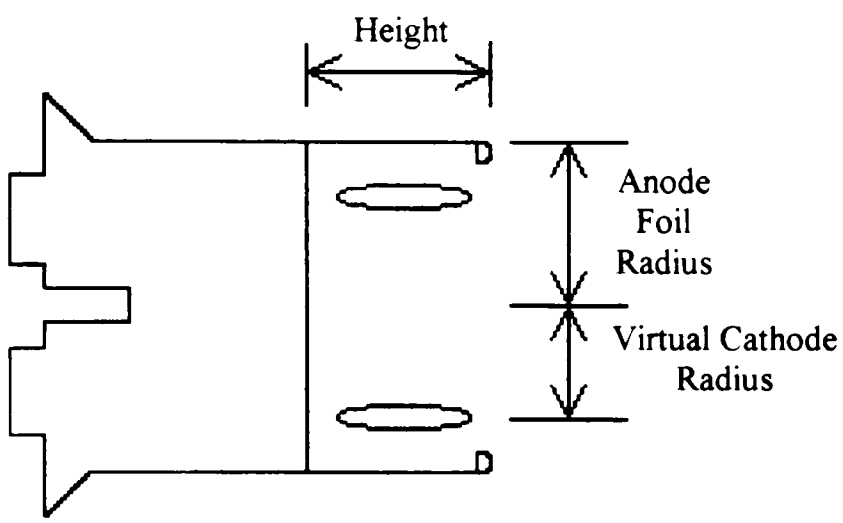

Figure 2.6: Anode Region for Resonant Frequencies

Using the height of the screen for h and the radius of the screen for r, along with p=1, in Equation 2.8 results in the resonant frequencies of 1.84 GHz for the TE_{11} and 1.99 GHz for the TM_{01} mode. These values correspond closely to the experimental frequencies seen in the FFTs. It should be noted that these values may not be exact since the height of cavity may not be exactly the height of the screen on the anode. The height may be shorter since the anode base is positively charged and draws electrons in toward the center, an effect that decreases the height and increases the resonant frequency. The height may also be larger since the impedance of the wave coupling into the waveguide does not give a complete reflection of the wave in the anode region. In addition, it will be shown in Section 4.2, however, that these are the correct modes with these approximate frequencies seen in the FFT's. The third resonant frequency was calculated

as before but since the virtual cathode appears as a conductor, the radius was taken equal to the virtual cathode radius. The mode calculated for the resonant frequency was a TE_{21} with p=1 and was found to be 2.75 GHz. This will also be shown in Section 4.2 to be the mode at the larger frequency in the FFT's.

As a verification of this cavity hypothesis, it can be seen that all experiments with the 3.5 inch size stainless steel mesh screen with a total covering of 3.5 inches of velvet opposite it produced a TE_{11} mode with a frequency around 1.84 GHz. With only partial velvet illuminating the anode screen, less than 3.5 inches, the interaction of the beam with the diode change and may not produce this frequency. Also, using different materials for the anode screen, such as aluminum, change the mode of operation and produces higher frequencies. This phenomenon has been seen before. Experiments have shown that microwave power and emission frequency are strongly influenced by the distribution of electrons over the cross section of the beam [9]. Since the aluminum foil would produce a more uniform beam cross section than a stainless steel mesh screen, the output power and efficiency could change. Still another verification of the cavity hypothesis can be found. In previous experiments at Texas Tech, a study using an anode screen of approximately twice the 3.5 inch length was performed [10]. The result was a TE_{11} mode with a frequency of approximately 1.4 GHz. Calculating the resonant frequency of a TE_{11} with these parameters results in a frequency of 1.2 GHz, which is close.

Now that the initial theory has been laid, it is important to know which mode will be produced and how a maximum output power can be created. It will be shown in the next section which mode is most likely to be produced and why the TE_{11} is being produced.

2.2 Coaxial Vircator Radiation

The radiation produced from the coaxial vircator is important for characterization of the device. The mode produced is important because different modes have different applications and the mode produced by the vircator will determine its usefulness. But in addition to this, the mode is required for calculation of the output power from the device.

Section 2.1 describes the three possible modes produced and this section describes the radiation produced from a perfectly symmetric coaxial vircator and the cause for the actual mode produced in the experiment. The procedure that follows for the theoretical derivation was originally described in Ref. [10] and is reproduced here with minor differences. The derivation, originally performed in Gaussian units, gives the shape of the radiated fields produced by the oscillating charges. It is the shape of the radiated fields that determine which mode gets coupled into the waveguide.

The geometry for the derivation of the radiation fields of a coaxial vircator is shown in Figure 2.7. In the figure, P represents the observation point, R is the distance from the center of the oscillating charge, ρ is the distance from the origin to the point P, and n is the distance from the center of the oscillating charge to point P. In the figure and all calculations, the primed spherical coordinates are for the oscillating charge and the unprimed spherical coordinates are for the observation point.

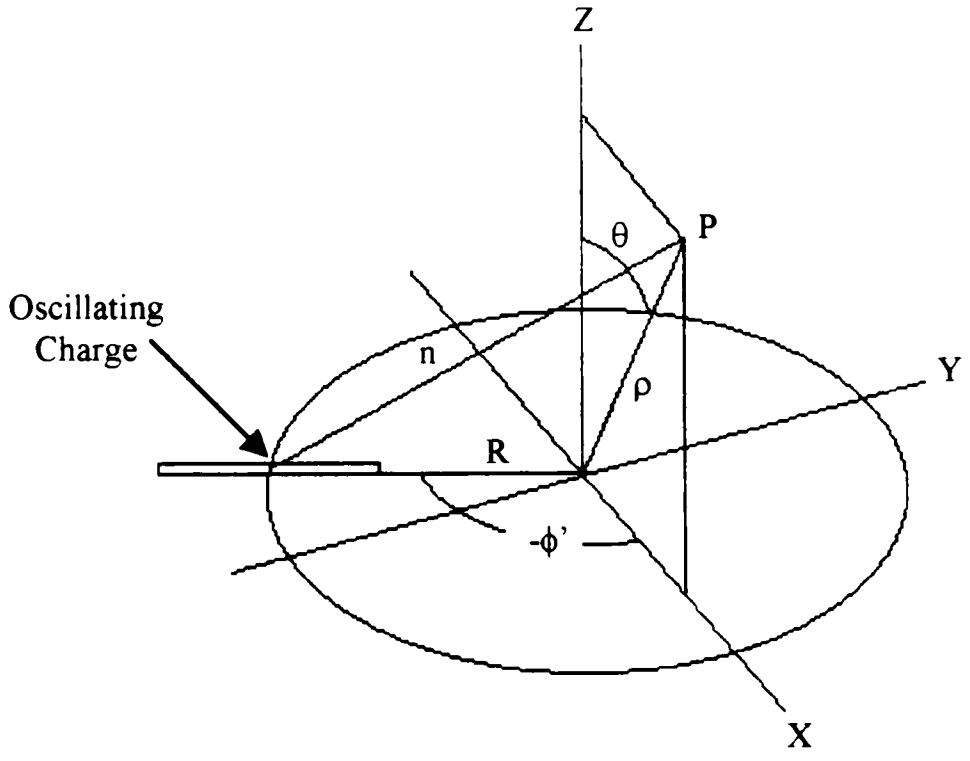

Figure 2.7: Geometry for Calculation of the Radiation from a Radially Oscillating Charge

From Jackson [11], the electric field from a nonrelativistic accelerated charge is:

$$\vec{E} = \frac{q}{c}\left[\frac{\hat{n}\times\left(\hat{n}\times\dot{\vec{\beta}}\right)}{R_r}\right]. \qquad (2.9)$$

In this equation R_r is the distance between the oscillating charge and the point of observation, c is the speed of light, q is the charge of the oscillating charge and the unit vector from the center of oscillation to the observation point is defined as:

$$\hat{n} = \frac{\vec{n}}{|\vec{n}|}, \tag{2.10}$$

where

$$\vec{n} = (R\cos(\phi') - \rho\sin(\theta))\hat{x} + R\sin(\phi')\hat{y} - \rho\cos(\theta)\hat{z} \tag{2.11}$$

and

$$|\vec{n}| = \left([R\cos(\phi') - \rho\sin(\theta)]^2 + [R\sin(\phi')]^2 + [\rho\cos(\theta)]^2\right)^{\frac{1}{2}}. \tag{2.12}$$

For a linearly oscillating charge of length d, and frequency, ω, oscillating in the x-y plane as shown in Figure 2.7:

$$\dot{\vec{\beta}} = \frac{d\omega^2}{2c}\sin(\omega t)(\cos(\phi')\hat{x} + \sin(\phi')\hat{y}) \tag{2.13}$$

Inserting Equations (2.10) and (2.13) into Equation (2.9) and solving in rectangular coordinates gives the radiated electric field:

$$\vec{E}(t) = \frac{qd\omega^2}{2c^2 R_r^{\,3}}\sin(\omega t)\begin{bmatrix} -R\rho\sin(\theta)\sin^2(\phi') - \rho^2\cos^2(\theta)\cos(\phi') \\ R\rho\sin(\phi')\sin(\theta)\cos(\phi') - \rho^2\sin(\phi') \\ \rho^2\cos(\theta)\sin(\theta)\cos(\phi') - R\rho\cos(\theta) \end{bmatrix}\begin{bmatrix} \hat{x} \\ \hat{y} \\ \hat{z} \end{bmatrix}. \tag{2.14}$$

For the given situation:

$$R_r = |\vec{n}|. \tag{2.15}$$

Accounting for the propagation time of the radiation from the oscillating charge to the observation point, we use:

$$\sin(\omega t) = e^{-j\frac{\omega}{c}R_r}. \tag{2.16}$$

Finally, a conversion to spherical coordinates is performed. Due to the symmetry of the problem, we set ϕ=0. This restricts the observation point to the x-z plane and we obtain:

$$\vec{E}(\rho,\theta,\phi') = \frac{qd\omega^2}{2c^2R_r^3} e^{-j\frac{\omega}{c}R_r} \begin{bmatrix} -R\rho\sin^2(\theta)\sin^2(\phi') - R\rho\cos^2(\theta) \\ R\rho\cos(\theta)\sin(\theta)\cos^2(\theta) - \rho^2\cos(\theta)\cos(\phi') \\ R\rho\sin(\phi')\sin(\theta)\cos(\phi') - \rho^2\sin(\phi') \end{bmatrix} \begin{bmatrix} \hat{r} \\ \hat{\theta} \\ \hat{\phi} \end{bmatrix} \quad (2.17)$$

This is the electric field from the oscillation of a single charge. If the charge is distributed evenly around a ring, similar to the reflexing mechanism in the coaxial vircator, we can integrate the differential charge in a differential section of the ring, $d\phi'$, around the complete ring to obtain the radiated electric field. For a given R and ρ, the result will be the radiated electric field patterns at the observation point in terms of the angle, θ, shown in Figure 2.7. The z-axis corresponds to the vector pointing down the waveguide in the coaxial vircator.

The purpose of finding the radiated field patterns is to determine into which mode the oscillating charges couple. Since the primary interest is the determination of the radiation pattern of the coaxial vircator at Texas Tech, parameters similar to the vircator at Texas Tech are input into Equation (2.17) and the radiation patterns numerically calculated. The parameters used are:

$R = 0.1$ m

$\omega = 12.566 \times 10^9$ (1/s), (corresponding to f = 2 GHz)

$\rho = 2R = 0.2$ m.

The values of q, d and c only scale the magnitude, so they are set to one. Figures 2.8 and 2.9 contain the polar plots of E_ρ and E_θ, respectively. The radiated field for E_ϕ was extremely small and taken to be zero.

From Jackson, the magnetic flux density can be found with:

$$\vec{B} = \hat{n} \times \vec{E}. \quad (2.18)$$

This equation says that the electric and magnetic fields are perpendicular to the direction of propagation and to each other. It also implies that the magnetic and electric fields are

equal in magnitude. Plugging Equation (2.10) and Equation (2.17) into Equation (2.18), the magnetic field components are found:

$$\vec{B}(\rho,\theta,\phi') = \frac{qd\omega^2}{2c^2 R_r^4} e^{-j\frac{\omega}{c}R_r} \vec{F}(\rho,\theta,\phi') \begin{bmatrix} \hat{r} \\ \hat{\theta} \\ \hat{\phi} \end{bmatrix} \tag{2.19}$$

where:

$$\vec{F}(\rho,\theta,\phi') = \begin{bmatrix} 0 \\ R\rho^2 \sin(\theta)\cos(\phi')\sin(\phi') - R^2\rho\sin(\phi') \\ R^2\rho\cos(\theta)\cos(\phi') - 2R\rho^2\cos(\theta)\sin(\theta)\cos^2(\phi') + \rho^3\cos(\theta)\cos(\phi') \end{bmatrix}. \tag{2.20}$$

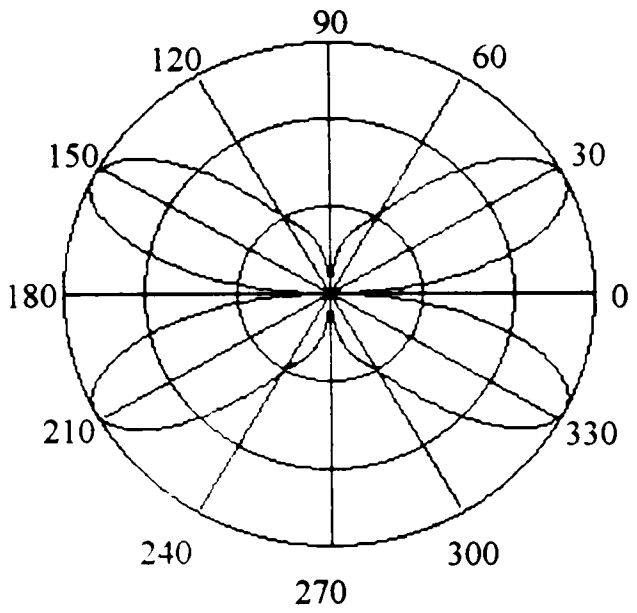

Figure 2.8: Polar Plot of E_ρ versus θ

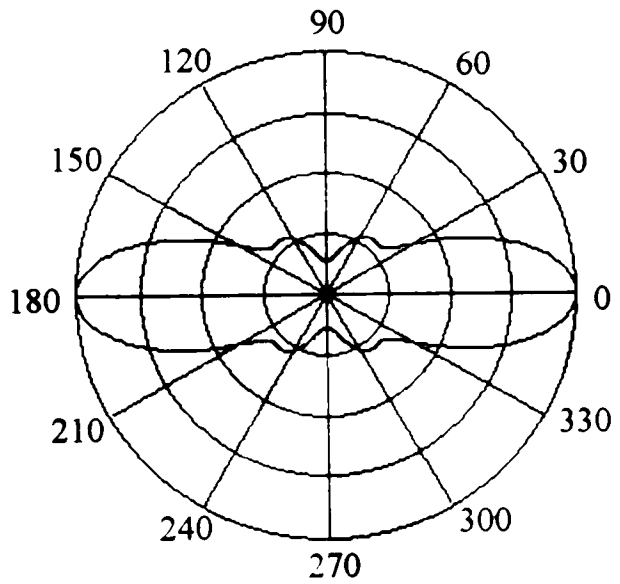

Figure 2.9: Polar Plot of E_θ versus θ

Using the same values as with the electric field calculation and performing the same integration, the magnetic field is found. The only non-zero magnetic field component is B_ϕ and is shown in Figure 2.10. These results are slightly different than those presented in Ref [10] and are presented as a correction.

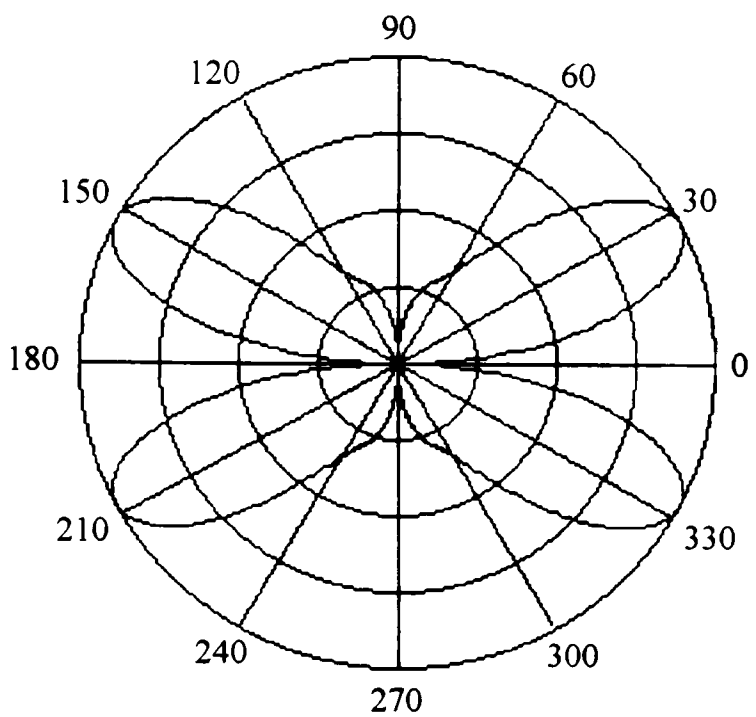

Figure 2.10: Polar Plot of B_θ versus θ

Now that the fields from a symmetric oscillating ring of charge have been found, the mode that will couple into the output waveguide on the coaxial vircator can be determined. If the source is symmetric, the beam will be symmetric and the mode produced must also be symmetric. The symmetric modes are contained in two groups, TE_{0n} and TM_{0n}. The TE modes are the modes where all electric field components are transverse to the propagation of the wave and the TM modes are the modes where all of the magnetic field components are transverse to the propagation of the wave.

If we assume that the source frequency is low enough that only the lowest modes can propagate, we restrict the possible modes to the TM_{01} and TE_{01}. This is a valid assumption since the vircator produces a dominant frequency in the range of 1.8 to 2.1 GHz, as shown in the previous section, and the cut-off frequencies for these modes are 1.17 and 1.86 GHz, respectively, for the output waveguide on the vircator. The next higher mode, the TM_{02}, has a cut-off of 2.68 GHz and will not propagate. Equations for

the field components for the TM_{01} and TE_{01} modes are shown in Table 2.1 and are also corrections to the Ref [10].

Table 2.1: Field Components for the TE_{01} and TM_{01} Modes

Field Component	TE_{01}	TM_{01}
E_ρ	0	$B_{01}\frac{\beta_\rho\beta_z}{\omega\mu\varepsilon}J_1(\beta_\rho\rho)e^{-j\beta_z z}$
E_ϕ	$A_{01}\frac{\beta_\rho}{\varepsilon}J_1(\beta_\rho\rho)e^{-j\beta_z z}$	0
E_z	0	$-jB_{01}\frac{\beta_\rho^{\,2}}{\omega\mu\varepsilon}J_0(\beta_\rho\rho)e^{-j\beta_z z}$
H_ρ	$-A_{01}\frac{\beta_\rho\beta_z}{\omega\mu\varepsilon}J_1(\beta_\rho\rho)e^{-j\beta_z z}$	0
H_ϕ	0	$B_{01}\frac{\beta_\rho}{\mu}J_1(\beta_\rho\rho)e^{-j\beta_z z}$
H_z	$jA_{01}\frac{\beta_\rho^{\,2}}{\omega\mu\varepsilon}J_0(\beta_\rho\rho)e^{-j\beta_z z}$	0

The symbols in Table 2.1 are defined as:

ρ, ϕ, z = cylindrical coordinate variables,

A_{01} = constant coefficient,

B_{01} = constant coefficient,

J_0 = Bessel function of the first kind of zero-order,

J_1 = Bessel function of the first kind of first-order,

β_ρ = radial propagation constant,

β_z = propagation constant in the z-direction,

ω = radian frequency of propagating wave,

ε = permittivity of medium of the propagating wave,

μ = permeability of medium of the propagating wave.

As shown in Table 2.1, all of the field components vary as Bessel functions of the first

kind of either the zero or first order. The graphs of these components are important in determining which mode will be coupled into the waveguide by comparing these functions with the radiated patterns shown in Figures 2.8 to 2.10. Each of the Bessel functions has the following form:

$$J_{0,1}(\beta_\rho \rho)$$

where:

$$\beta_\rho = \frac{\chi_{01}}{r}. \qquad (2.21)$$

In this equation, ρ is radial position of observation, r is the radius of the waveguide, 0.0984 meters, and χ_{01} is first zero of the respective Bessel function, 3.832 for TE_{01} and 2.405 for TM_{01}. Graphs of these functions are shown in Figures 2.11 and 2.12.

In determining which mode gets coupled into the waveguide, a comparison of the radiated waveforms and the mode's fields at comparable places is performed. In the polar plots of the radiated field, the value of $\theta = 0$ corresponds to the center of the output waveguide of the vircator. The Bessel functions at a radius of zero also correspond to the center of the output waveguide of the vircator and will be used for the comparison point.

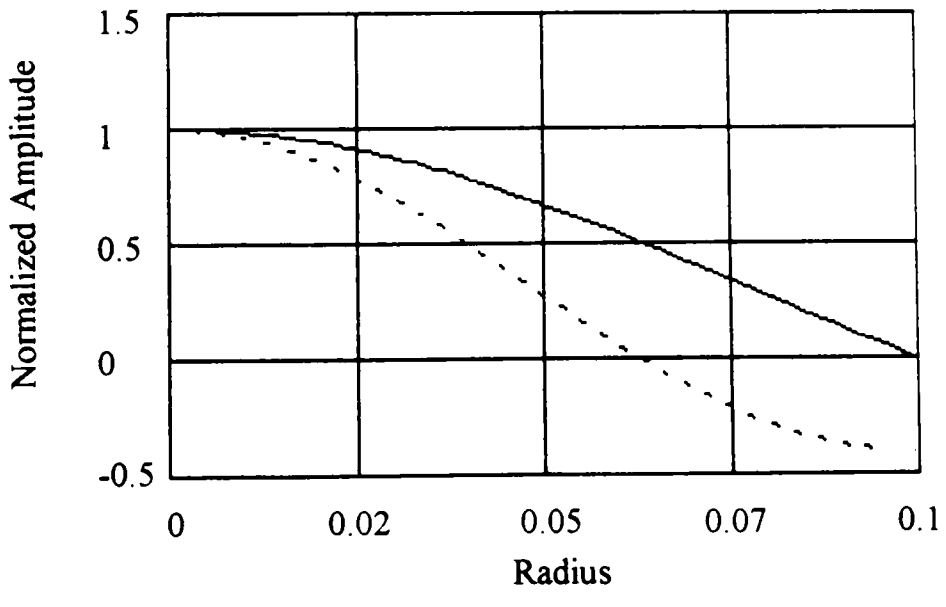

Figure 2.11: Graph of the Zero-order Bessel Function of the First Kind, solid line – TM_{01}, dashed line – TE_{01}

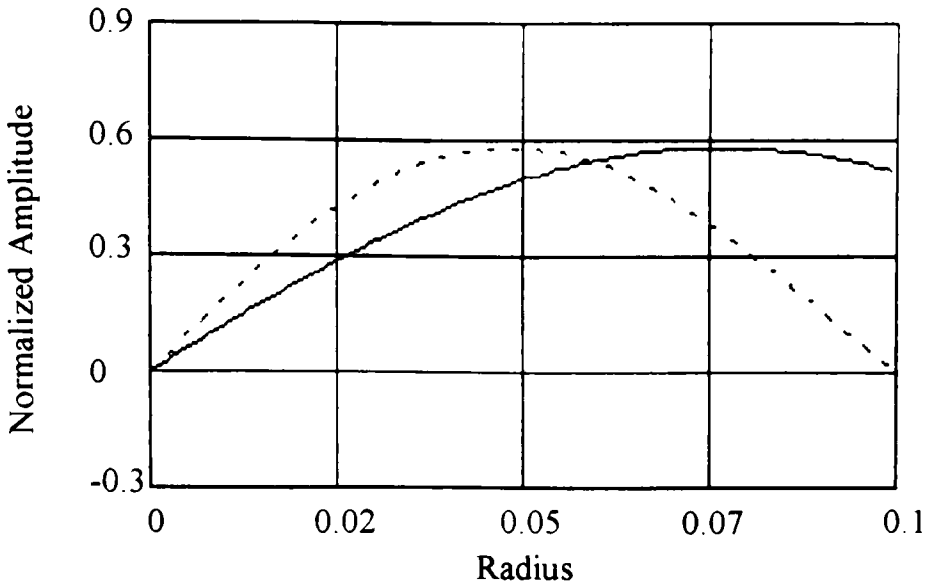

Figure 2.12: Graph of the First-order Bessel Function of the First Kind, solid line – TM_{01}, dashed line – TE_{01}

Since we are comparing the spherical values at $\theta = 0$, a direct correlation can be made between the radiated fields and the mode patterns. For small values of θ, the spherical coordinate, ρ, is approximately equal to the cylindrical coordinate, z, the spherical coordinate, θ, is approximately equal to the cylindrical coordinate, ρ, and the spherical coordinate, ϕ, remains unchanged in the cylindrical coordinate system. This allows the radiated field in Figure 2.8 at a value of $\theta = 0$ to be compared to E_z at a radius of zero in the mode patterns. Similarly, at the same point, the radiated field in Figure 2.9 is comparable to the E_ρ mode pattern and the radiated field Figure 2.10 is comparable to the H_ϕ mode pattern.

From Figure 2.8, we have a minimum at $\theta = 0$ and so we look for the mode that has a minimum at zero radius for the E_z field component. This corresponds to the TM_{01} mode. Following the same procedure in the following figures, we want minimums at zero radius for the field components of E_ρ and H_ϕ. Both of these conditions correspond to the TM_{01} mode and indicates that the mode coupled into output waveguide will be a TM_{01}.

Even though a TM_{01} is the expected mode, a TE_{11} is the generated mode. This mode is unexpected since it has an asymmetry and an asymmetry in the source is required to generate an asymmetric mode. The cause for a TE_{11} was found by measuring the gap

between the anode and the cathode with an inside micrometer. Figure 2.13 shows a representation of the distance between the anode and the cathode. The misalignment of the anode-cathode gap results in the anode being closer to cathode at certain points and further from the cathode 180 degrees opposite this point. The result for the same potential across the anode-cathode gap is a stronger electric field in the place where anode is closer to the cathode. The stronger field will result in more electrons being extracted. The opposite effect of fewer electrons being extracted will occur where the anode-cathode gap is the largest. The net result is what appears as a dipole antenna with a polarized field along the line connecting the points of high and low extraction, shown in Figure 2.13, and is the cause for the asymmetric mode being generated. In support of this, the measured polarization of the field should correspond to approximately this angle. If a probe is placed at the 180 degree point and another at the 90 degree point, shown in Figure 2.13, a polarization of 60 degrees should be obtained with the following equation:

$$\text{Polarization} = \tan^{-1}\left(\frac{\text{Probe 2 E - Field}}{\text{Probe 1 E - Field}}\right). \tag{2.22}$$

Figure 2.14 shows the measured polarization produced from the vircator. The first part of the polarization waveform, up to 55 ns, varies rapidly due to the small values of the field probes. The main microwave pulse occurs from about 55 to 105 ns. The rest of the waveform, after 105 ns, is the exponential decay. It is easily seen that the polarizations, after 55 ns, match and supports the belief that a misalignment is the cause for the TE_{11} mode. This 60 degree polarization occurred in every shot and is evidence that it is not a random process.

An attempt to re-align the gap spacing was performed. But the cathode has bolt holes slightly larger than the bolt holding the cathode and alignment can vary slightly each time the cathode is taken apart and then replaced. The deviation is small but is still enough to cause a generation of a TE_{11} mode, which is not necessarily unwanted. Since the same alignment can not be guaranteed each time the vircator is taken apart, a careful alignment is not performed.

It should also be noted that the waveforms in the previous section were from a carefully aligned anode-cathode gap with differences in the gap less than 0.5 millimeters, only a 1.5 % gap deviation. This aligned gap produced three modes, with only one mode being symmetric, the TM_{01}. A dominant mode was present at any given time, progressing in time from lower to higher ordered mode. This could be caused by the instability in the formation of the virtual cathode. Even though gap closure is minimal, the closure that does occur is significant enough to create an instability that causes a change in modes. This indicates that the modes are frequency dependent, a further indication of a resonant structure as described in the previous section. When careful alignment was not performed, only the TE_{11} mode was generated. The conclusion is that even though the TM_{01} is the natural mode for an aligned gap, a small mis-alignment has a significant effect on the mode produced. The mis-alignment of the gap causes an asymmetry in the source that forces the TE_{11} to be produced.

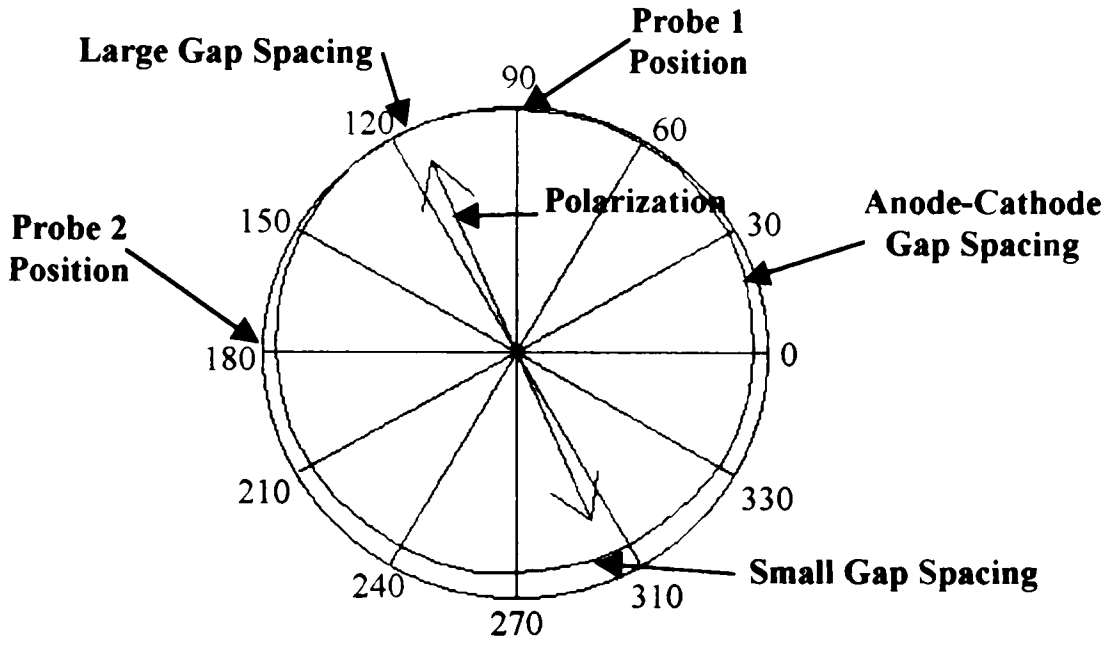

Figure 2.13: Anode – Cathode Gap Spacing

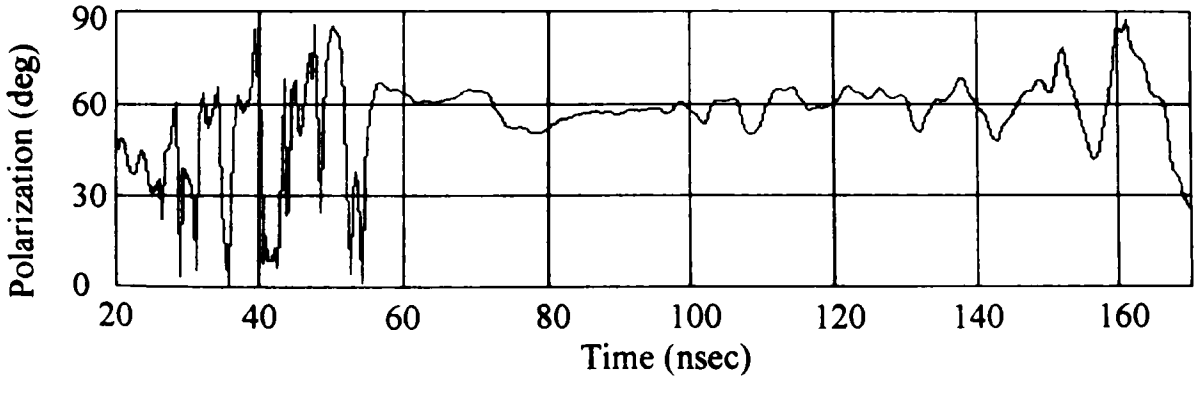

Figure 2.14: Measured Polarization from the Vircator

2.3 High Voltage Source

The coaxial vircator at Texas Tech University consists of a Marx generator connected to a 12.5 ns pulse forming line that is connected to the coaxial diode. The microwaves produced are coupled into an overmoded waveguide and then radiated into and absorbed in an anechoic chamber. Figure 2.15 shows a view of the coaxial vircator system.

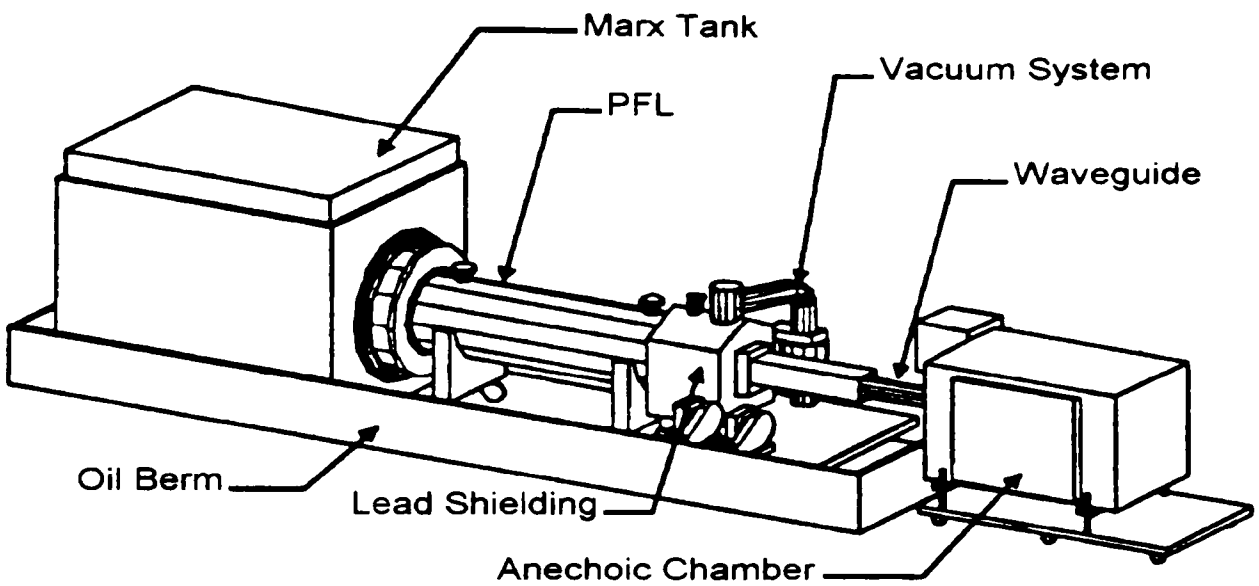

Figure 2.15: Coaxial Vircator System

The Marx bank contains 31, 0.2 μF capacitors with a maximum charging voltage of 50 kilovolts. The Marx bank is capable of storing 7.75 kJ of energy with a maximum output voltage of 1.55 MV. This energy is switched into a 10 Ω pulse-forming line (PFL) with a one-way transit time of 12.5 ns. Between the Marx bank and the PFL is a 25 μH inductor that isolates the Marx bank since it appears as a high impedance to reflected pulses. Charging the PFL through the inductor also creates a ringing voltage that is approximately 1.6 times the voltage produced by the Marx bank. At the end of the PFL is a single-channel, self-breaking oil switch that transfers the high voltage pulse to the diode region which is under vacuum. Due to the high voltages involved, the entire system up to the diode region is immersed in transformer oil which retards breakdown. Figure 2.16 is a detailed view of the coaxial vircator. Six pre-pulse resistors, each 3000 Ω, at the diode region, placed in parallel, keep the diode region near ground. Otherwise, capacitive coupling during charging of the PFL would cause the potential across the

diode to rise with the PFL preventing the single-channel switch from closing and allowing the emitter to emit prematurely. A view of the resistors and one side of the single channel, self-breaking oil switch is shown in Figure 2.17. For more detailed information, see Ref. [12].

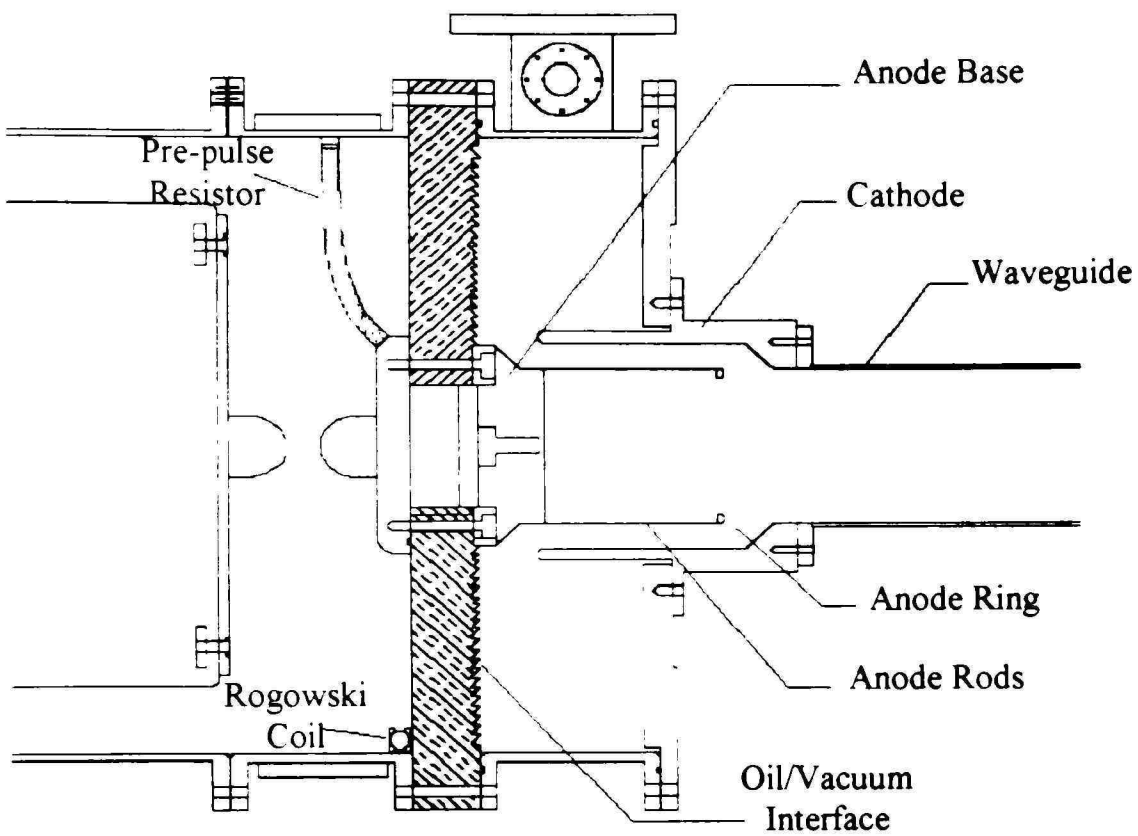

Figure 2.16: Detailed View of the Coaxial Vircator

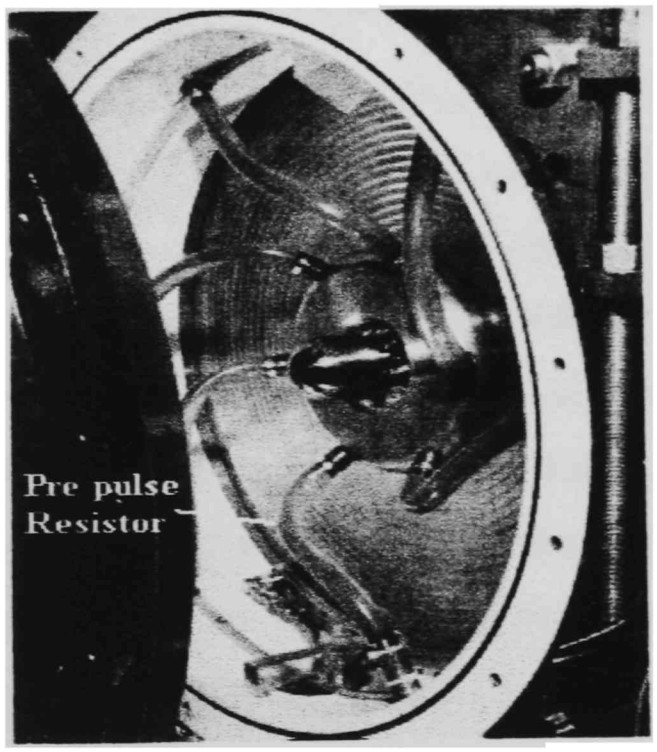

Figure 2.17: Picture of the Pre-pulse Resistor and Oil Switch Region

2.4 Coaxial Diode Region

The diode region is the most important part of the coaxial vircator. It is the part of the machine that is the conduit for transfer of beam power to microwave power. A diode is made up of a cathode and an anode. For the coaxial vircator, the cathode is a cylindrical structure with velvet covering it. The velvet acts as an explosive emitter and a diagram of the cathode is shown in Figure 2.18.

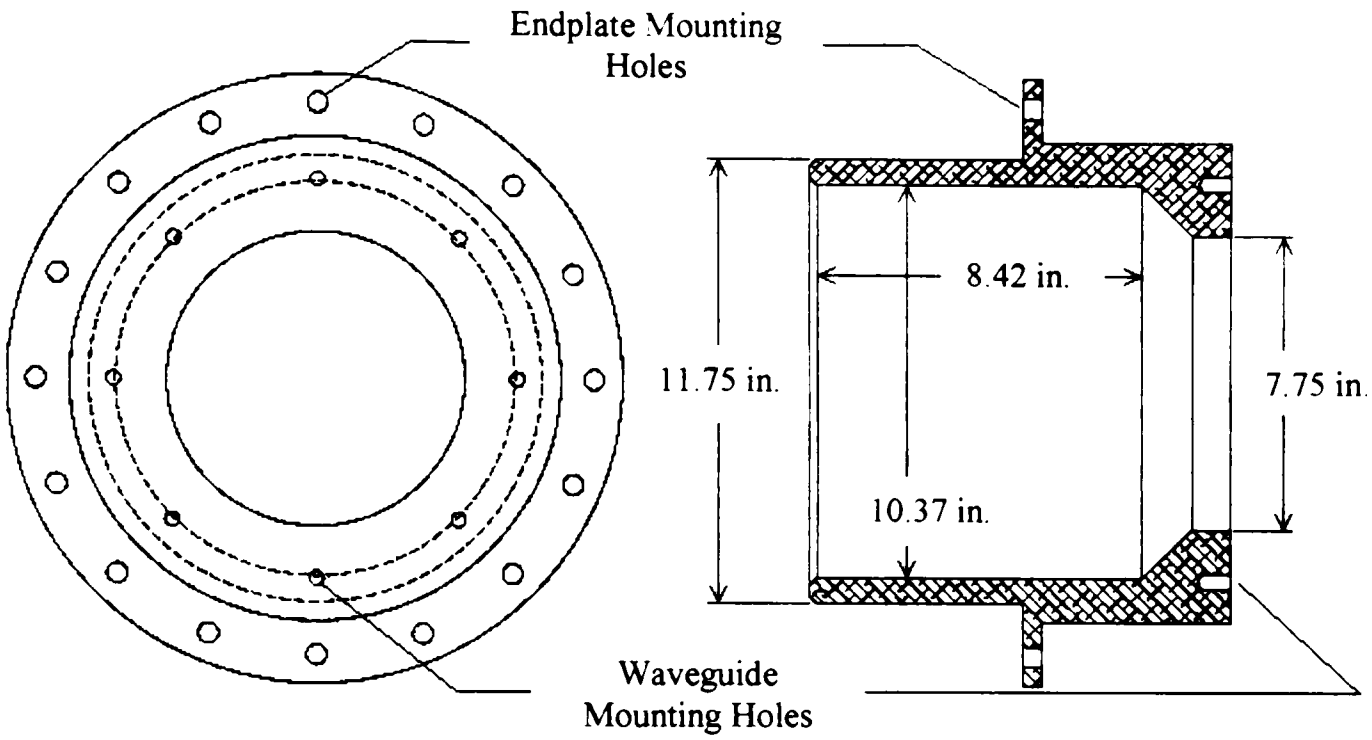

Figure 2.18: Diagram of the Cathode of the Coaxial Vircator

The anode for the geometry under experiment consists of an anode base and two spacers with the second spacer having tapped holes to screw in the 36 rods that secures a foil. The spacers are stacked on the anode base, one on top of the other. Though the anode base is capable of securing the rods by itself, previous experiments with the spacers had shown the greatest efficiencies and they were always used in the current experiments. The experiments at Texas Tech used both aluminum and stainless steel mesh screens. The stainless steel mesh screen is secured to the 36 rods with aluminum wire and the aluminum foil is secured by wrapping it around the rods and gluing the ends together. A diagram of the anode is seen in Figure 2.19, the spacers in Figures 2.20 and 2.21 and an actual picture of the diode without the spacers, is shown in Figure 2.22.

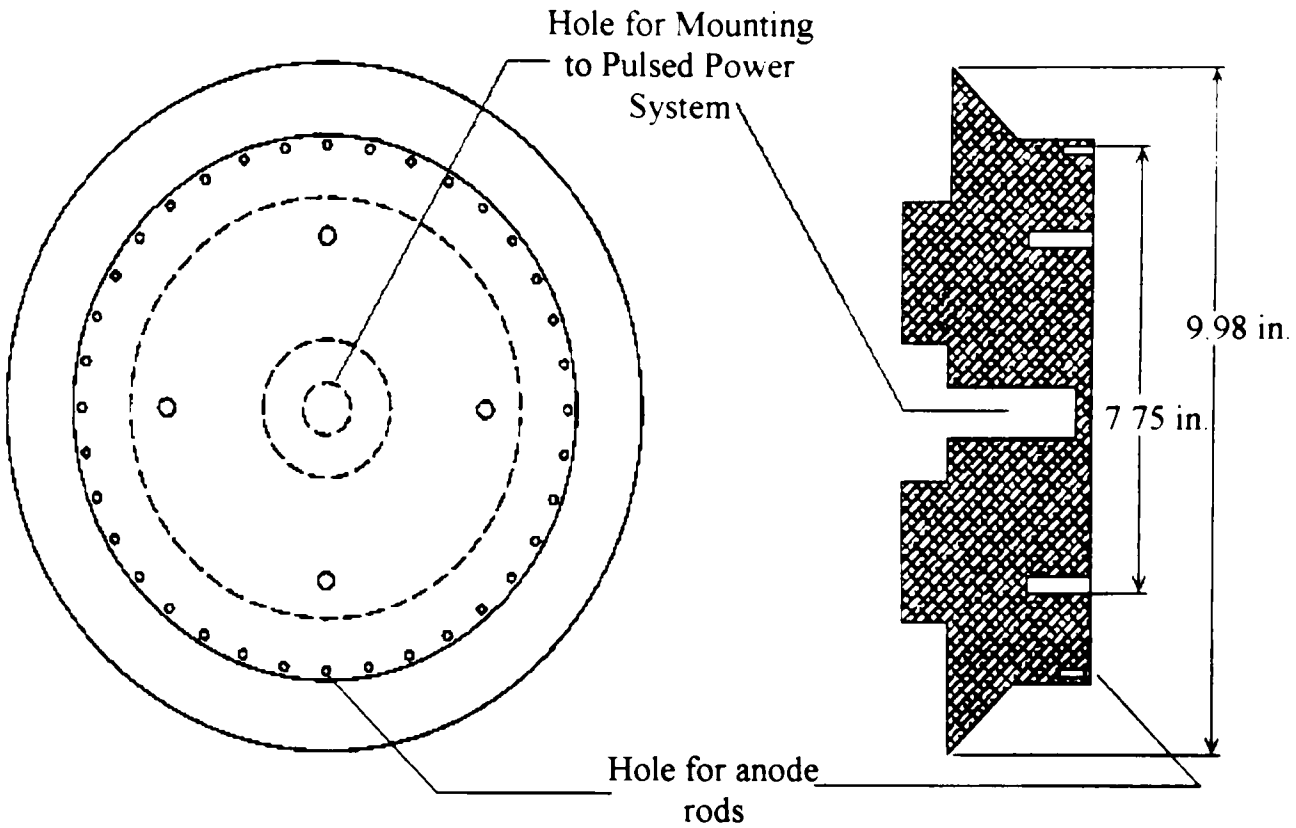

Figure 2.19: Diagram of the Anode of the Coaxial Vircator

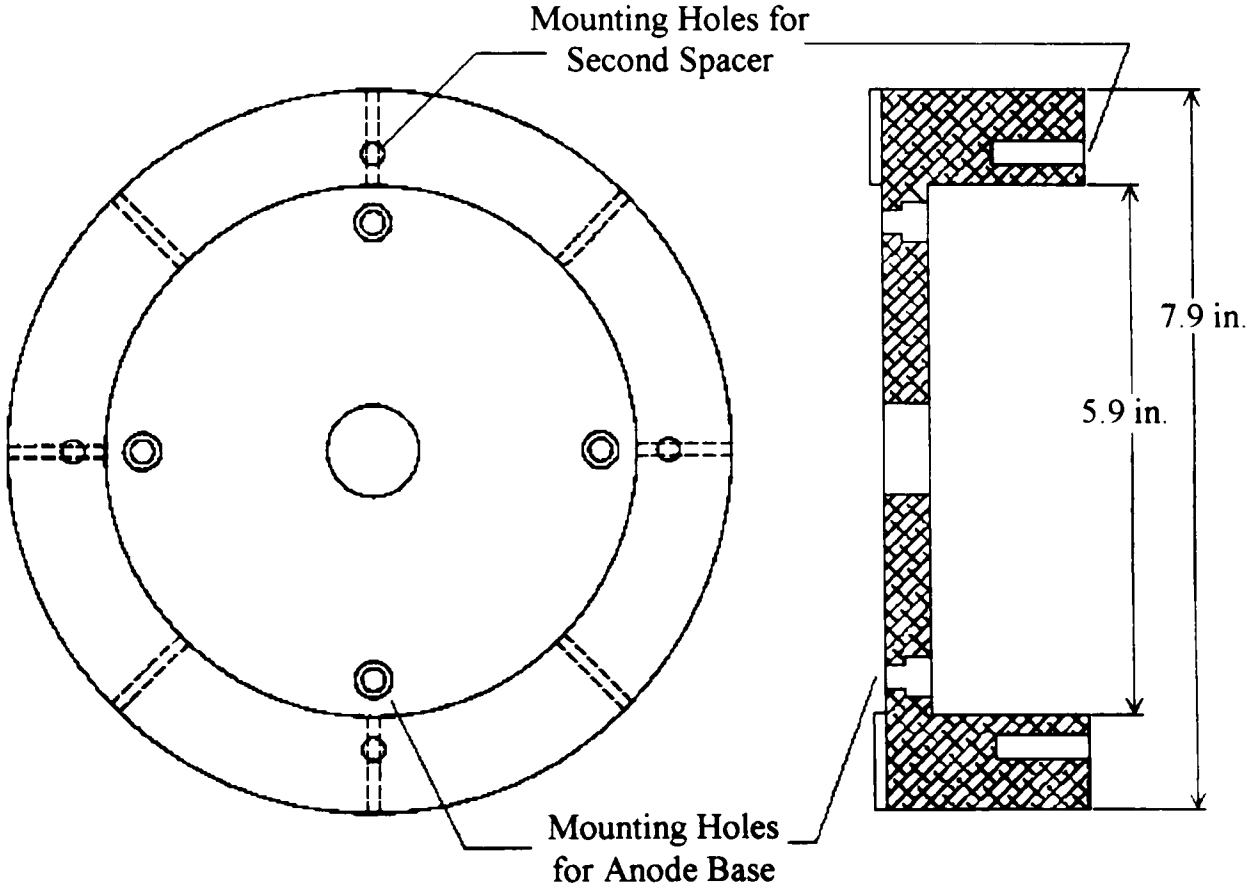

Figure 2.20: Diagram of the First Spacer of the Coaxial Vircator

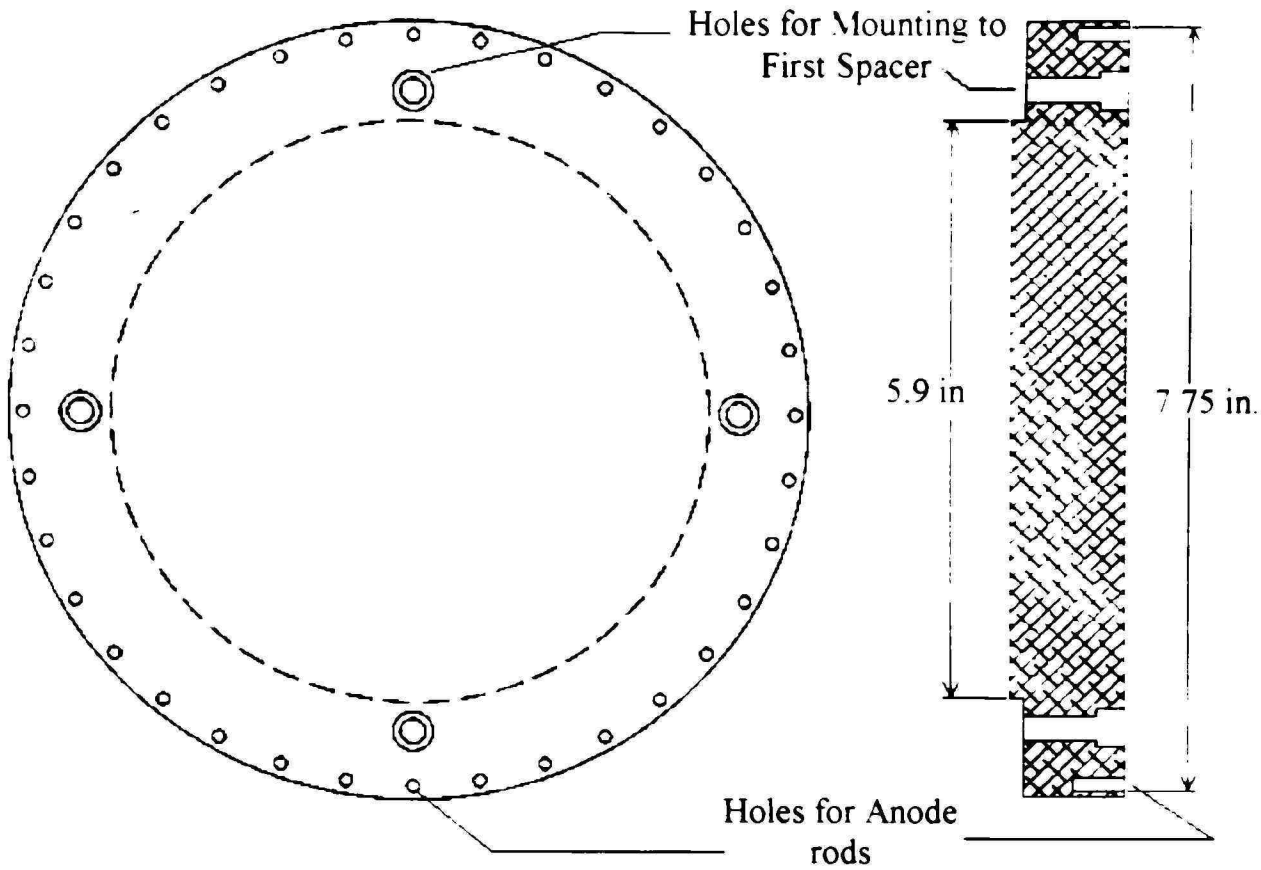

Figure 2.21: Diagram of the Second Spacer of the Coaxial Vircator

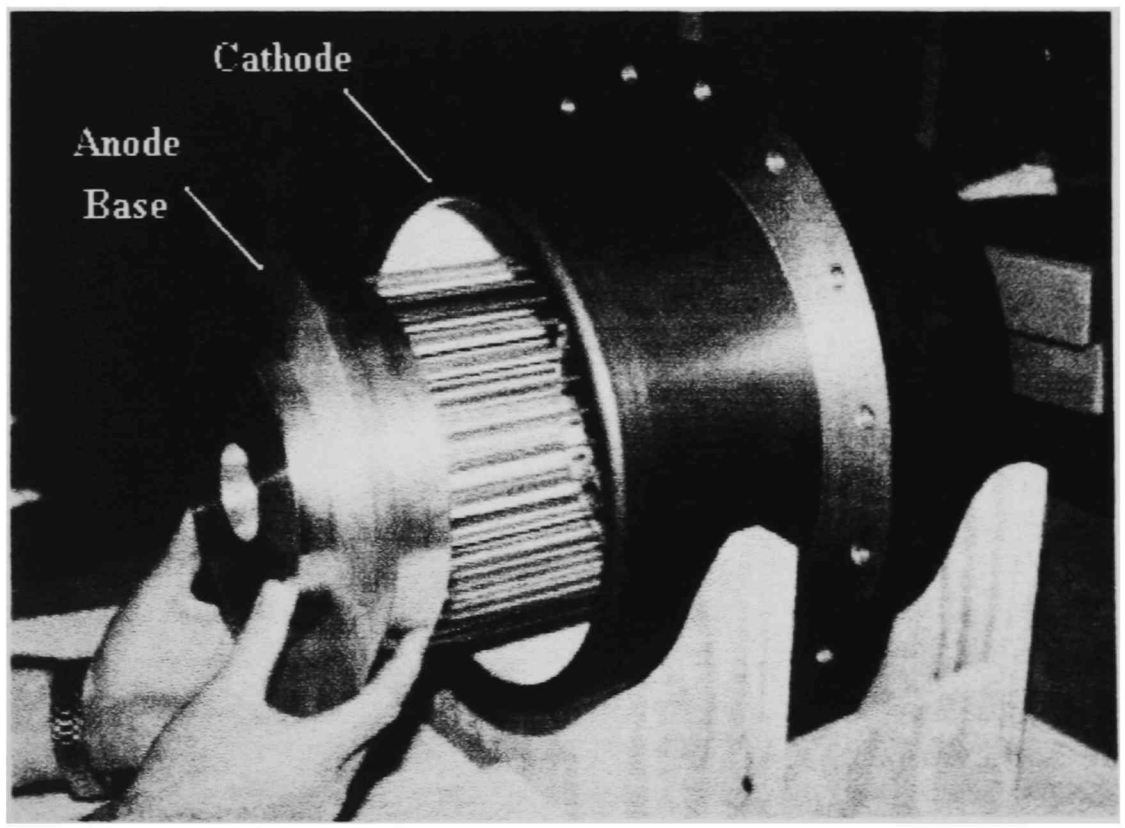

Figure 2.22: Picture of Coaxial Vircator Diode

During testing of the vircator the chamber pressure ranged from 2 to 6 μTorr. An overmoded waveguide couples the microwave power out of the diode region. The waveguide is under vacuum and is not terminated with a matching horn. Near the end of the waveguide is a Lexan window that maintains the vacuum. The diagnostic probes, discussed in Section 4.2, are also under vacuum.

CHAPTER 3
SIMULATIONS

With the complications involved with the many particles and time varying fields of vircators, any relevant calculation on its operation requires the use of computer simulation and even then, a powerful computer is a strict requirement. As computers become more powerful, the simulations performed get more detailed. Initially, computers were used to perform repetitive computations, usually on one aspect of the system such as the potential between parallel plates in a diode, and typically in only one dimension. But the information gained is limited since it did not tell what the field looked liked with the addition of particles or other factors taken into account. Then programs were written that simulated more of the entire picture, in two dimensions with a symmetrical third dimension. Eventually, a full three-dimensional simulation code was created. But these programs are not a final solution to accurately define the inner workings of a device. The programs are approximations to the precise solution and as one variable is used to calculate another variable, any error is propagated and additional errors may be added.

MAGIC, a two-dimensional code with a symmetric third dimension, is used to simulate the coaxial vircator geometry. The code is run on a Pentium Pro, 200 MHz personal computer with 64 Megabytes of RAM. The simulation works by taking time and breaking it up into a number of time intervals of size Δt. The geometry to be tested is also broken up into cells of size Δx. Macroparticles are added to the simulation, where a macroparticle is a representation of a large collection of particles. A stability criteria of the simulation with macroparticles is that the Courant condition is satisfied:

$$\Delta x > c\Delta t \tag{3.1}$$

where c is the speed of light. This merely states that a macroparticle can not traverse more than one cell in one time period. Another requirement for field resolution is that the cell-to-cell size difference must not vary greatly, 25% is an approximate upper limit. Further details can be obtained from the MAGIC user's manual.

It is not uncommon for the results of simulations to be inaccurate. In a reditron experiment, the simulated diode current was 20 - 40 percent lower than in the experiment [13]. It was also shown in diode simulation experiments that as the number of cells spaced between the anode and cathode increased, the current obtained from simulation approached the theoretical value but still did not reach it [14]. But in the simulation codes, a fixed number of cells or usable memory is available and to make the results extremely accurate requires hardware typically unavailable, except on a Cray supercomputer. In addition, the increase in the number of cells results in a decreased cell size. This decreased cell size results in a decreased time step and increased number of macroparticles that increases computation time. Eventually, time and resources must be balanced to obtain results that are accurate to a high enough degree to obtain some meaningful information.

3.1 Initial Simulation

Simulations were performed to gain an understanding of the coaxial vircator and see how closely the simulations modeled the experiment. From the simulations, multiple plots could be turned into animations and the behavior of the vircator watched as time proceeded. This was done and many of the behaviors of the vircator were observed. These behaviors include the cycling of wrong-phased electrons, the reflexing of the bunched electrons, how the shape of the virtual cathode changes with time, how the radial momentum of the particles changes and a number of parameters that MAGIC can output in graphical format.

The initial simulation performed was to verify that the simulation results came close to the results of the experimental system. The simulated diode region is shown in Figure 3.1. The initial simulation parameters are given in Table 3.1. The results of interest from the simulation include the diode voltage, diode current and frequency of operation. The simulation diode voltage and frequency matched closely with experiment, the current on the other hand was lower by about half, leading to the conclusion that something was not being modeled correctly. The results of the initial simulation are shown in Figure 3.2 and the simulation results are shown in Table 3.2.

Table 3.1 Initial Simulation Variables

	r_a	r_k	D_f	D_s	D_t
Value (in.)	3.875	5.186	1.748	4.5	3.25

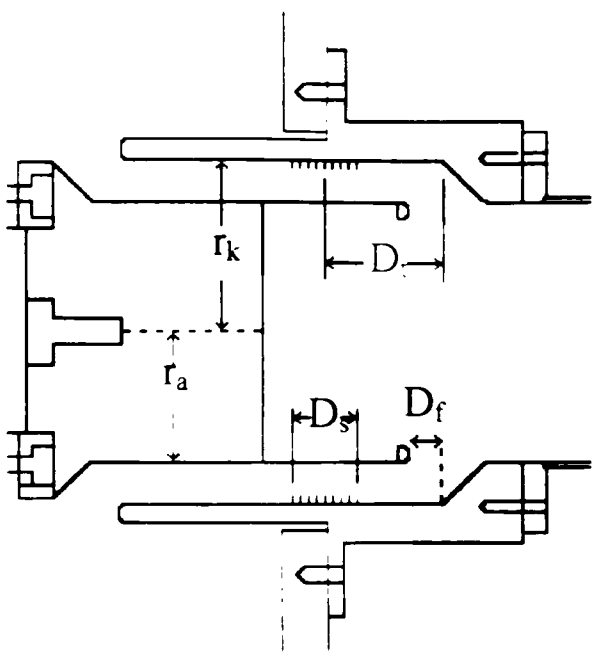

Figure 3.1 Simulated Diode Region

In defining the simulation, the geometry, including conductors and any other physical device of the experiment, was set up on a grid with sizes approximately the same as the physical dimensions of the experiment. Then a TEM wave was launched down a coaxial transmission line into the diode region. The magnitude of the launched wave was adjusted until the simulation gave a voltage similar to the experiment. An explosive emitter is defined to emit a given number of macroparticles each time step after a preset field intensity is overcome. This represents the velvet emitter in the experiment. The initial simulation results, Table 3.2, indicated a diode current that was too low compared to experiment. Various characteristics in the simulation are defined and can be changed to increase the current, these include increasing the initial velocity given to created macroparticles or increasing the thickness of the foil or both. But this can only increase the current slightly and another physical cause was sought. It was believed that bipolar flow was the cause for the increased current and so it was added to the simulations. Bipolar flow and the results are the topic of the next section.

Additional parameters that help gain information about the functioning of the vircator are the particle and phase-space plots at an instant of time. The first plot, in all

of the figures of results, is a plot of particle position in the simulated geometry, see Figure 3.2(a). The figure is a slice of the simulation region showing the diode. The bottom of the figure is the center-line axis of symmetry about which the figure is assumed symmetrical. In the figure, the solid lines are conductors or foil and the small objects are macroparticles. The second phase-space plot is a plot of radial momentum versus radial position. Also included in the results is the fast Fourier transform plot of the radial electric field microwave radiation produced by the vircator at the wall of the output waveguide. The final plot is the output power produced by the vircator. Previous versions of MAGIC required that the mode produced be known and then the power produced at a frequency could be calculated. This was inaccurate and newer versions of MAGIC contain a routine that calculates the power. The graphs in all simulation results are direct outputs from MAGIC simulations and is the cause for the poor quality of the text.

Typical information that is obtained from the phase-space simulation results is just a small portion of all information in the results but are considered to be the most important in determining how the coaxial vircator functions. Many of these phase-space plots have been turned into animations for more insight into the performance of the coaxial vircator. In the first plot, the form and placement of the virtual cathode, the number of macroparticles inside the radius of the virtual cathode and the placement of other macroparticles is observed. In the second phase-space plot, the height and width of the diamond shape of macroparticles, indicating reflexing, the intensity of the diamond, and the number and position of particles to the left of and inside the diamond are observed. Other graphs display the frequency of operation, and output power. These results along with the results of the diode voltage and diode current allow a calculation of the efficiency which is important because the simulations are performed to see how the efficiency can be increased or decreased by subtle changes.

It should be noted that the simulations are just guidelines with many parts of the actual experiment not being simulated. Differences from experiment to simulation include lossy conductors, a non-ideal vacuum, operating conditions that change from shot to shot, discretized time steps, macroparticles that all move together and many others. It

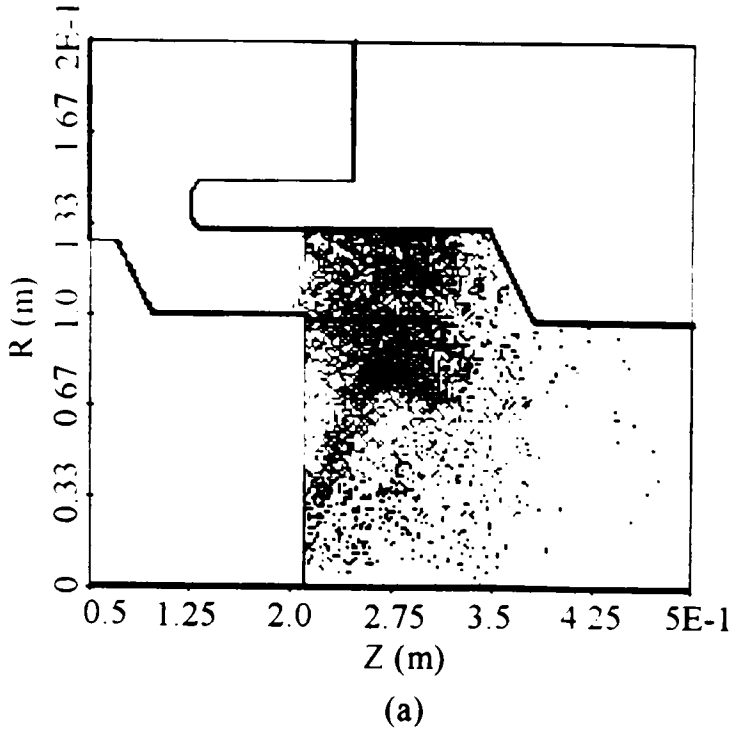

(a)

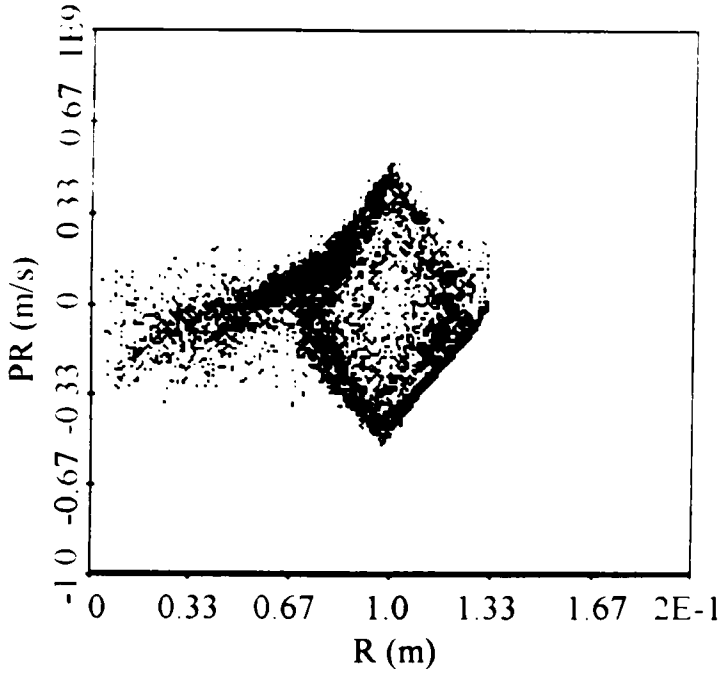

(b)

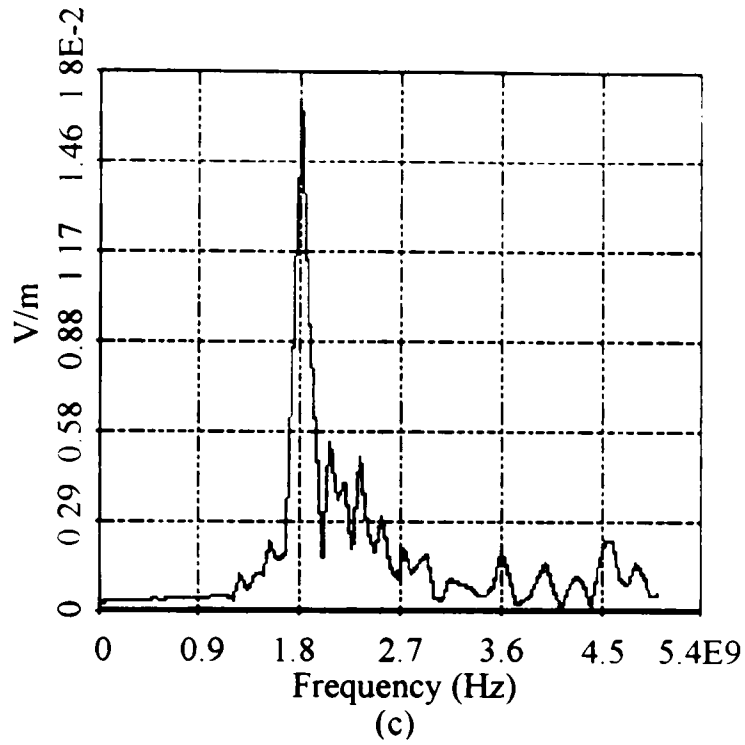

(c)

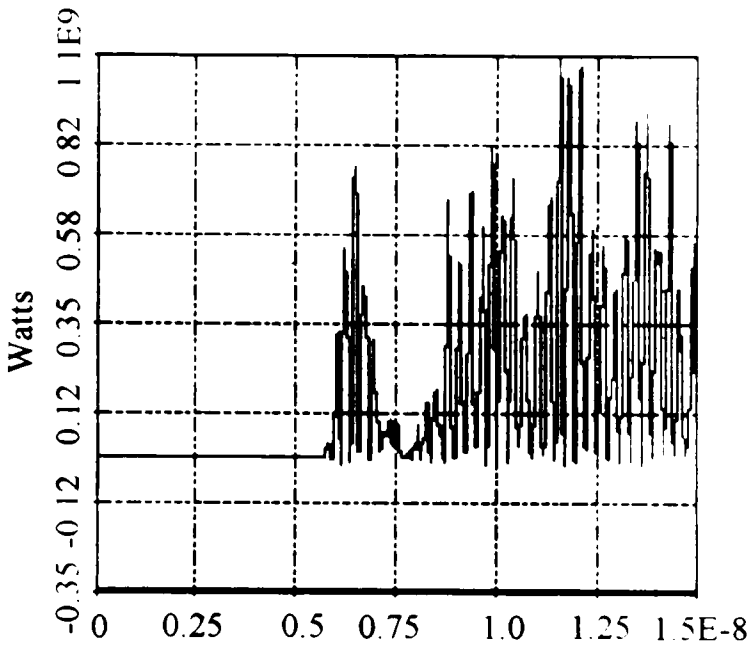

(d)

Figure 3.2: Initial Simulation Results.
(a) Particle position @ 5 ns, (b) r versus ρ_r phase space @ 5 ns, (c) E_r at wall versus frequency, (d) Output microwave power

Table 3.2: Initial Simulation Results

Parameter	Value
Diode Voltage (V_d)	550 kV
Diode Current (I_d)	30 kA
Diode Impedance (Z_d)	18.33 Ω
Beam Power (P_{beam})	16.5 GW
Microwave Frequency (f)	1.8 GHz
Microwave Power (P_{mw})	1.05 GW
Power Efficiency (η)	6.36%

is hoped that the simulations are modeled well enough to obtain accurate results that lead to experiments that are verified by simulation.

3.2 Simulations with Bipolar Flow

As indicated in the initial simulation results, the model for the coaxial vircator was inaccurate in describing what was happening in the experiment. The current obtained from the simulation gave a value of 30 kA while 45 – 60 kA was obtained in the experiments. The expected cause for this is bipolar flow.

Bipolar flow is the process whereby positive ions are injected into the system along with the electrons. The positive ions are created as the electron current increases and impinges upon the anode, then absorbed gases or impurities in or on the anode become ionized and form a plasma of positive ions. This anode plasma then propagates in a direction opposite to the electron flow at a velocity much lower than the electron velocity. For the vircator, positive ions also propagate towards the virtual cathode due to the negative charge of the virtual cathode. Figure 3.3 shows a diagram of bipolar flow.

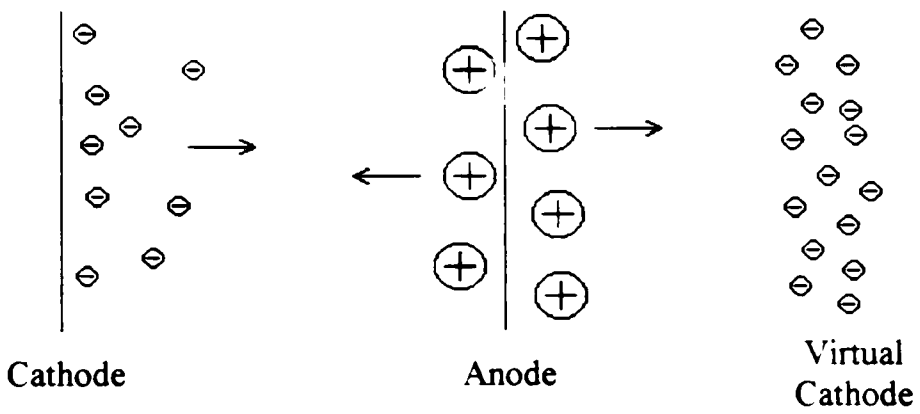

Figure 3.3: Diagram of Bipolar Flow in a Vircator

In the simulations, the ions are assumed to be protons since vircator experiments in Japan have shown protons to be the cause for bipolar flow in their experiment due to water impurities [15]. In the simulations, ions are created when the first electron crosses the anode. From simulation phase-space diagrams, it takes approximately eight nanoseconds for the protons to cross the anode-cathode gap. The added ions, due to their positive charge, cause a decrease in the space charge in the anode-cathode gap. This allows more electrons to enter the previous space charge limited anode-cathode gap,

causing an increase in the diode current. Also, as ions approach the virtual cathode, the virtual cathode becomes less defined and "smears" in the negative radial direction. The following figures and results are from MAGIC simulations with bipolar flow. From the tables of the simulation results it is seen that bipolar flow gives a current close to the experimental values.

In the figures and tables of the simulation results, the geometry is identical to the initial simulation except for minor differences. These differences include the addition of various sized rods and a hole placed on axis of the anode base. The exact geometry with these changes can be seen in the first plot of the simulation results. The other differences include using aluminum as the foil material, using a 1.25 inch wide emitter and varying the applied potential. Two separate applied potentials are studied. The "High Voltage" potential corresponds to a per capacitor charge of 32 kV and the "Low Voltage" potential corresponds to a per capacitor charge of 25 kV. Table 3.3 shows the various simulations performed and the corresponding figure that contains the results. An interesting result from the simulations showed an decrease in impedance with a higher applied potential. Bipolar flow is the cause for the impedance change. With the higher potential across the diode, positive ions move faster allowing more ions to be injected into the gap. This increases the space charge allowing more electrons in the gap which is an increase in current. This increased current causes the decrease in impedance.

Table 3.3: List of Simulated Geometries

Figure	Description
Figure 3.4	Standard Geometry (High Voltage)
Figure 3.5	Standard Geometry (Low Voltage)
Figure 3.6	Geometry with Aluminum Foil (High Voltage)
Figure 3.7	Geometry with Aluminum Foil (Low Voltage)
Figure 3.8	Geometry with Small Collection Rod (High Voltage)
Figure 3.9	Geometry with Small Collection Rod (Low Voltage)
Figure 3.10	Geometry with Large Collection Rod (High Voltage)
Figure 3.11	Geometry with Large Collection Rod (Low Voltage)
Figure 3.12	Geometry with a Hole (High Voltage)
Figure 3.13	Geometry with a Hole (Low Voltage)
Figure 3.14	Geometry with 1.25" Strip (High Voltage)
Figure 3.15	Geometry with 1.25" Strip (Low Voltage)

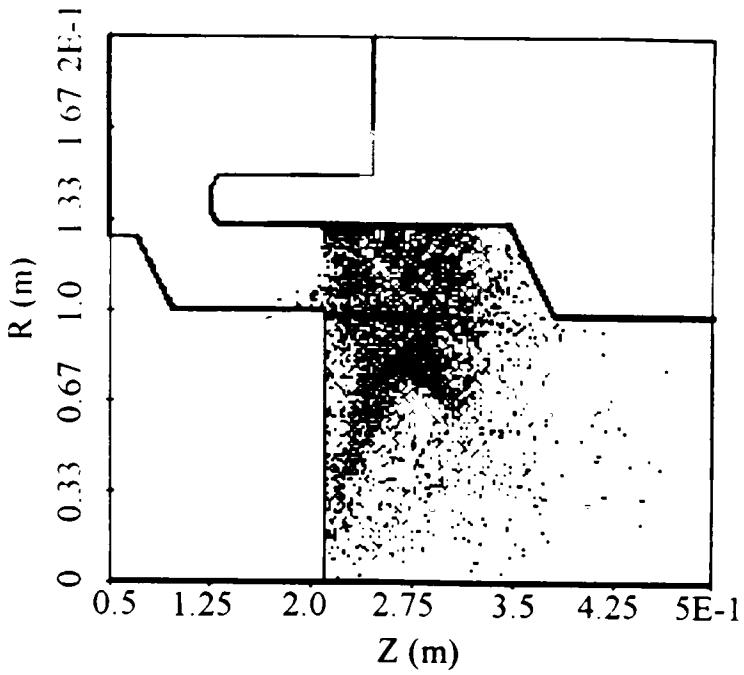

(a)

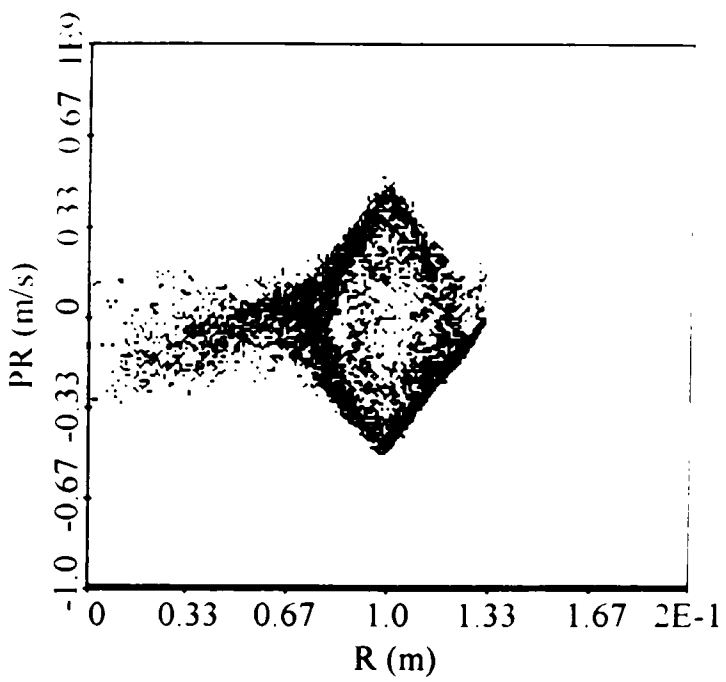

(b)

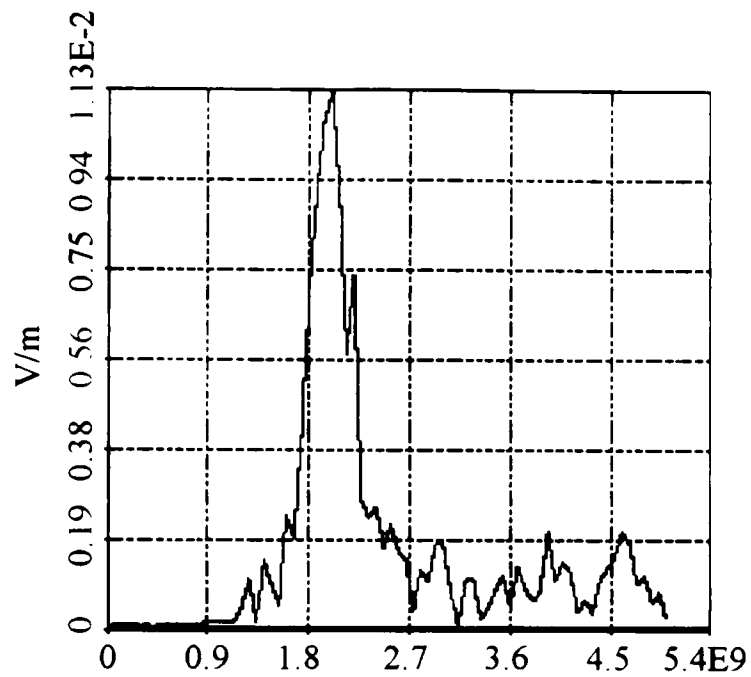

(c)

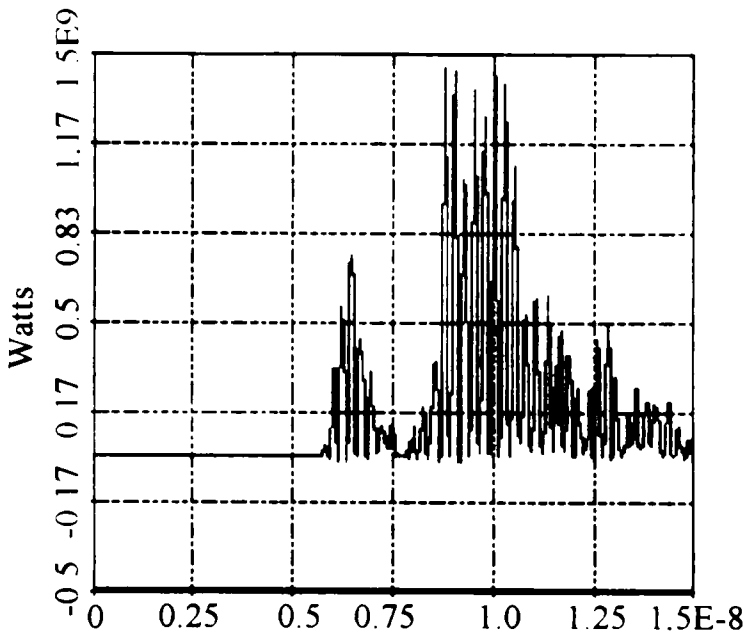

(d)

Figure 3.4: Results for the Standard Geometry, High Voltage.
(a) Particle position @ 5 ns, (b) r versus ρ_r phase space @ 5 ns, (c) E_r at wall versus frequency, (d) Output microwave power

Table 3.4: Results for the Standard Geometry, High Voltage

Parameter	Value
Diode Voltage (V_d)	570 kV
Diode Current (I_d)	50 kA
Diode Impedance (Z_d)	11.4 Ω
Beam Power (P_{beam})	28.5 GW
Microwave Frequency (f)	1.94 GHz
Microwave Power (P_{mw})	1.43 GW
Power Efficiency (η)	5.02 %

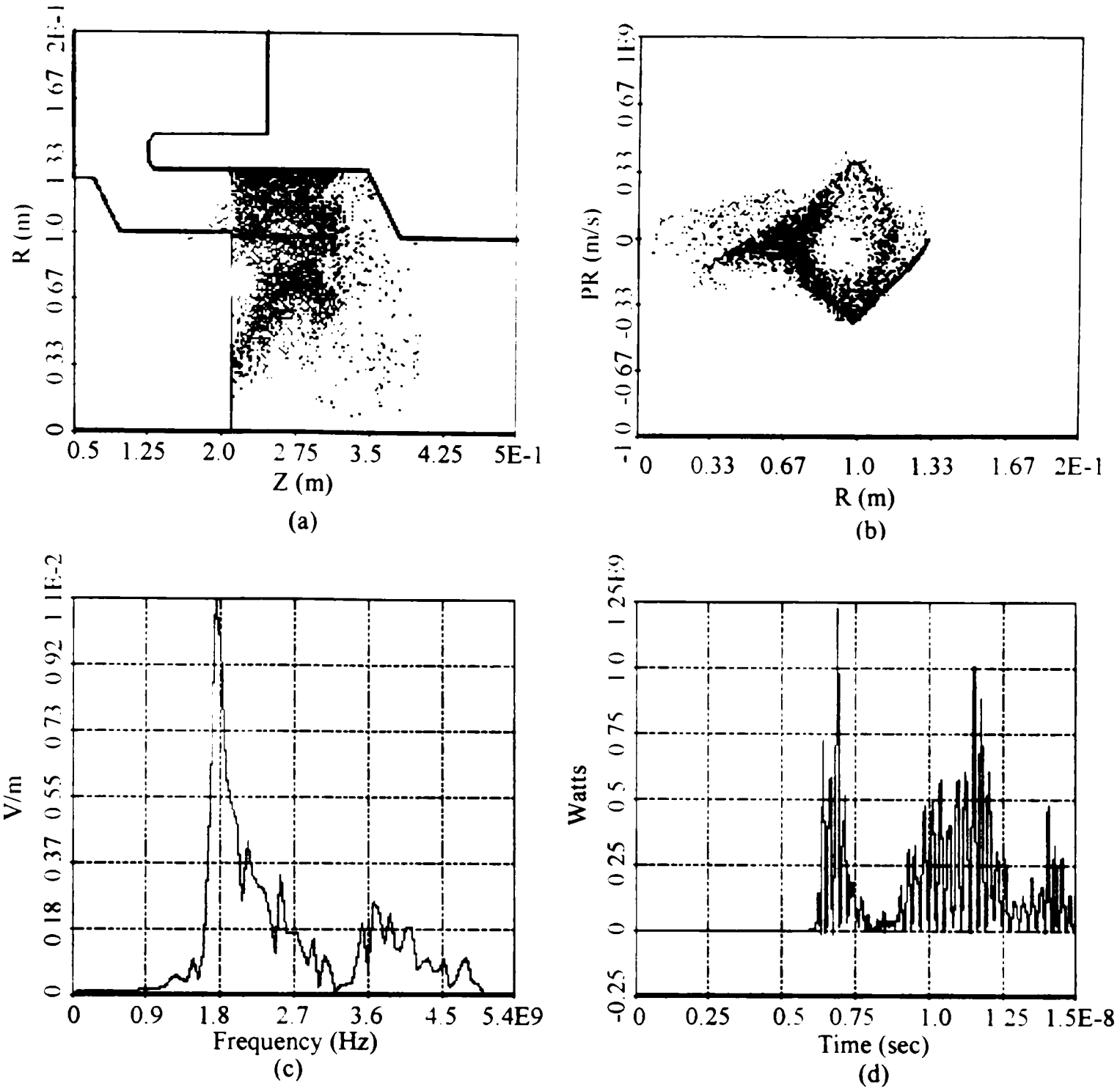

Figure 3.5: Results for the Standard Geometry, Low Voltage.
(a) Particle position @ 5 ns, (b) r versus ρ_r phase space @ 5 ns, (c) E_r at wall versus frequency, (d) Output microwave power

Table 3.5: Results for the Standard Geometry, Low Voltage

Parameter	Value
Diode Voltage (V_d)	440 kV
Diode Current (I_d)	35 kA
Diode Impedance (Z_d)	12.57 Ω
Beam Power (P_{beam})	15.4 GW
Microwave Frequency (f)	1.71 GHz
Microwave Power (P_{mw})	1.23 GW
Power Efficiency (η)	7.99 %

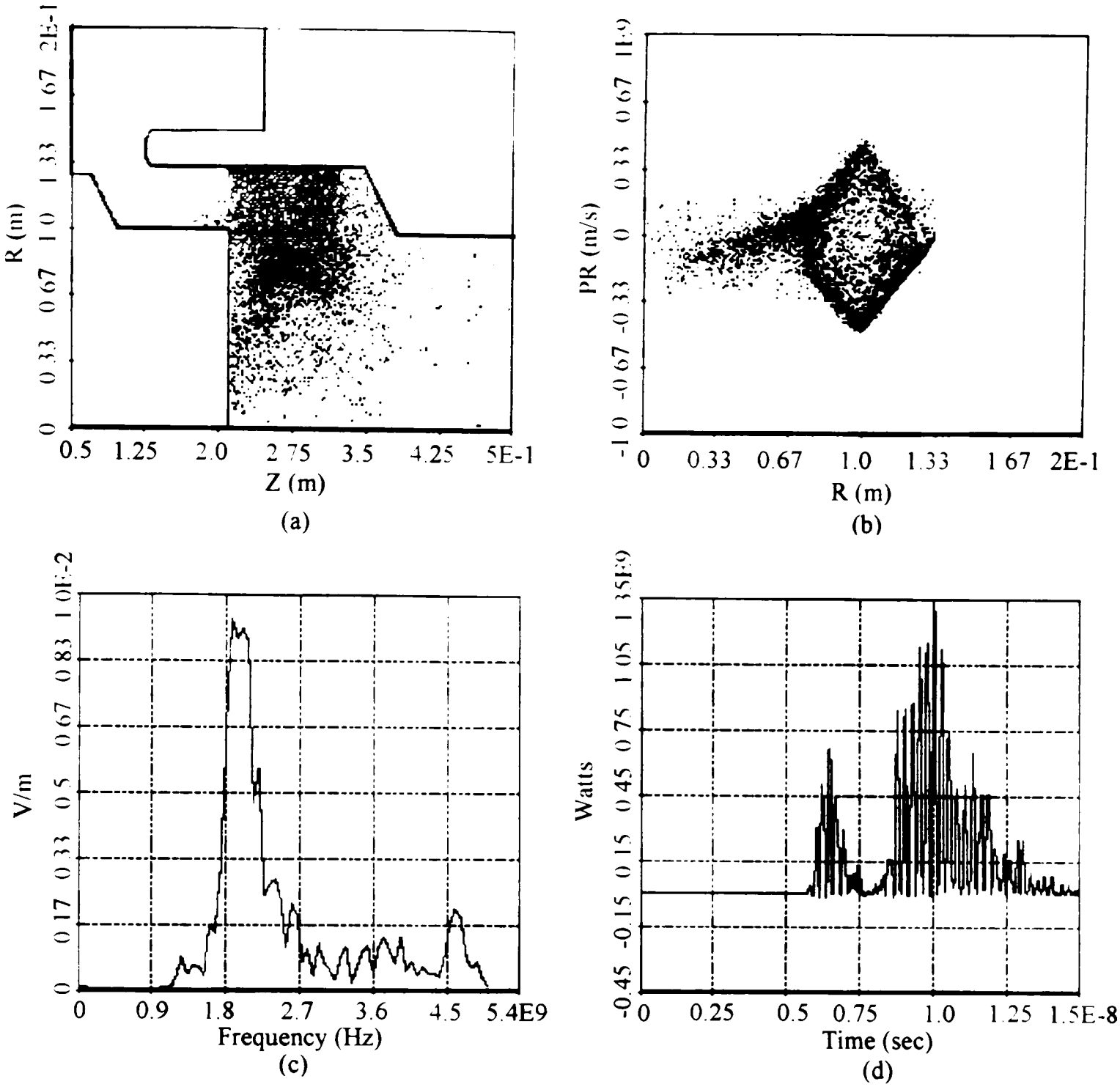

Figure 3.6: Results for the Geometry with Aluminum Foil, High Voltage.
(a) Particle position @ 5 ns, (b) r versus ρ_r phase space @ 5 ns, (c) E_r at wall versus frequency, (d) Output microwave power

Table 3.6: Results for the Geometry with Aluminum Foil, High Voltage

Parameter	Value
Diode Voltage (V_d)	550 kV
Diode Current (I_d)	50 kA
Diode Impedance (Z_d)	11 Ω
Beam Power (P_{beam})	27.5 GW
Microwave Frequency (f)	1.85 GHz
Microwave Power (P_{mw})	1.31 GW
Power Efficiency (η)	4.76 %

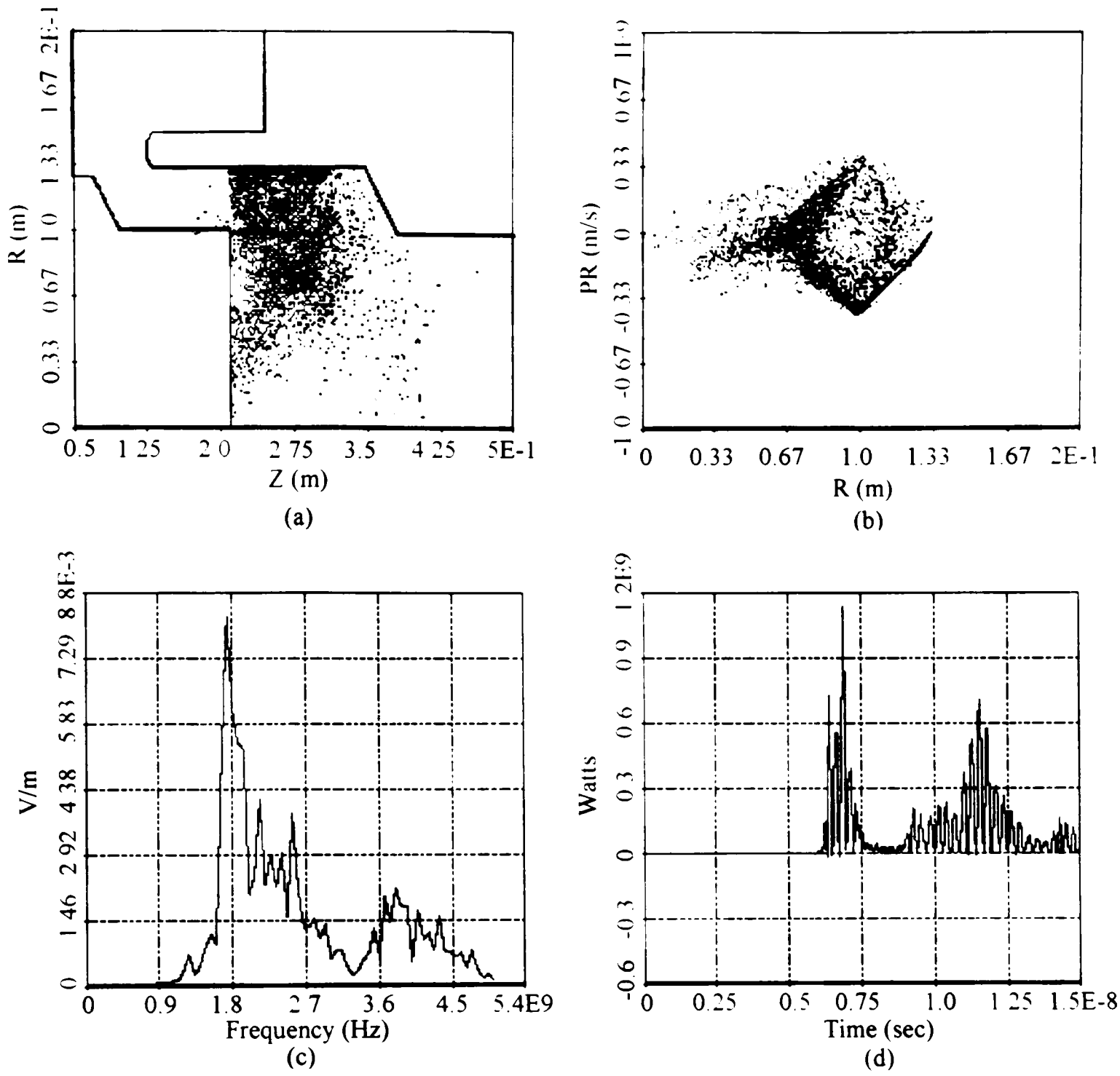

Figure 3.7: Results for the Geometry with Aluminum Foil, Low Voltage.
(a) Particle position @ 5 ns, (b) r versus ρ_r phase space @ 5 ns, (c) E_r at wall versus frequency, (d) Output microwave power

Table 3.7: Results for the Geometry with Aluminum Foil, Low Voltage

Parameter	Value
Diode Voltage (V_d)	420 kV
Diode Current (I_d)	33 kA
Diode Impedance (Z_d)	12.73 Ω
Beam Power (P_{beam})	13.86 GW
Microwave Frequency (f)	1.67 GHz
Microwave Power (P_{mw})	1.14 GW
Power Efficiency (η)	8.23 %

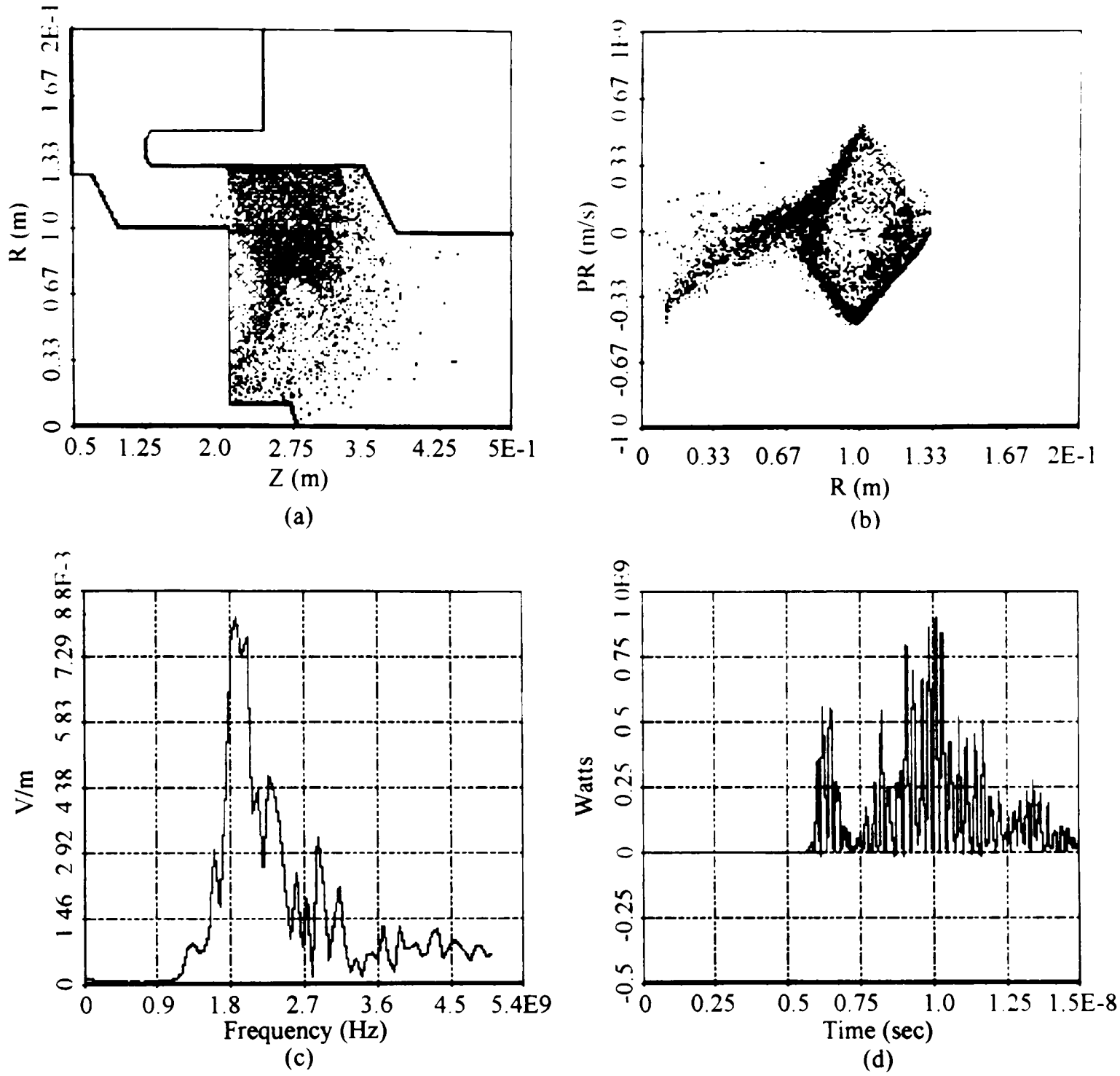

Figure 3.8: Results for the Geometry with Small Rod, High Voltage.
(a) Particle position @ 5 ns, (b) r versus ρ_r phase space @ 5 ns, (c) E_r at wall versus frequency, (d) Output microwave power

Table 3.8: Results for the Geometry with Small Rod, High Voltage

Parameter	Value
Diode Voltage (V_d)	570 kV
Diode Current (I_d)	50 kA
Diode Impedance (Z_d)	11.40 Ω
Beam Power (P_{beam})	28.5 GW
Microwave Frequency (f)	1.9 GHz
Microwave Power (P_{mw})	0.9 GW
Power Efficiency (η)	3.16 %

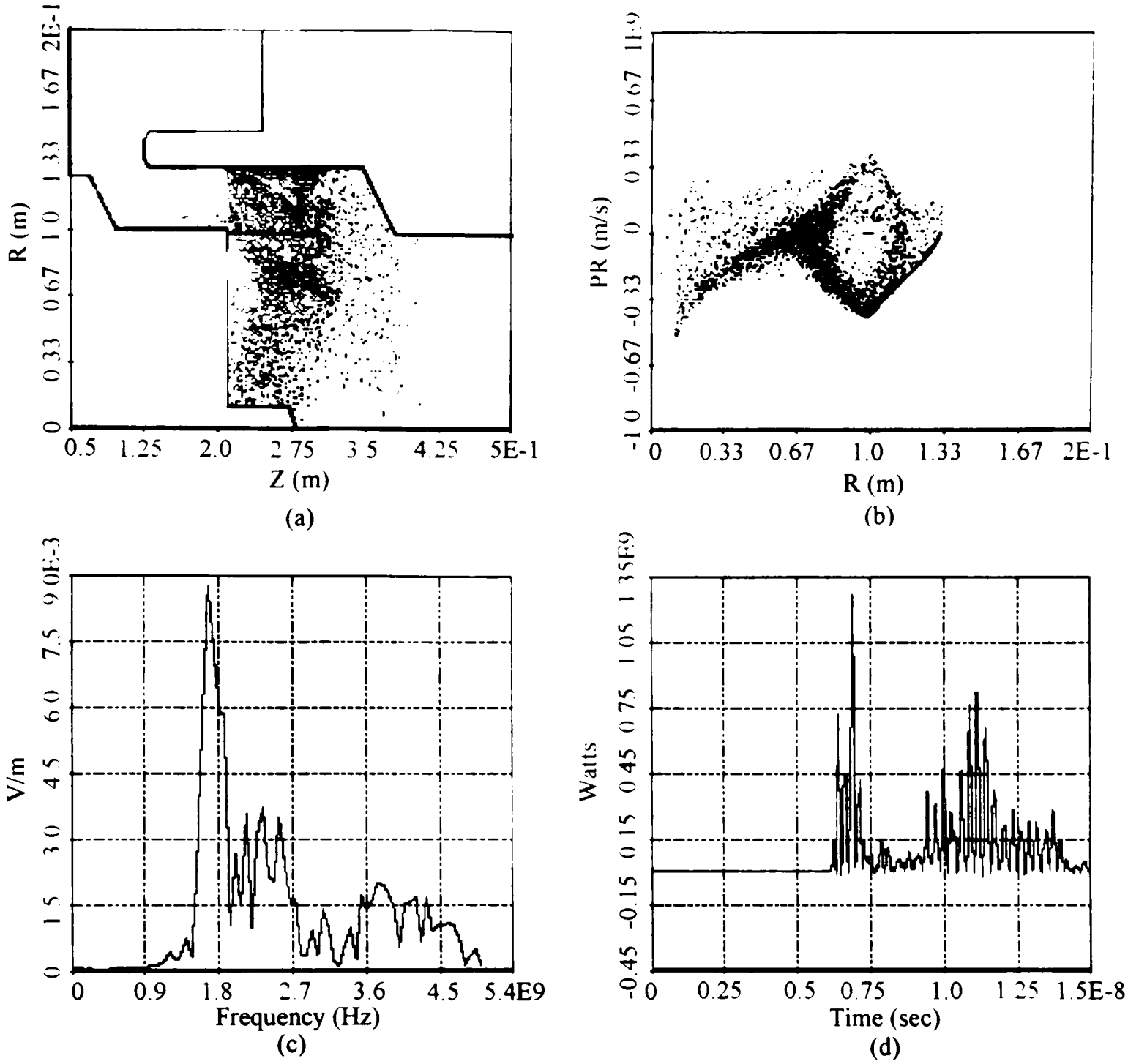

Figure 3.9: Results for the Geometry with Small Rod, Low Voltage.
(a) Particle position @ 5 ns, (b) r versus ρ_r phase space @ 5 ns, (c) E_r at wall versus frequency, (d) Output microwave power

Table 3.9: Results for the Geometry with Small Rod, Low Voltage

Parameter	Value
Diode Voltage (V_d)	430 kV
Diode Current (I_d)	35 kA
Diode Impedance (Z_d)	12.29 Ω
Beam Power (P_{beam})	15.05 GW
Microwave Frequency (f)	1.62 GHz
Microwave Power (P_{mw})	1.28 GW
Power Efficiency (η)	8.5 %

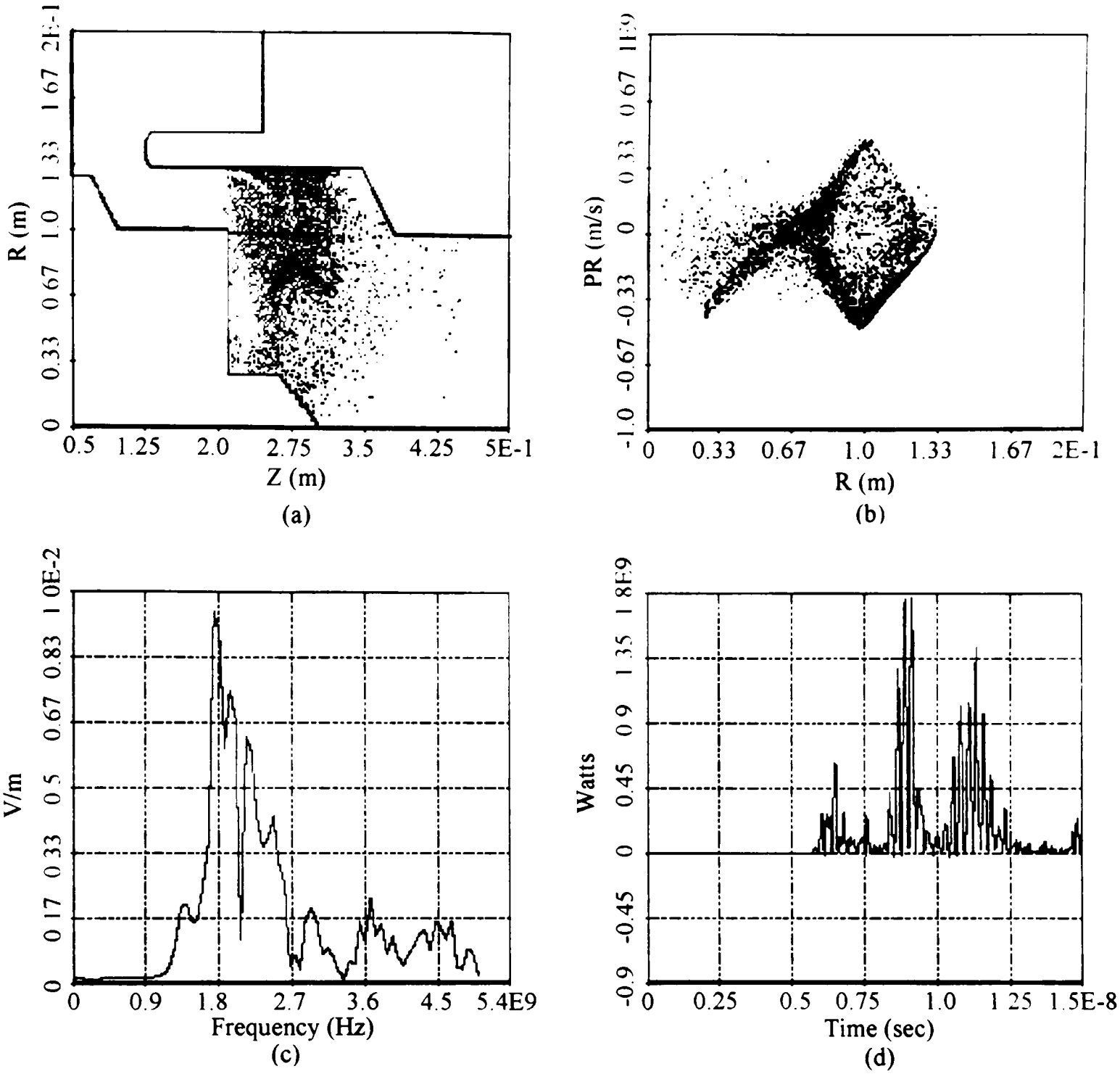

Figure 3.10: Results for the Geometry with a Large Rod, High Voltage.
(a) Particle position @ 5 ns, (b) r versus ρ_r phase space @ 5 ns, (c) E_r at wall versus frequency, (d) Output microwave power

Table 3.10: Results for the Geometry with a Large Rod, High Voltage

Parameter	Value
Diode Voltage (V_d)	550 kV
Diode Current (I_d)	51 kA
Diode Impedance (Z_d)	10.78 Ω
Beam Power (P_{beam})	28.05 GW
Microwave Frequency (f)	1.71 GHz
Microwave Power (P_{mw})	1.78 GW
Power Efficiency (η)	6.35 %

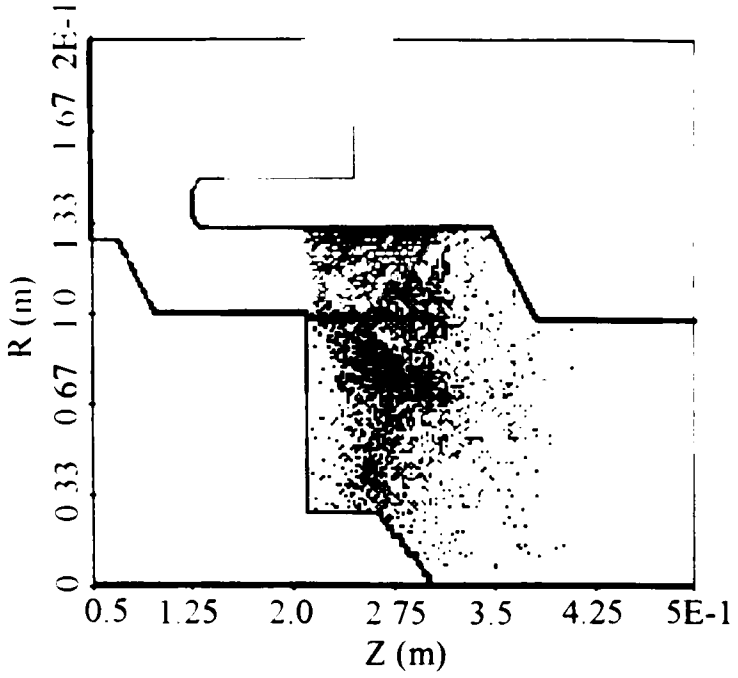

(a)

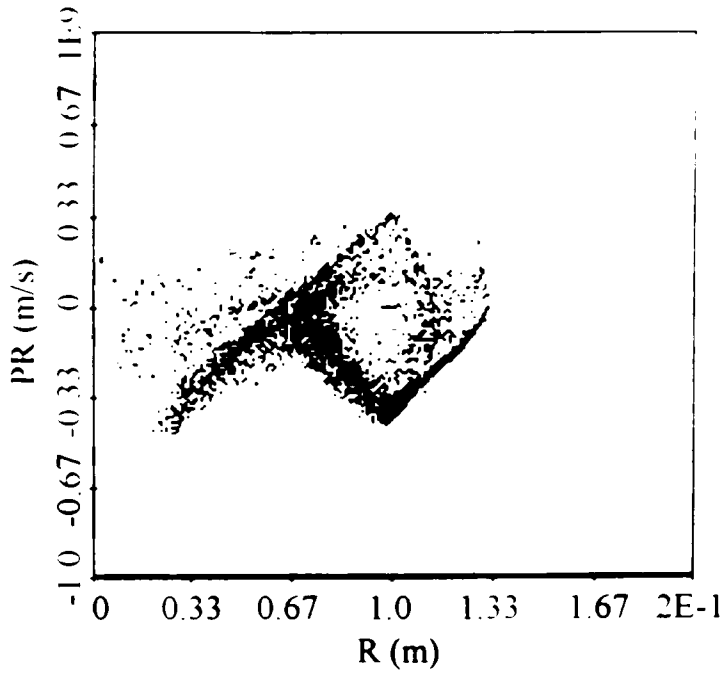

(b)

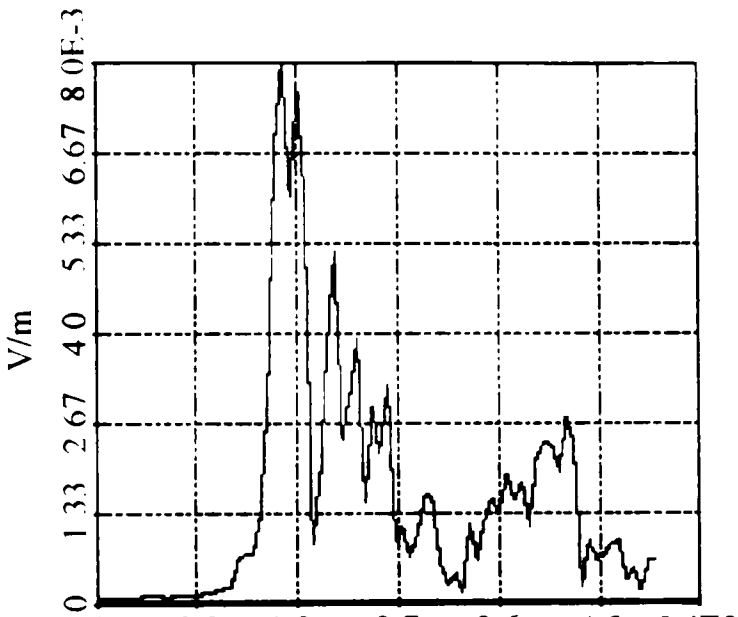

(c)

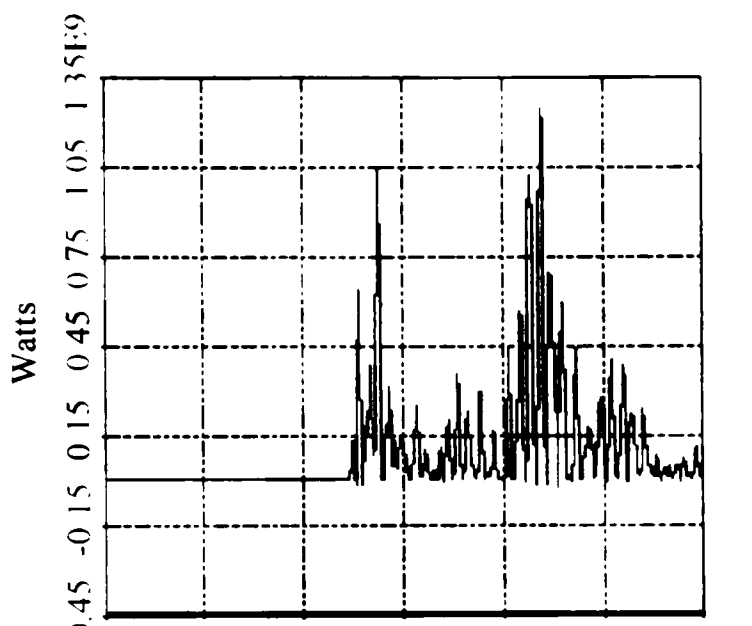

(d)

Figure 3.11: Results for the Geometry with a Large Rod, Low Voltage.
(a) Particle position @ 5 ns, (b) r versus ρ_r phase space @ 5 ns, (c) E_r at wall versus frequency, (d) Output microwave power

Table 3.11: Results for the Geometry with a Large Rod, Low Voltage

Parameter	Value
Diode Voltage (V_d)	440 kV
Diode Current (I_d)	36 kA
Diode Impedance (Z_d)	12.22 Ω
Beam Power (P_{beam})	15.84 GW
Microwave Frequency (f)	1.62 GHz
Microwave Power (P_{mw})	1.29 GW
Power Efficiency (η)	8.14 %

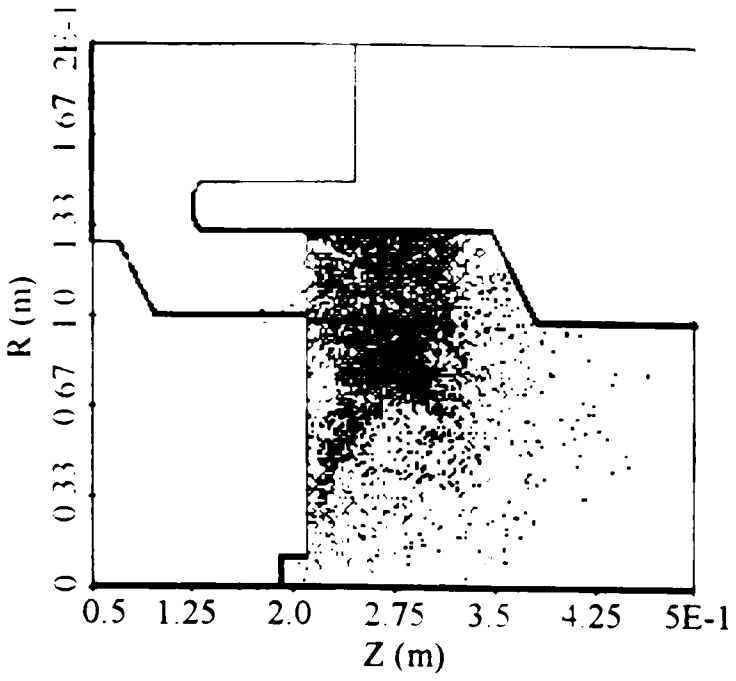

(a)

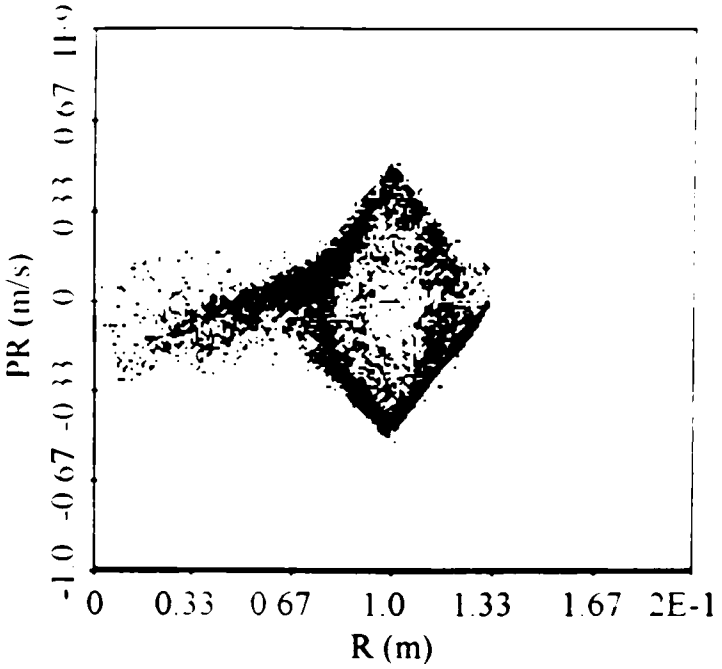

(b)

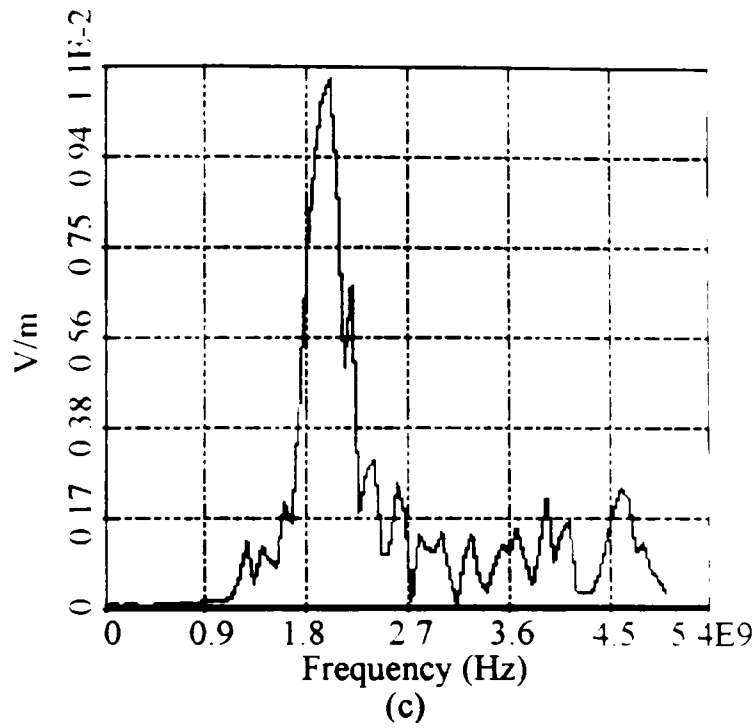

(c)

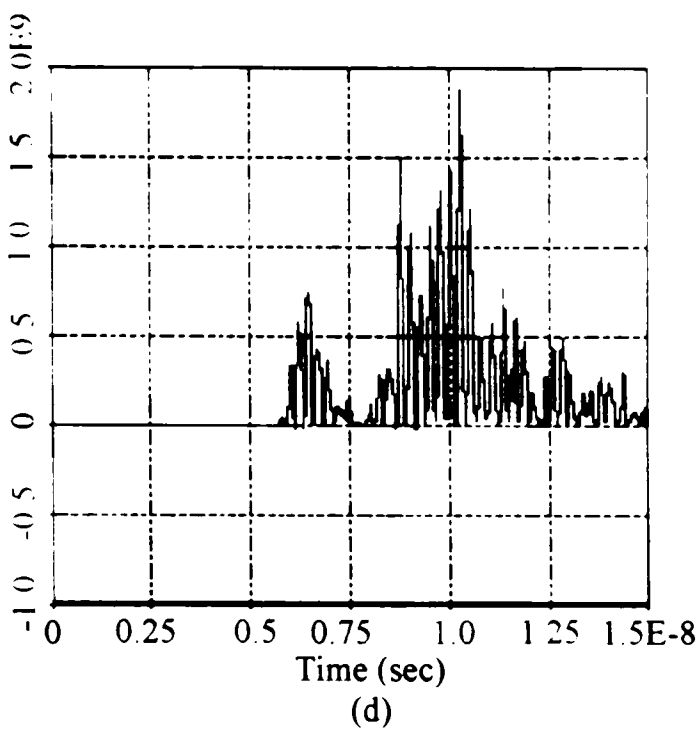

(d)

Figure 3.12: Results for the Geometry with a Hole, High Voltage.
(a) Particle position @ 5 ns, (b) r versus ρ_r phase space @ 5 ns, (c) E_r at wall versus frequency, (d) Output microwave power

Table 3.12: Results for the Geometry with a Hole, High Voltage

Parameter	Value
Diode Voltage (V_d)	550 kV
Diode Current (I_d)	50 kA
Diode Impedance (Z_d)	11 Ω
Beam Power (P_{beam})	27.5 GW
Microwave Frequency (f)	1.98 GHz
Microwave Power (P_{mw})	1.88 GW
Power Efficiency (η)	6.84 %

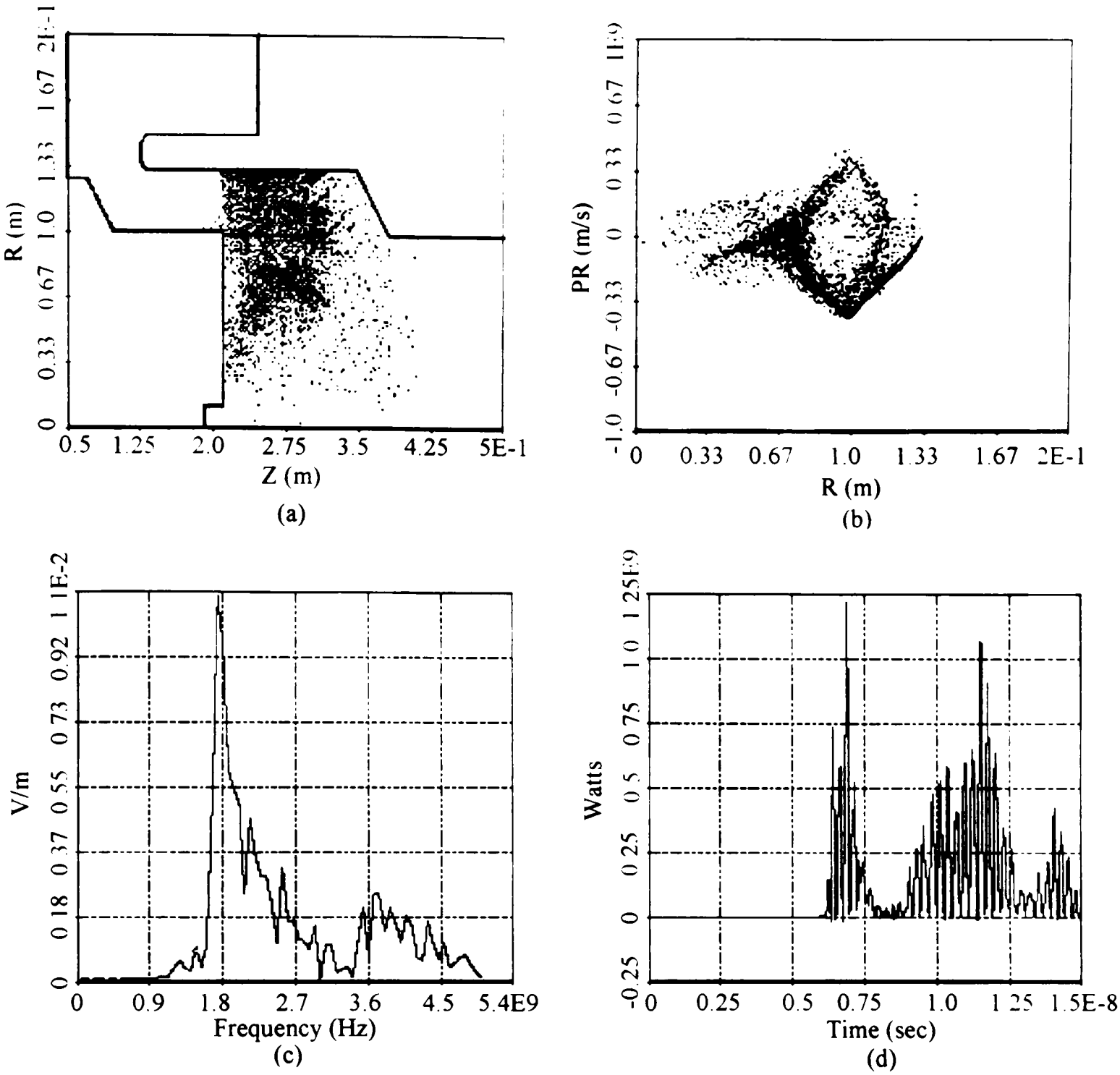

Figure 3.13: Results for the Geometry with a Hole, Low Voltage.
(a) Particle position @ 5 ns, (b) r versus ρ_r phase space @ 5 ns, (c) E_r at wall versus frequency, (d) Output microwave power

Table 3.13: Results for the Geometry with a Hole, Low Voltage

Parameter	Value
Diode Voltage (V_d)	428 kV
Diode Current (I_d)	34 kA
Diode Impedance (Z_d)	12.59 Ω
Beam Power (P_{beam})	14.55 GW
Microwave Frequency (f)	1.71 GHz
Microwave Power (P_{mw})	1.23 GW
Power Efficiency (η)	8.45 %

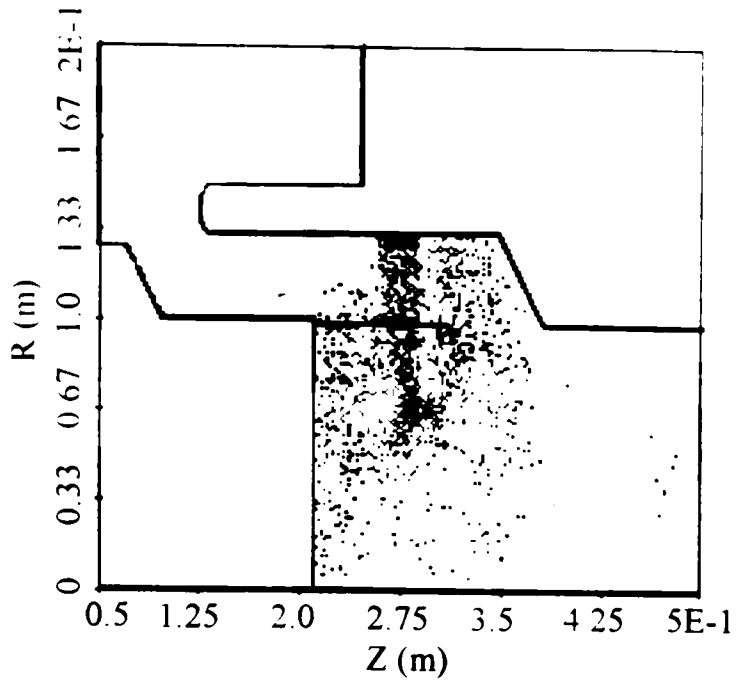

(a)

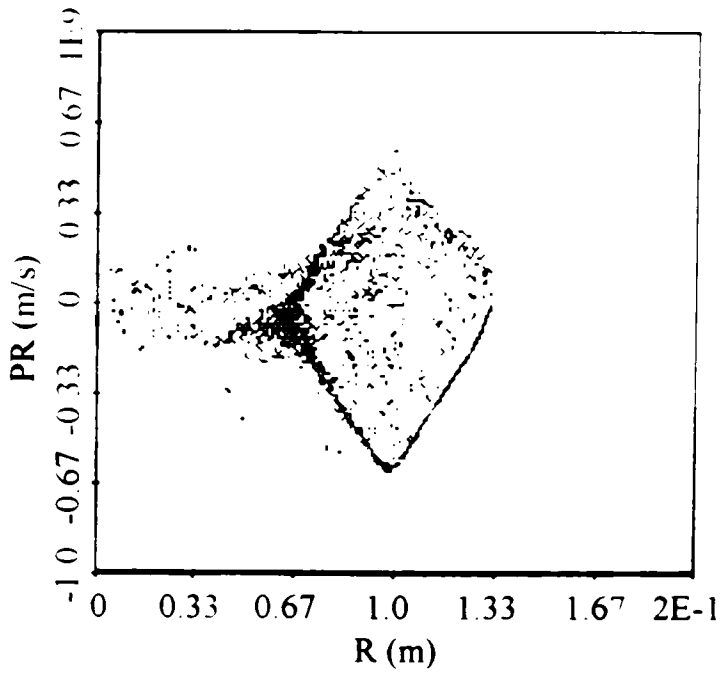

(b)

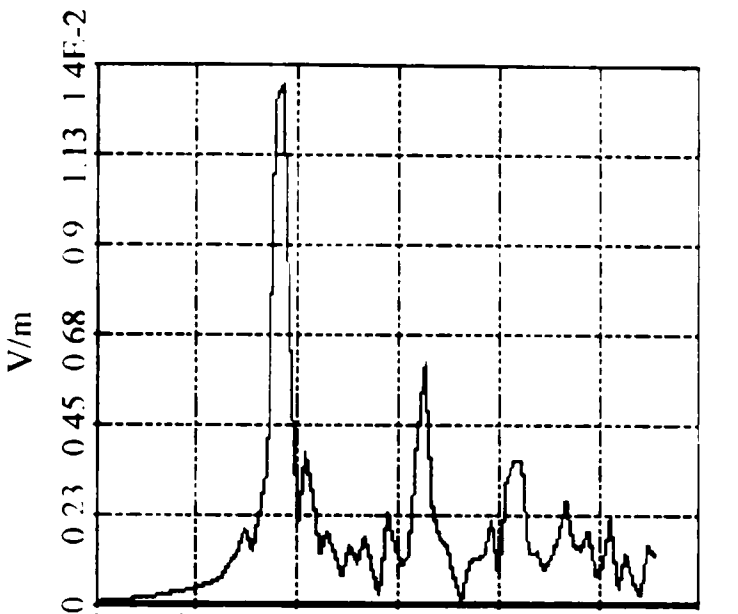

(c)

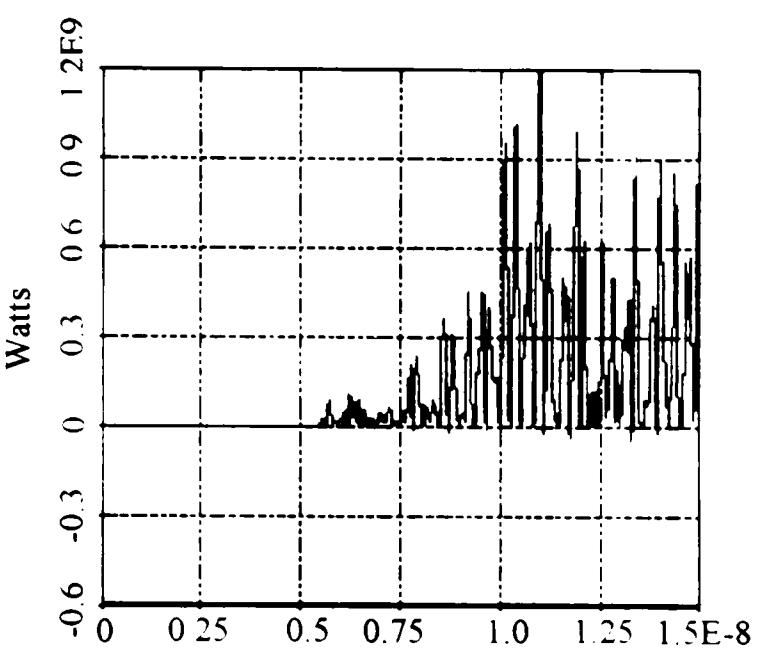

(d)

Table 3.14: Results for the Geometry with a 1.25" Strip, High Voltage.
(a) Particle position @ 5 ns, (b) r versus ρ_r phase space @ 5 ns, (c) E_r at wall versus frequency, (d) Output microwave power

Table 3.14: Results for the Geometry with a 1.25" Strip, High Voltage

Parameter	Value
Diode Voltage (V_d)	700 kV
Diode Current (I_d)	40 kA
Diode Impedance (Z_d)	17.5 Ω
Beam Power (P_{beam})	28 GW
Microwave Frequency (f)	1.69 GHz
Microwave Power (P_{mw})	1.2 GW
Power Efficiency (η)	4.29 %

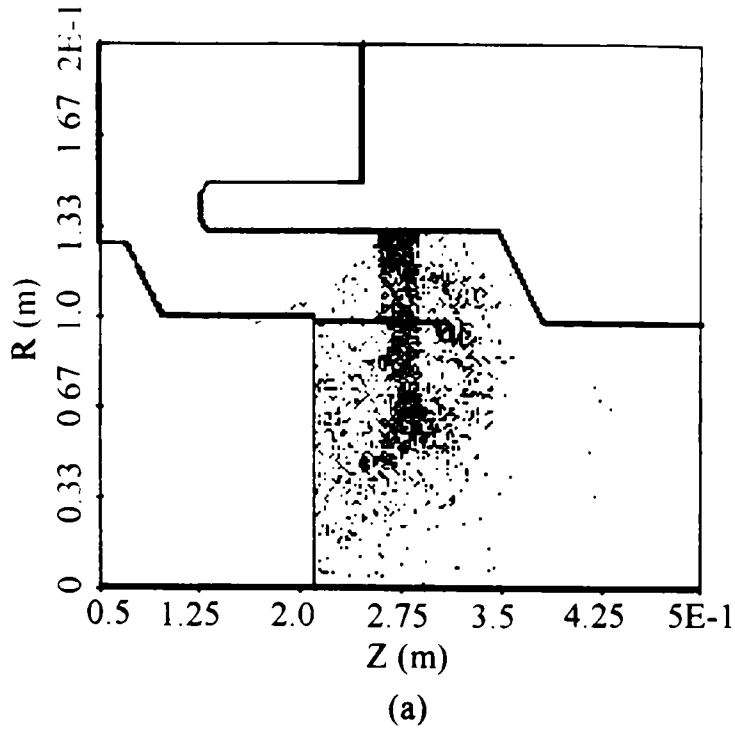

(a)

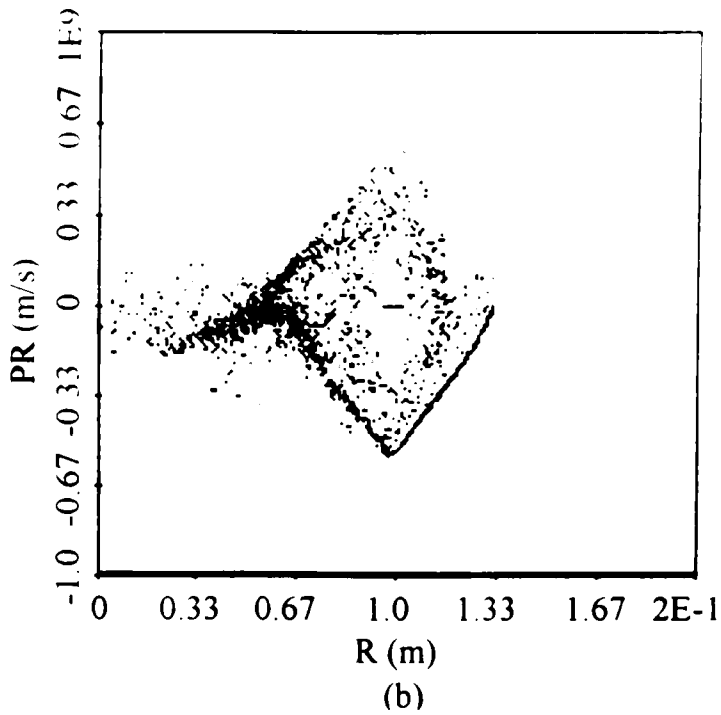

(b)

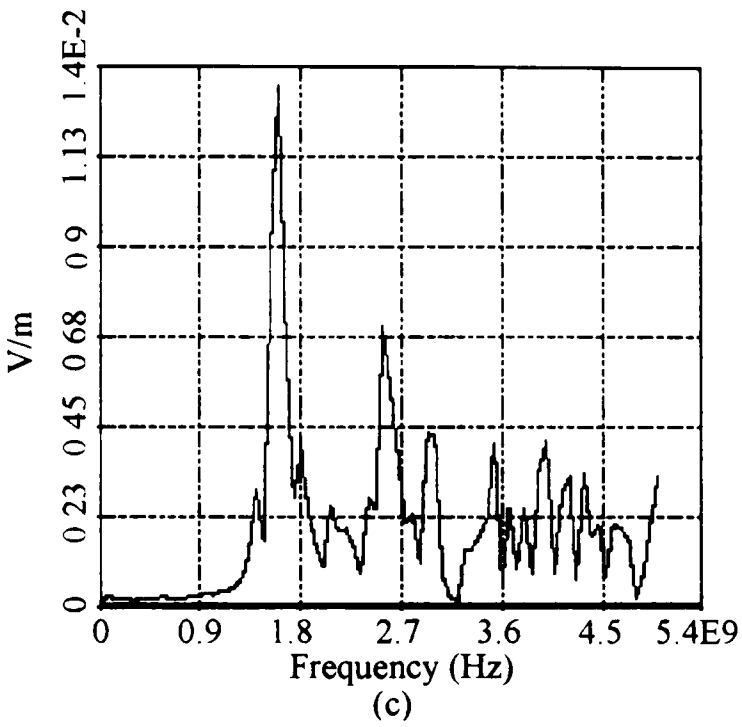

(c)

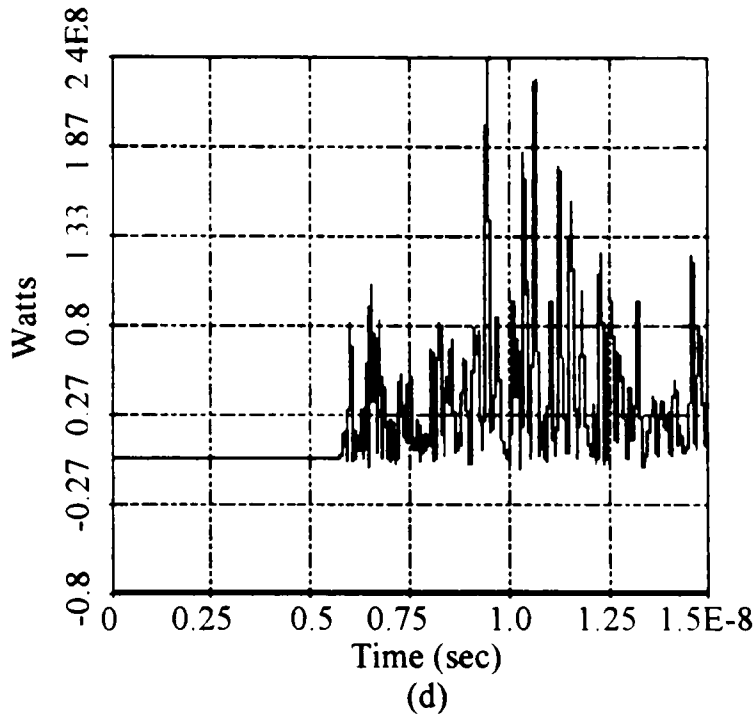

(d)

Figure 3.15: Results for the Geometry with a 1.25" Strip, Low Voltage.
(a) Particle position @ 5 ns, (b) r versus ρ_r phase space @ 5 ns, (c) E_r at wall versus frequency, (d) Output microwave power

Table 3.15: Results for the Geometry with a 1.25" Strip, Low Voltage

Parameter	Value
Diode Voltage (V_d)	540 kV
Diode Current (I_d)	30 kA
Diode Impedance (Z_d)	18 Ω
Beam Power (P_{beam})	16.2 GW
Microwave Frequency (f)	1.62 GHz
Microwave Power (P_{mw})	0.24 GW
Power Efficiency (η)	1.48 %

CHAPTER 4
DIAGNOSTICS

4.1 Beam Diagnostics

In microwave experiments, the diagnostics of the experiment are important in order to be able to accurately gather pertinent data so as to gain an understanding of the device under investigation. The data gathered in the vircator experiment are aimed at determining the efficiency and the cause for the change in the performance of the device. The efficiency is defined as the maximum instantaneous output power divided by the maximum instantaneous input diode power. The input power is defined as the voltage across the diode multiplied by the diode current at the same time.

To measure the diode voltage, one of the six pre-pulse resistors was configured into a voltage divider circuit. The purpose of the divider circuit is to bring the voltage to a level that can be measured. A schematic of the resistive divider circuit is shown in Figure 4.1.

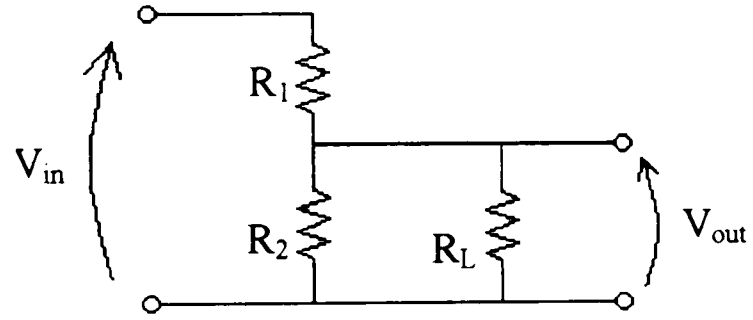

Figure 4.1: Resistive Divider Schematic

The relation of input voltage to output voltage in the divider circuit is:

$$V_{out} = \frac{R_2 \| R_L}{R_2 \| R_L + R_1} V_{in}. \qquad (4.1)$$

For the installed circuit, R_1 is one of the six pre-pulse water resistors, each with a value of 3000 Ω. The water resistors are a mixture of copper sulfate and de-ionized water enclosed inside 4040A Tygon tubing with copper end plugs. A picture of the converted water resistor lying next to a ruler is shown in Figure 4.2. This design allows

them to be immersed in transformer oil without deterioration of the tubing from the oil and to withstand high voltages. A drawback of the water resistor is that they change value over time and from the stress of a high, applied voltage. Frequent monitoring of the resistors is performed to keep the values close to the designed value for accurate data readings. R_2 is the parallel combination of three 1 Ω carbon resistors for a total resistance of one-third ohm. R_L is the load resistance and has a value of 50 Ω.

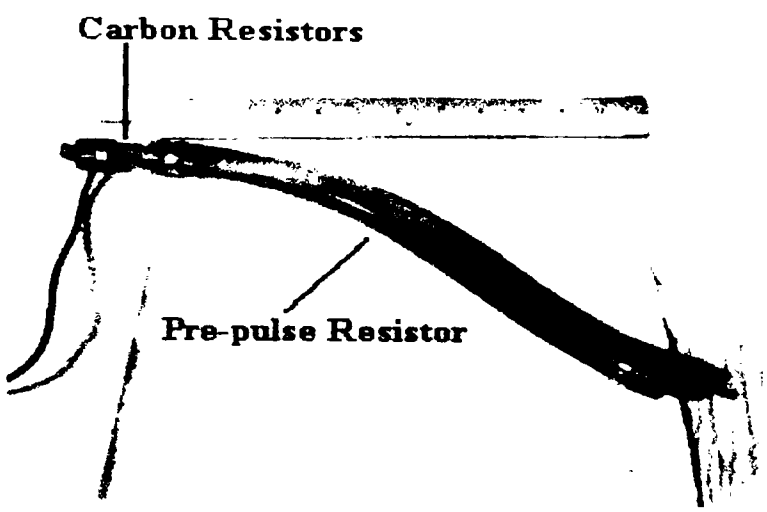

Figure 4.2: Pre-pulse Resistor

Since the rise time of the voltage pulse is on the order of a nanosecond, the effects of stray capacitance and stray inductance in the 1Ω carbon resistors used in the voltage divider circuit has a significant effect on the shape of the measured voltage pulse. For a linear system, the following relation holds:

$$V_{output}(\omega) = H(\omega)V_{input}(\omega) \quad , \tag{4.2}$$

where $V_{output}(\omega)$ is the Fourier transform of the voltage waveform measured from the divider circuit, $H(\omega)$ is the impulse response of the divider circuit in the frequency domain and $V_{input}(\omega)$ is the Fourier transform of the actual waveform. To compensate for the effects of the divider circuit the transfer function needs to be found and then $V_{output}(\omega)$ is divided by the transfer function in the frequency domain to obtain the actual voltage input waveform in the frequency domain which can be transformed back into the time domain to give the actual input voltage function.

To find the impulse response $H(\omega)$, an input signal is split in two with one signal being attenuated the same amount as the voltage divider circuit and captured and the other signal being input into the divider circuit and the output captured. Then the signals are transformed into the frequency domain and the first signal divided by the second signal to give the impulse response. This impulse response can then be used to find the actual waveform form the output of the divider circuit. Figure 4.3 shows both the uncompensated and compensated waveforms. Since a timing mark was placed on the voltage waveform, this too gets altered by the transformation process which effectively "smears" out the timing mark. The timing mark before and after compensation occurs before the voltage waveform and at a low magnitude compared to the voltage waveform. This leaves a good representation of the voltage waveform. It should be noted that the voltage measured is not the actual diode voltage. The measured voltage is related to the diode voltage by the following relation:

$$V_{measured}(t) = V_{diode}(t) + L\frac{dI_{diode}(t)}{dt} \tag{4.3}$$

where $V_{measured}$ is the waveform from the divider circuit, I_{diode} is the diode current and V_{diode} is the actual diode voltage. The "spikey" appearance of the diode voltage waveform is caused by reflections between the oil switch and the vacuum chamber, which appear as small transmission lines for the time scales involved [10]. The main voltage pulse is approximately 50 ns wide. The main signal pulse begins at 38 ns and stays on for about 25 ns, followed by a lower level pulse of 25 ns due to reflections from the load, followed by an exponential decay.

The diode current is measured by a slow-wave Rogowski coil. The measured current is the actual diode current, but due to the construction of the Rogowski coil, the waveform is only valid for 70 ns, twice the transit time of the coil. But since the main portion of the diode current in the experiment is only 50 ns, the Rogowski coil provides an accurate waveform. A typical current waveform is shown in Figure 4.4. For more information on the diagnostics of the voltage and current waveforms, the reader should see Ref [16].

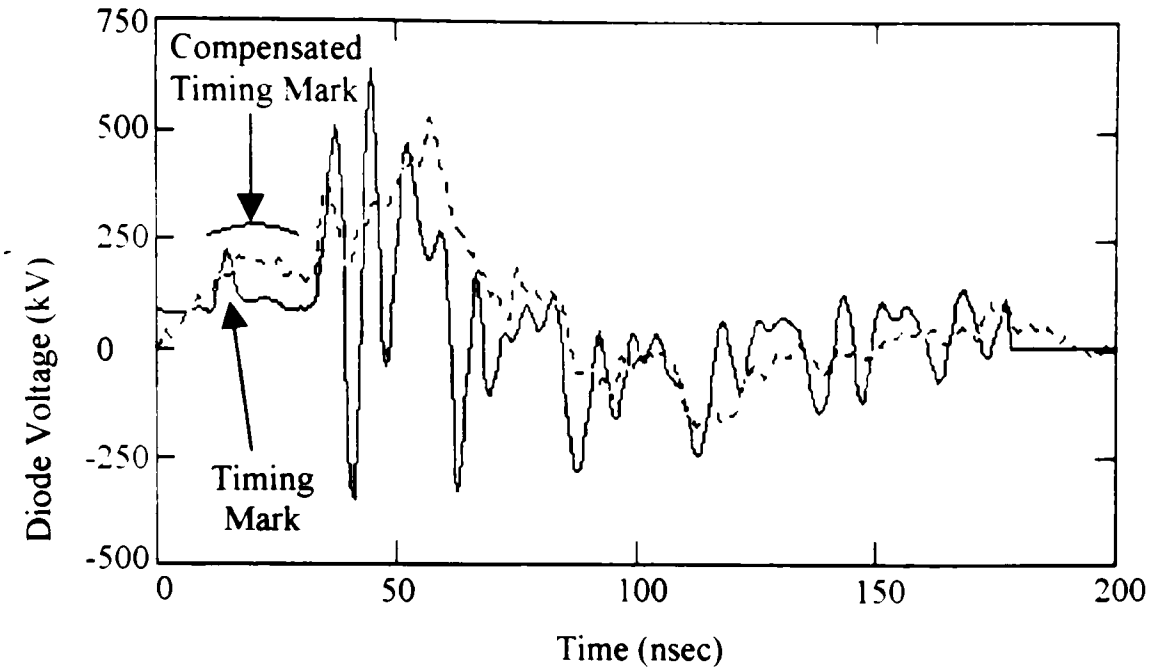

Figure 4.3: Voltage Waveforms, solid line – uncompensated waveform
Dashed line – compensated waveform

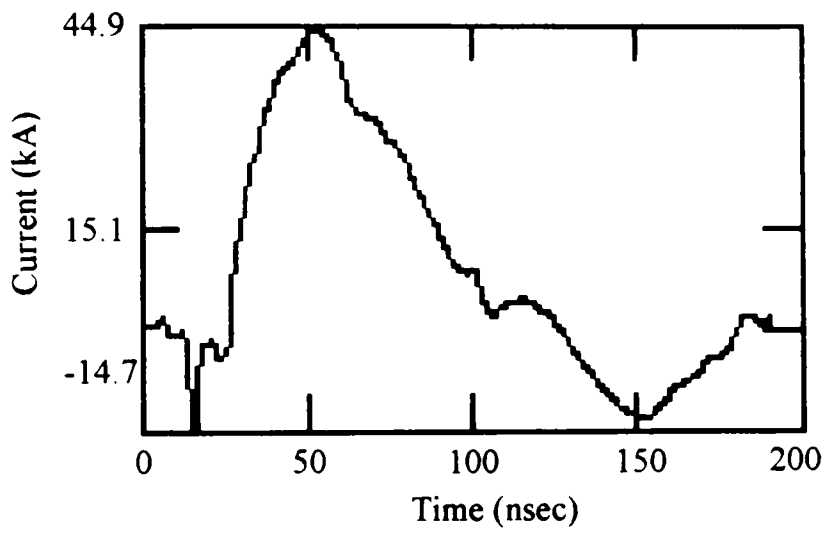

Figure 4.4: Typical Current Waveform

The beam power is calculated with:

$$P_{beam}(t) = V(t)I(t) \tag{4.4}$$

where V is the diode voltage and I is the diode current. A typical waveform for the beam power is shown in Figure 4.5. It should be noted that the beam power measured is larger than the actual beam power since the diode voltage measured is larger than the actual diode voltage by the relation given in Equation (4.3). The higher than actual diode voltage results in an apparent lower microwave power efficiency.

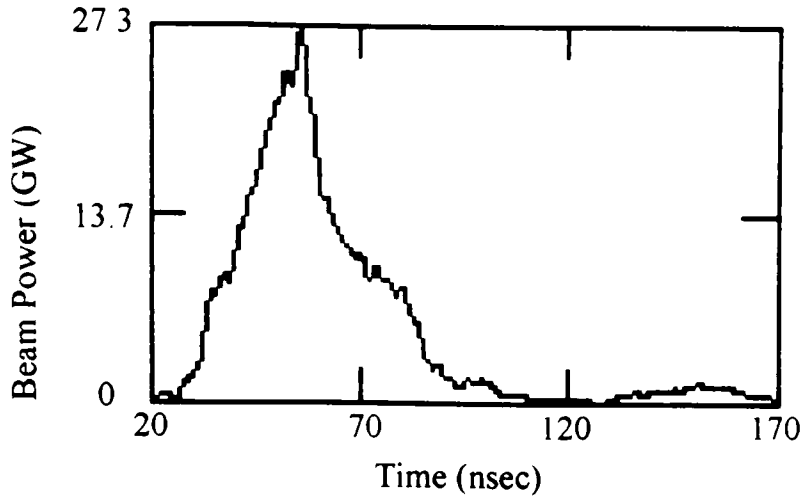

Figure 4.5: Typical Beam Power Waveform

4.2 Microwave Diagnostics

Accurately determining the operation of a vircator is difficult in itself. Being able to accurately extract microwave data from the vircator is even more difficult, especially with limited resources. The main problem with resources was that data need to be taken with oscilloscopes, and since the vircator's operating frequency was around the 2 GHz range, a fast scope is required. Previously, 1 GHz analog scopes were available and expensive, but this still did not reach the 2 GHz range. An addition to the problem was the fact that a limited window on the oscilloscope allowed viewing of only a portion of the signal at a time. As an example, if the scope's horizontal setting is 2 nanoseconds per division, only 16 nanoseconds could be viewed at a time and if the signal lasts about 70 nanoseconds, as is the case for our vircator, an accurate picture of the signal is difficult to obtain. Now, digital oscilloscopes are available to us with bandwidths greater than 2 GHz.

Another problem with the determination of the operation of the vircator lies in how the vircator behaves. Typically, the vircator is a device with many frequencies and many modes. Usually, one mode is dominant over the others, based on the geometry of the device, but others will still exist and this causes problems with power measurements. If only one mode is assumed, the measured power will be inaccurate, especially if the other modes contribute to a large portion of the signal. Also, some modes and frequencies may exist at the same time.

Most devices used to measure power are frequency dependent and may not cover a large enough bandwidth for the device being studied. A calorimeter is an example. In a calorimeter, power is absorbed into a liquid and the change in temperature of the liquid is an indicator of the power from the device. But the calorimeter is designed for a range of frequencies for near total absorption of the microwaves. The cause for this frequency dependence lies in the reflection from a plane wave incident on a medium of one permittivity sandwiched between media of other permittivities. Hence, a measurement scheme needs to be created that accounts for the frequency and mode differences of the vircator.

In determining the required diagnostics for the vircator, the range of frequencies needs to be determined. This was accomplished with a Hewlett Packard digital oscilloscope that has the capability of sampling at the rate of eight giga-samples per second. With the Nyquist criteria of sampling at twice the source frequency, a bandwidth of 4 GHz can be viewed on the digital oscilloscope. The high frequency signal was taken from a radial E-field probe near the output of the extraction waveguide as shown in Figure 4.6.

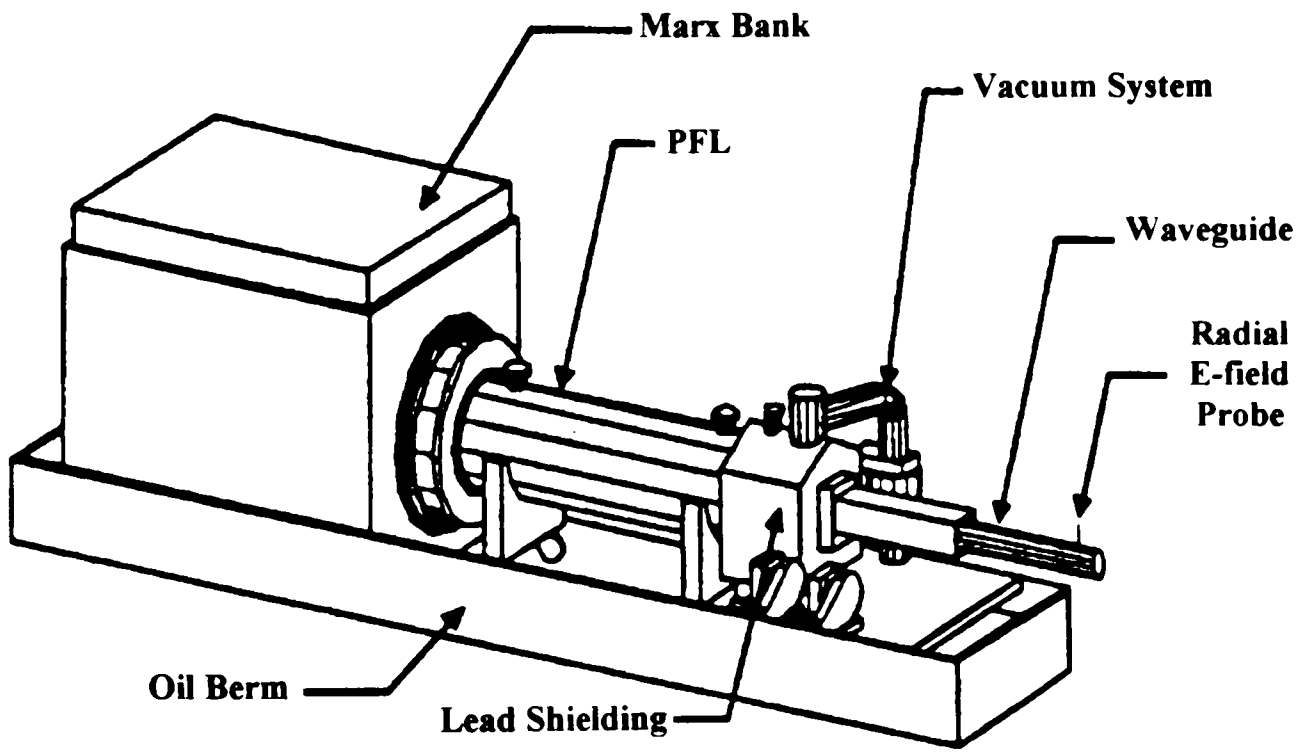

Figure 4.6: Schematic of the Coxial Vircator System

Two radial E-field probes were installed into the system, 90 degrees apart, in the same plane, to determine the polarization of the fields with one variation in the azimuthal direction. The radial E-field probes used to make the high frequency measurements were originally described in a paper by Burkhart [17]. The probes implemented in the system are usable in high vacuum, capable of measuring high electric fields without breaking down and do not protrude into the area being tested, thus not causing significant perturbations in the device which disturb the fields being measured. Figure 4.7 shows a diagram of a probe installed in the waveguide. The design of the probe requires that the radial electric field have a wavelength that is much larger than the dimension of the inner conductor of the probe. If this is true, a quasi-static condition exists over the area of the probe at any given instant in time. The surface charge on the probe is given by:

$$Q(t) = KD_r(t) \quad , \tag{4.5}$$

where K is the effective area of the inner conductor (m^2), and D_r is the electric flux density on the inner conductor (C/m^2). A close-up of the probe can be seen in Figure 4.8. In Figure 4.8,Φ is the potential, E_r the radial electric field and ε_r the relative permittivity of the insulating dielectric.

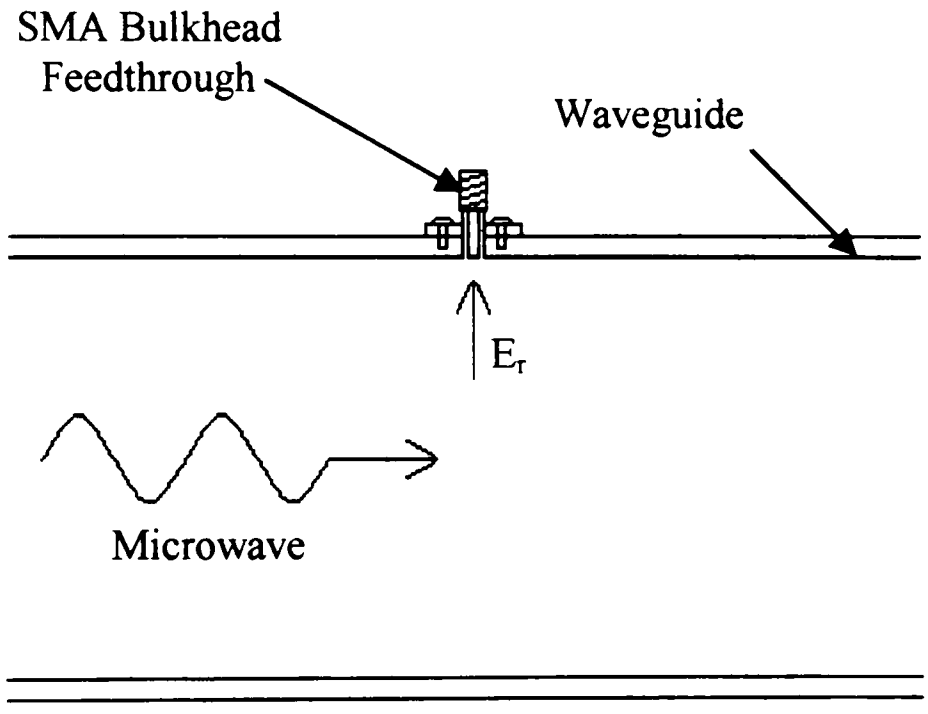

Figure 4.7: Radial E-field Probe Diagram

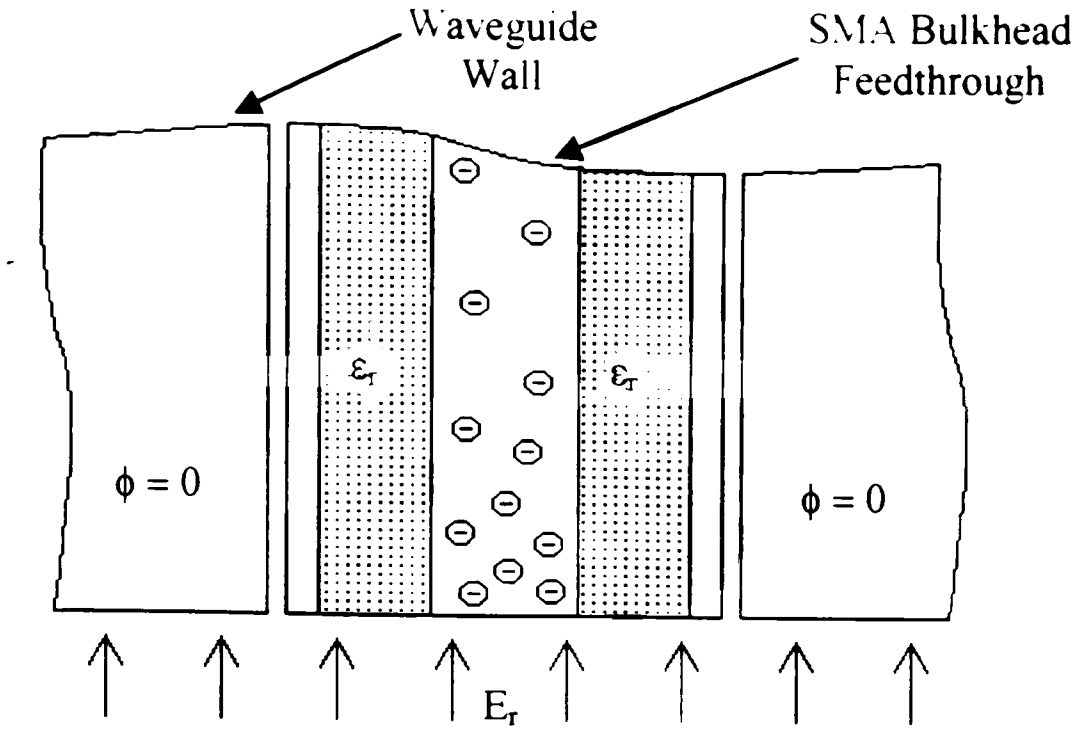

Figure 4.8: Close-up of the Radial E-field Probe

For a sinusoidal radial electric field, the current can be found by:

$$I(t) = \frac{dQ(t)}{dt}. \tag{4.6}$$

The resulting power is found with:

$$P = \frac{1}{2}|I|^2 Z_0 = \frac{Z_0}{2}[\omega \varepsilon_0 E_r K]^2, \tag{4.7}$$

where ω is the radian frequency of the electric field, ε_0 is the permittivity inside the waveguide (F/m), E_r is the radial electric field (V/m), and Z_0 is the impedance seen from the probe to the measuring device (Ω). Finding K is the only thing needed to calibrate the E-field probes.

Calibration was performed with the use of a one-kilowatt magnetron at a frequency 2.544 GHz. This device was chosen since the frequency is close to the operating frequency of the vircator. The power is low compared to the output of the vircator but offers a constant source needed for calibration. The method of calibration was to place the magnetron's monopole sticking into the center of a cylindrical waveguide. This generates a TM_{01} with a known field and can be used to calibrate the

radial E-field probes if a calibrated probe is used to find the power in the waveguide at a test point.

The test probe is a commercial, calibrated B-dot probe. The B-dot probe outputs a signal which is the time derivative of the magnetic field intercepted by the loop of the probe. For a sinusoidal magnetic field, a relation for the output power is given by:

$$P_{out} = \frac{B^2 A_{eff}{}^2 \omega^2}{2Z_0} \quad , \tag{4.8}$$

where B is the magnetic flux density intercepted by the probe (T), A_{eff} is the effective area (m^2), ω is the radian frequency of the microwaves, and Z_0 is the impedance seen by the probe (Ω). With the power determined from the B-dot probe, the value of K for the E-field probes is found, calibrating the E-field probes. For more details on the calibration of the E-field probes, the reader is directed to Ref. [10].

After calibrating the probes, the vircator diode was re-aligned with the anode-cathode gap varying by at most half a millimeter. The two cases under investigation include the charging of each capacitor to a value of 32 kV (i.e. V_{diode} = 550 kV) for case one and 25 kV (i.e. V_{diode} = 425 kV) for case two. The waveform and Fourier transform for the radial E-field probe for the 32 kV charge is shown in Figure 4.9. The Fourier transform was calculated to determine the frequencies of operation in the vircator. This showed three distinct modes at three different frequencies, one at 1.825 GHz, a second at 2.1 GHz and a third at 2.85 GHz. These frequencies are measured at the centers of the three groups of frequencies in the Fourier transforms.

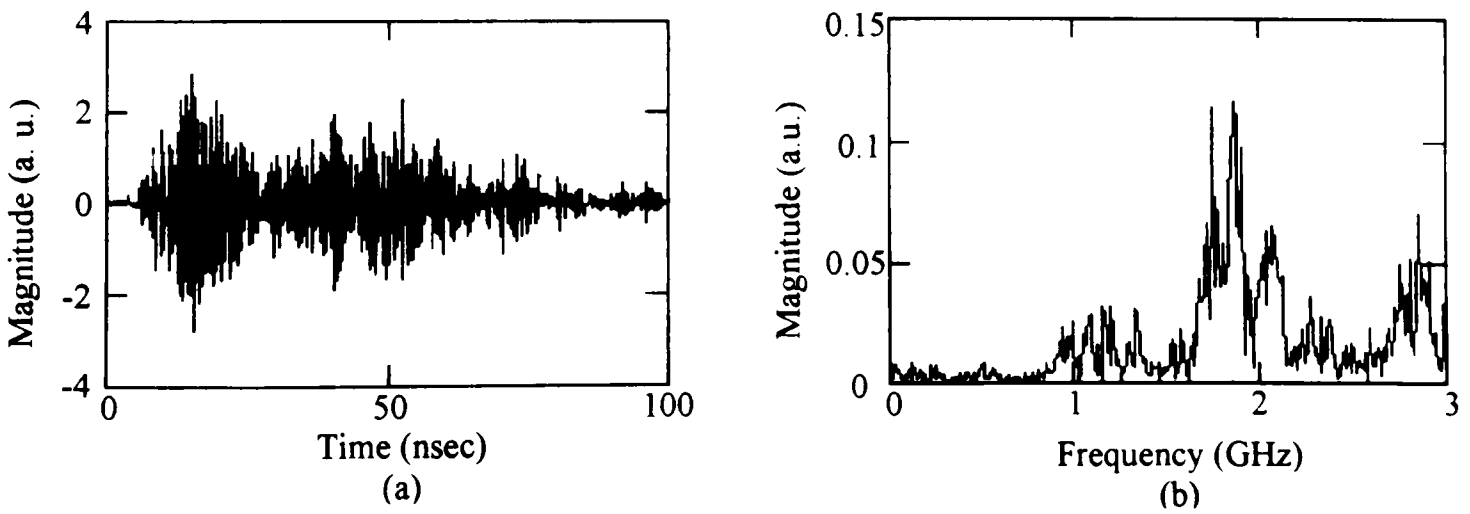

Figure 4.9: 32 kV waveform (V_{diode} = 550 kV). (a) radial E-field waveform, (b) FFT of waveform.

Investigation of the waveform revealed, by the use of windowing small portions of the waveform and taking the FFT, that the frequency spectrum was wideband over most of the pulse, but was dominated by one of the modes at all times. The frequency of the dominant mode started at the lowest and progressed to the highest value. Next, the mode for each of the groups of frequencies was determined. This was done to calculate the power accurately.

For a mode to propagate in a waveguide, the frequency of the microwave must be larger than the cut-off frequency of the mode for the waveguide. Thus, the largest frequency of the FFT was used in determining which modes can propagate. The cut-off frequency can be calculated with:

$$f_c = \frac{\chi_{mn}}{2\pi a\sqrt{\mu\varepsilon}} \quad , \tag{4.9}$$

where χ_{mn} is the n^{th} zero of the derivative of the Bessel function J_m of the first kind, of order m, for a TE mode or the n^{th} zero of the Bessel function J_m of the first kind, of order m, for a TM mode, a is the waveguide radius, μ is the permeability of the waveguide and ε is the permittivity of the waveguide. This gave a total of ten possible modes which are shown in Table 4.1 with the lowest ordered mode first and increasing down the table. If it is assumed that only one frequency corresponds to one mode and that the modes progress higher as the frequency increases, further information can be obtained. This limits the first three modes to the first frequency and the five modes beginning after the dominant mode, TE_{11}, to the second frequency. The final mode can be any higher order mode after the TM_{01}. The next step in determining which modes existed was the building and testing of mode filters. A diagram of a mode filter is shown in Figure 4.10.

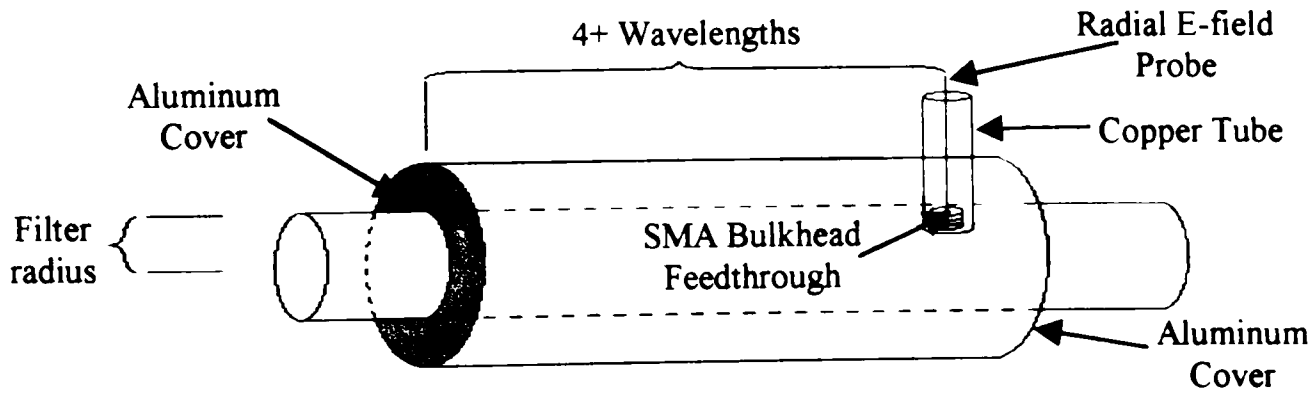

Figure 4.10: Mode Filter

Table 4.1: Cut-off Frequencies for Cylindrical Waveguide with 0.098 m Radius

Mode	Cut-off Frequency (GHz)
TE_{11}	0.89
TM_{01}	1.17
TE_{21}	1.48
TM_{11}	1.86
TE_{01}	1.86
TE_{31}	2.04
TM_{21}	2.49
TE_{41}	2.58
TE_{12}	2.58
TM_{02}	2.68

The mode filter is designed to capture the microwaves that propagate out of the original waveguide, into a waveguide with a smaller radius. This smaller radius increases the cut-off frequncy of all the modes which allows fewer modes to propagate in the smaller waveguide. The radial electric field is then captured and an FFT is again performed. The length of the input of the filter to the radial E-field probe is larger than four wavelengths to allow modes that are cut-off to die out. Two mode filters were constructed, a large filter with a radius of 0.0607 meters, and a small filter with a radius of 0.0492 meters. Table 4.2 shows the mode and cut-off frequencies for the large and small filter. Figure 4.11 shows the radial E-field waveform from the large filter and the FFT of the waveform with the cut-off values indicated. Figure 4.12 shows the radial E-field waveform from the small filter and the FFT of the waveform with the cut-off values indicated.

Table 4.2: Filter Mode Cut-off

Mode	Cut-off frequency for Large Filter (GHz)	Cut-off frequency for Small Filter (GHz)
TE_{11}	1.45	1.78
TM_{01}	1.89	2.33
TE_{21}	2.40	2.96
TM_{11}	3.01	3.71

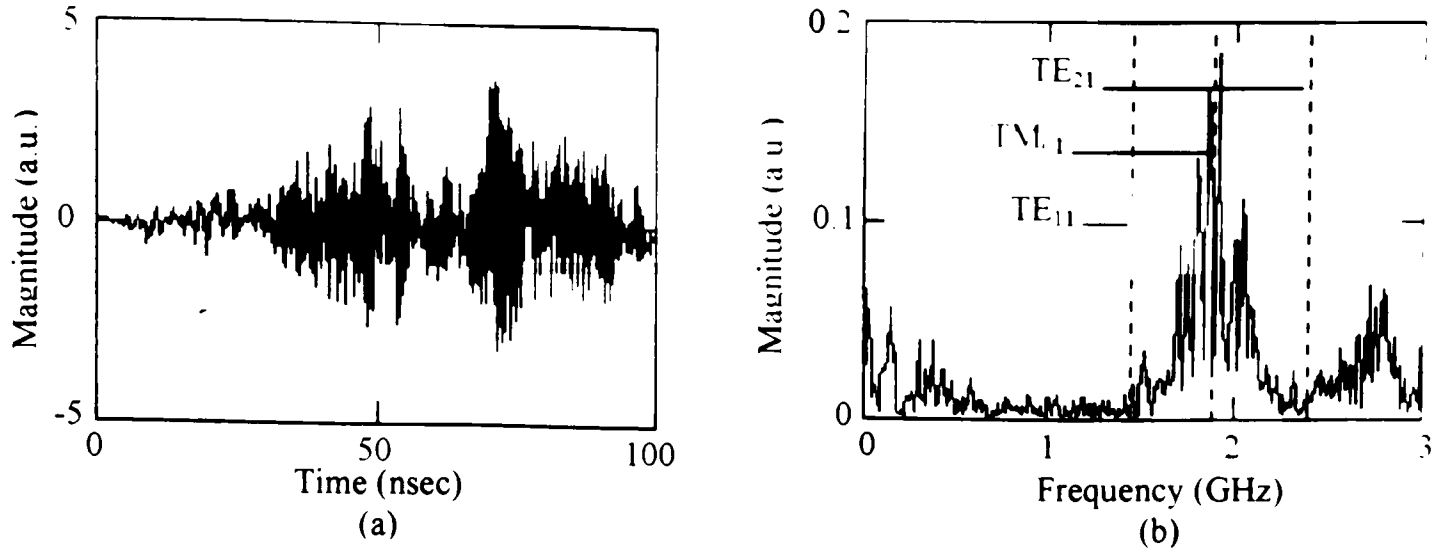

Figure 4.11: 32kV Waveform with Large filter (V_{diode} = 550 kV). (a) Large filter, radial E-field waveform, (b) FFT of the Large filter waveform.

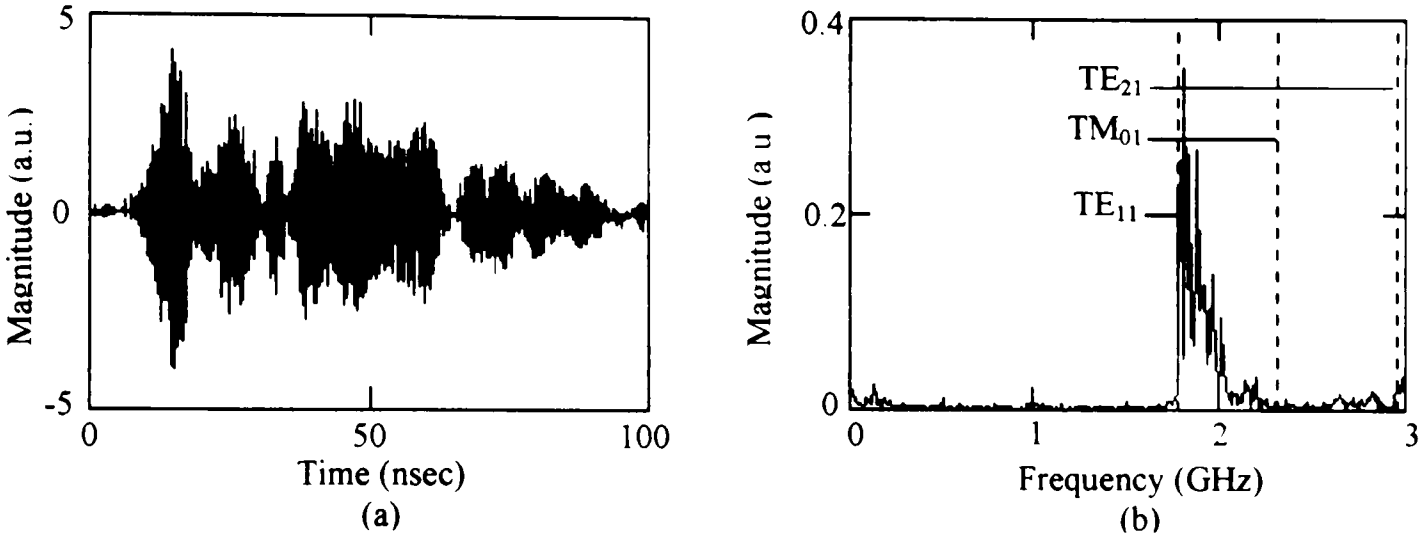

Figure 4.12: 32kV Waveform with Small filter (V_{diode} = 550 kV). (a) Small filter, radial E-field waveform, (b) FFT of the Small filter waveform

Comparing the two FFT outputs with the cut-off frequencies allows the modes to be determined. The small filter FFT output shows that frequencies below 2 GHz must be a TE_{11}. Since the cut-off frequency of any other mode is above 2 GHz, it cannot propagate. This figure also shows that any frequency above 2 GHz is not a TE_{11} mode. This is because it would have propagated and been present in the figure since frequencies above 2 GHz are above the TE_{11} cut-off. For the mode just above 2 GHz, a comparison of the two figures is needed. In the large filter FFT figure, the signal just above 2 GHz propagated when the cut-off of the TM_{01} mode was below this frequency. The cut-off for the next higher mode, TE_{21}, for the large filter is at 2.4 GHz so this mode is not a possibility. Since we have already determined that the signal above 2 GHz is not a TE_{11},

this mode must be a TM_{01}. A similar argument is made for the remaining mode above 2.5 GHz. If it were a TM_{01}, it would have propagated in the small filter and been evident in the small filter FFT. In the large filter, the next highest mode, TM_{11}, has a cut-off of 3.0 GHz and since it was already determined that it was not a TE_{11} or TM_{01}, the mode above 2.5 GHz must be a TE_{21}.

Similar results are found for a charging voltage per capacitor of 25 kV. The original, unfiltered data are shown in Figure 4.13. The large and small filter outputs are shown in Figure 4.14 and 4.15, respectively. Using the same logic as was done with the 32 kV charge data, two modes are evident, a TE_{11} and a TE_{21}. For the low voltage case, only one frequency at 1.825 GHz is seen. In the high voltage case, two frequencies are present, one at 1.825 GHz and one at 2.1 GHz which are the plasma and reflexing frequencies, respectively. But in the low voltage case, the reflexing frequency drops to match the plasma frequency as described in section 2.1. This matching of frequencies results in a higher efficiency.

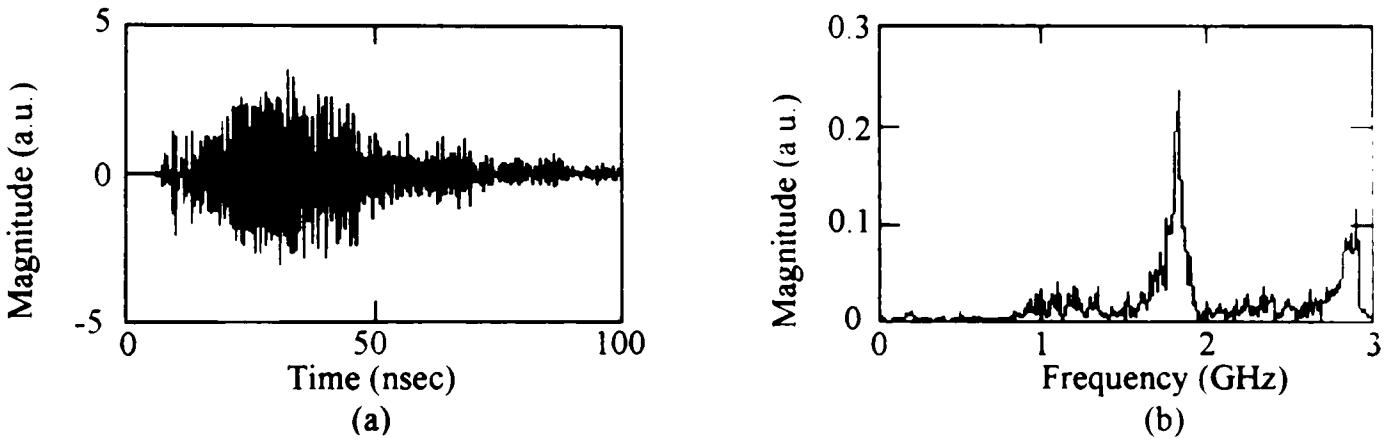

Figure 4.13: 25 kV Waveform (V_{diode} = 425 kV). (a) radial E-field waveform, (b) FFT of waveform

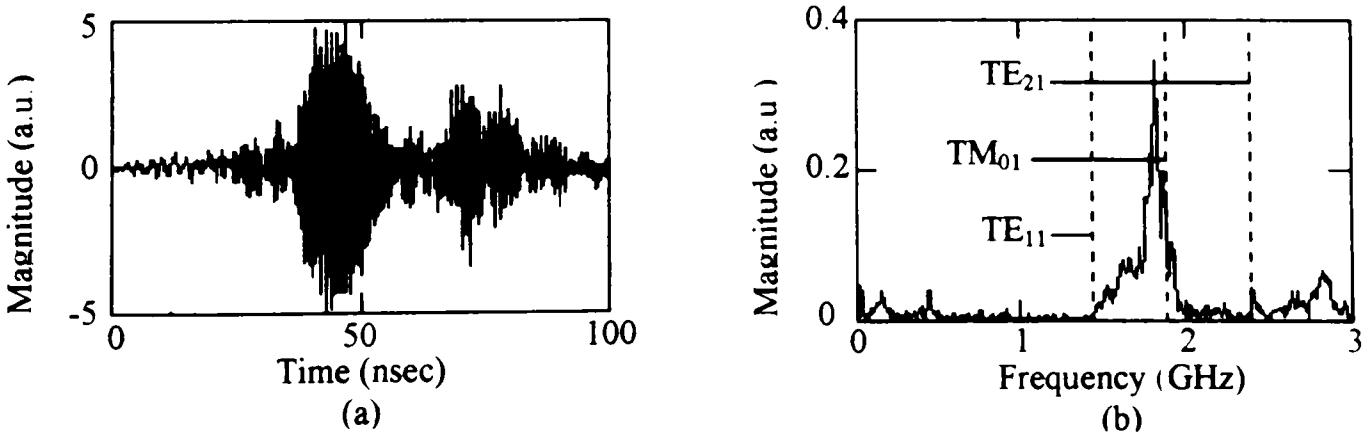

Figure 4.14: 25 kV Waveform with Large Filter (V_{diode} = 425 kV). (a) Large filter, radial E-field waveform, (b) FFT of the Large filter waveform.

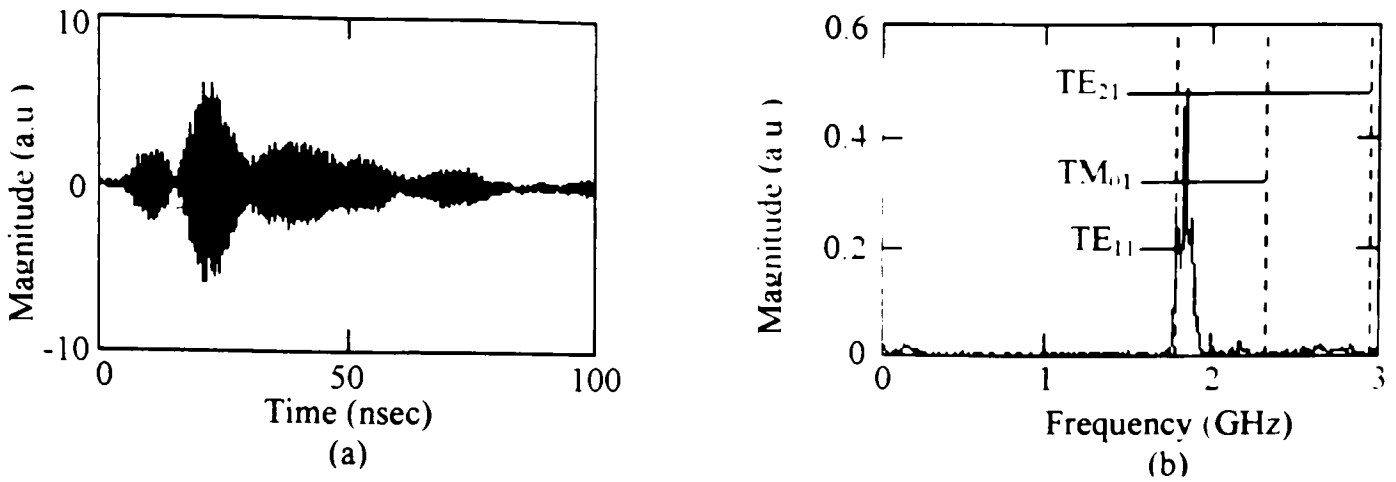

Figure 4.15: 25 kV Waveform with Small Filter (V_{diode} = 425 kV). (a) Small filter, radial E-field waveform, (b) FFT of the Small filter waveform.

Now that the possible modes and their relative frequencies have been determined, it should be noted that these modes and frequencies are the results of a carefully aligned diode. But changing the velvet on the cathode needs to be performed often and a re-alignment of the diode may be difficult and, most importantly, it will not be aligned exactly as before. Due to these difficulties, specially careful alignment will not be attempted. This will generate a TE_{11} mode as discussed in section 2.2, which is not necessarily unwanted.

The method of determining the output power is to take the rf electric field from the two E-field probes previously discussed, attenuate them, then run the signals through crystal diode detectors, obtaining electric field envelopes. Since a TE_{11} mode has a polarization, the electric field envelopes can be used to determine the time dependent polarization with:

$$\phi(t) = \tan^{-1}\left(\frac{E_2(t)}{E_1(t)}\right) , \qquad (4.10)$$

where E_1 is the time dependent power envelope at one of the E-field probes and E_2 is the time dependent power envelope at the other E-field probe. Figures 4.16 and 4.17 show typical electric field envelopes from the E-field probes and the time dependent polarization waveform, respectively.

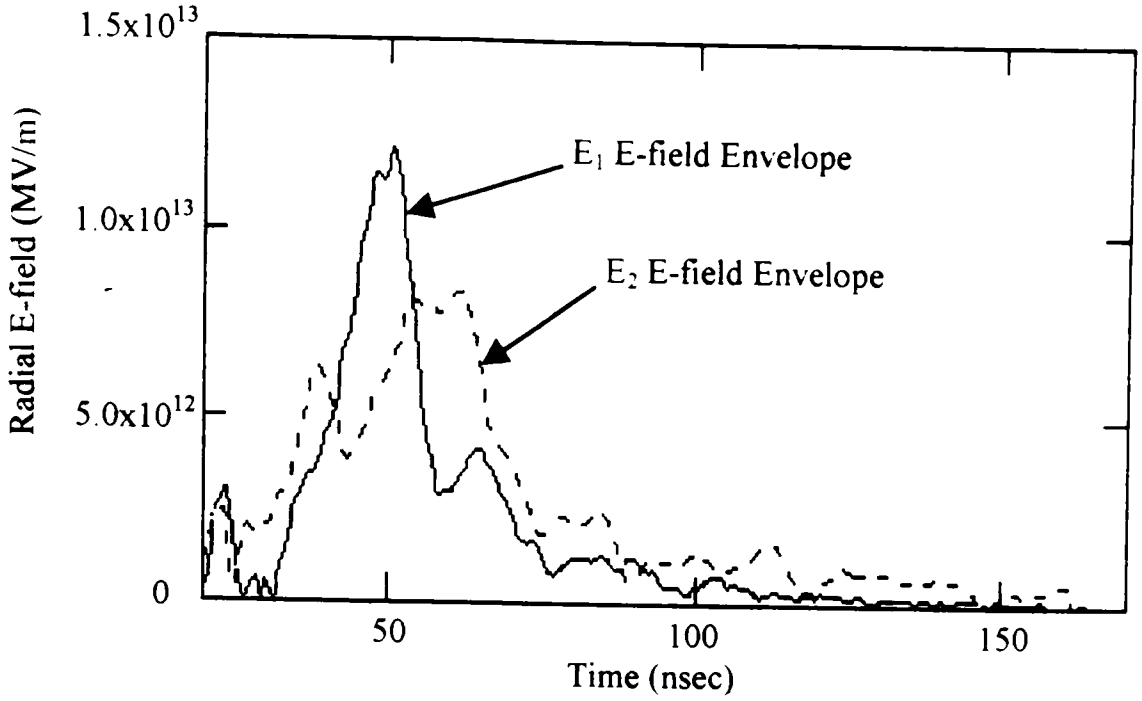

Figure 4.16: Typical Electric Field Envelopes

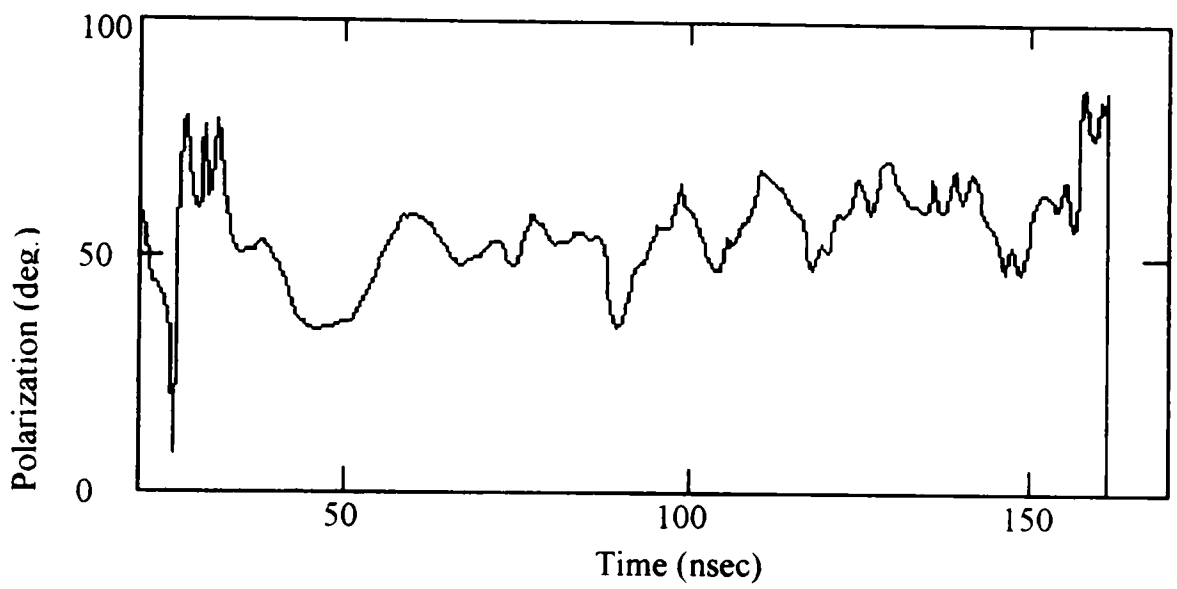

Figure 4.17: Polarization from Electric Field Envelopes

The microwave power density can then be found with:

$$S = \frac{E_\rho^2}{2Z_w} \tag{4.11}$$

where E_ρ is radial electric field and Z_w is the wave impedance. Since the wave impedance is a function of frequency, the only thing needed to find the output power is the microwave frequency. This was found with another E-field probe like the probes

discussed previously Calibration of this probe is not needed since the frequency is the only parameter of interest. The rf output from this E-field probe is not run through a crystal diode detector but captured directly with a digital oscilloscope with a bandwidth larger than the operating frequency of the vircator. The FFT of this signal then tells the microwave frequency A typical FFT of a captured rf signal is shown in Figure 4.18.

Now with the power density at a known location and the polarization of the TE_{11} mode in relation to that position known, an integration over the surface of the waveguide is performed to obtain the microwave power waveform. A typical microwave power waveform is shown in Figure 4.19. The pulse width is approximately 50 ns. The main pulse begins about 38 ns and stays on for about 50 ns, this corresponds to the 25 ns main voltage pulse applied to the diode and the 25 ns reflection pulse. The trailing tail of the pulse corresponds to the exponential decay of the potential across the diode.

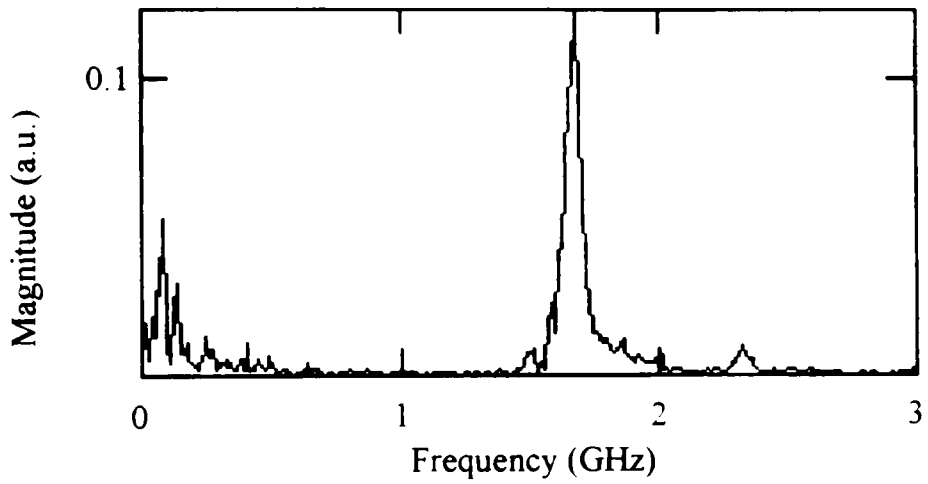

Figure 4.18: FFT of RF Waveform from the Coaxial Vircator

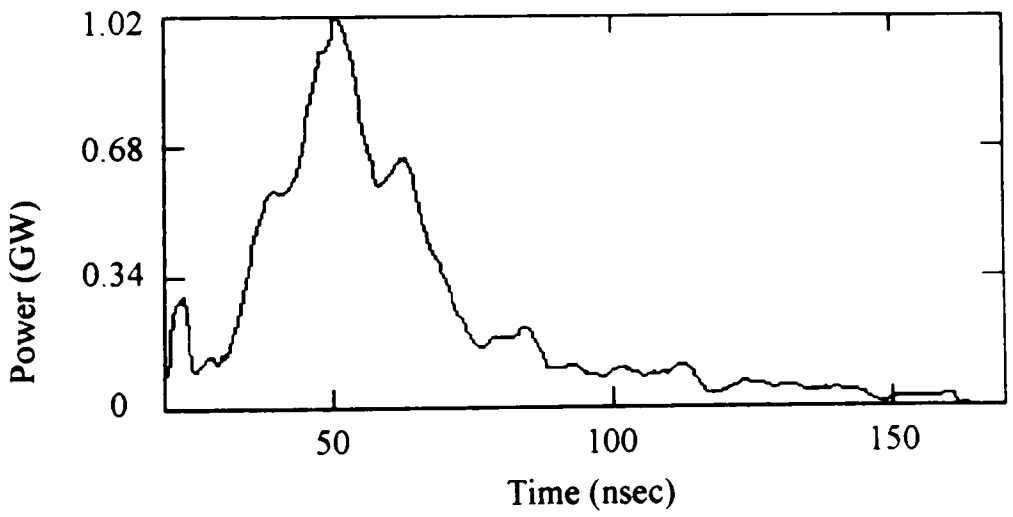

Figure 4.19: Typical Microwave Power Envelope

It should be noted that since the output waveguide is not terminated with a matched load, reflections exist. Also, the probes used cannot distinguish between forward and backward travelling waves so the measured power will not necessarily be the actual power delivered to a matched load.

CHAPTER 5
EXPERIMENTAL RESULTS

The experiments on the coaxial vircator were aimed at changes in the diode region that keep the device simple to determine if the coaxial vircator would produce high output power at high efficiencies. The changes to the diode include various screen materials, placement of collection rods on axis in the diode, placement of a hole on axis in the center of the diode, varied applied voltages to the diode, the variation of the emitting material in size and position and a negative polarity geometry. A total of eleven different positive polarity geometries were tested, each of the eleven geometries were tested at two voltage levels except one geometry for which the current was so low that the timing mark generator would not trigger and only one case is given for this geometry. A total of twenty-one experiments, given in Section 5.1, are presented for the positive polarity geometry. Section 5.2 contains the results for the negative polarity geometry.

5.1 Positive Polarity Geometries

The voltage level tests for the positive polarity geometry were performed by charging each capacitor to 25 kV for the low charging level and 32 kV for the high charging level. Since the diode voltage changes for individual cases, caused by the change in the impedance of the diode, from this point, any reference to low voltage refers to a per capacitor charge of 25 kV and high voltage will refer to a per capacitor charge of 32 kV. The actual diode voltage can be seen in the row for diode voltage in the corresponding table.

To be able to distinguish the effect of a given change in geometry, a standard geometry had to be established. The standard diode geometry is shown in Figure 5.1. The anode foil is a stainless steel mesh screen, 3.5 inches long, with a transparency of 70%. A velvet strip 4.5 inches long acts as the explosive emitter and is applied one inch away from the transition to get a full coverage of the anode screen.

The initial set of tests was aimed at changes made to the anode base structure. These changes include two different anode foil materials, a hole on axis and

two different rod geometries. The two different foils include a stainless steel mesh screen with larger wire than the standard geometry with a transparency of 69% and a foil made of aluminized kapton with a thickness of 1.34 mils. The larger wire is 0.017 inches in diameter with ten wires per inch and the small wire has 0.009 inch diameter with eighteen wires per inch. All other possible variables have been kept the same as for the standard geometry. Table 5.1 contains results from the standard geometry. Table 5.2 contains the results from the two different foils. The values in the tables, as well for all experimental data in the tables, are obtained by averaging the data obtained from three separate shots.

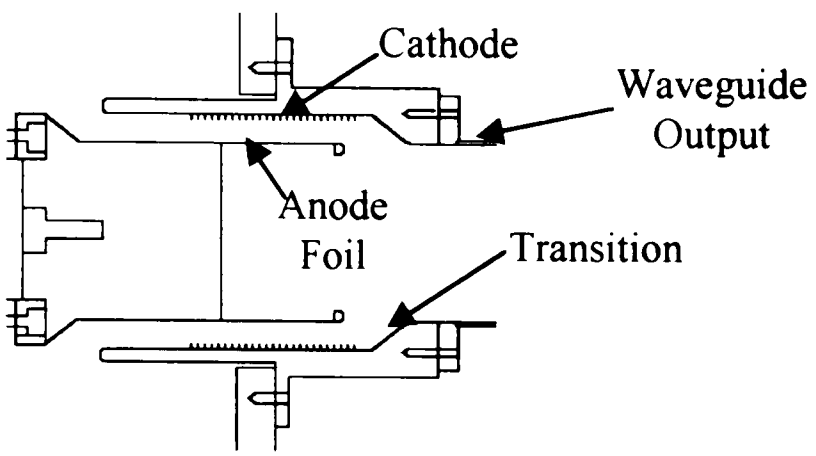

Figure 5.1: Standard Diode Geometry

Table 5.1: Standard Geometry Results

Test	Standard Geometry Low Voltage	Standard Geometry High Voltage
V_{peak} (kV)	421.92	531.97
I_{peak} (kA)	43.81	57.44
Z_{diode} (Ω)	9.63	9.26
f_{peak} (GHz)	1.87	1.69
BW (GHz)	0.35	0.42
P_{mw} (MW)	293.88	214.22
E_{mw} (J)	14.29	12.45
P_{beam} (GW)	18.33	30.39
E_{beam} (J)	458.35	669.57
η_{power} (%)	1.60	0.70
η_{energy} (%)	3.12	1.86

The variables in the table, and all experimental data in the following tables, are defined as follows:

V_{peak} = maximum diode voltage,

I_{peak} = maximum diode current,

Z_{diode} = diode impedance, V_{peak} / I_{peak},

f_{peak} = frequency with largest FFT magnitude,

BW = bandwidth of the output power from FFT,

P_{mw} = maximum microwave power,

E_{mw} = energy in the microwave pulse,

P_{beam} = maximum electron beam power,

E_{beam} = energy in the electron beam,

η_{power} = power efficiency, $(P_{mw} / P_{beam}) \times 100\%$,

η_{energy} = energy efficiency, $(E_{mw} / E_{beam}) \times 100\%$.

Table 5.2: Experimental Foil Results

Test	Aluminum Foil Low Voltage	Aluminum Foil High Voltage	Screen Mesh Low Voltage	Screen Mesh High Voltage
V_{peak} (kV)	383.88	467.55	349.11	497.74
I_{peak} (kA)	44.47	57.59	45.00	58.86
Z_{diode} (Ω)	8.63	8.12	7.76	8.56
f_{peak} (GHz)	2.125	2.20	1.74	1.69
BW (GHz)	0.55	0.60	0.39	0.54
P_{mw} (MW)	275.96	245.39	222.16	202.50
E_{mw} (J)	9.41	9.00	11.52	11.34
P_{beam} (GW)	16.71	26.67	15.42	28.93
E_{beam} (J)	390.22	609.43	372.39	629.26
η_{power} (%)	1.65	0.92	1.44	0.70
η_{energy} (%)	2.41	1.48	3.09	1.80

The second set of changes dealt with changes in the anode base structure. These included placing a hole in the center of the anode base, on axis, with a diameter of 0.902 inches and a depth of 0.7874 inches and the addition of two different sized collection rods screwed into the anode base, on axis, where the hole was. The purpose of the hole and

rods was to keep electrons out of the wrong-phased region by use of a retarding field. Figure 5.2 shows the diode geometry with the hole present and the diode geometry with the collection rod added. Table 5.3 shows the geometry variables seen in Figure 5.2 for the collection rods. The results from the geometries are shown in Table 5.4

Table 5.3: Collection Rod Parameters

Parameter	Rod #1	Rod #2
R_L (in.)	2.97	2.01
T_L (in.)	0.26	1.66
R_D (in.)	0.90	2.12

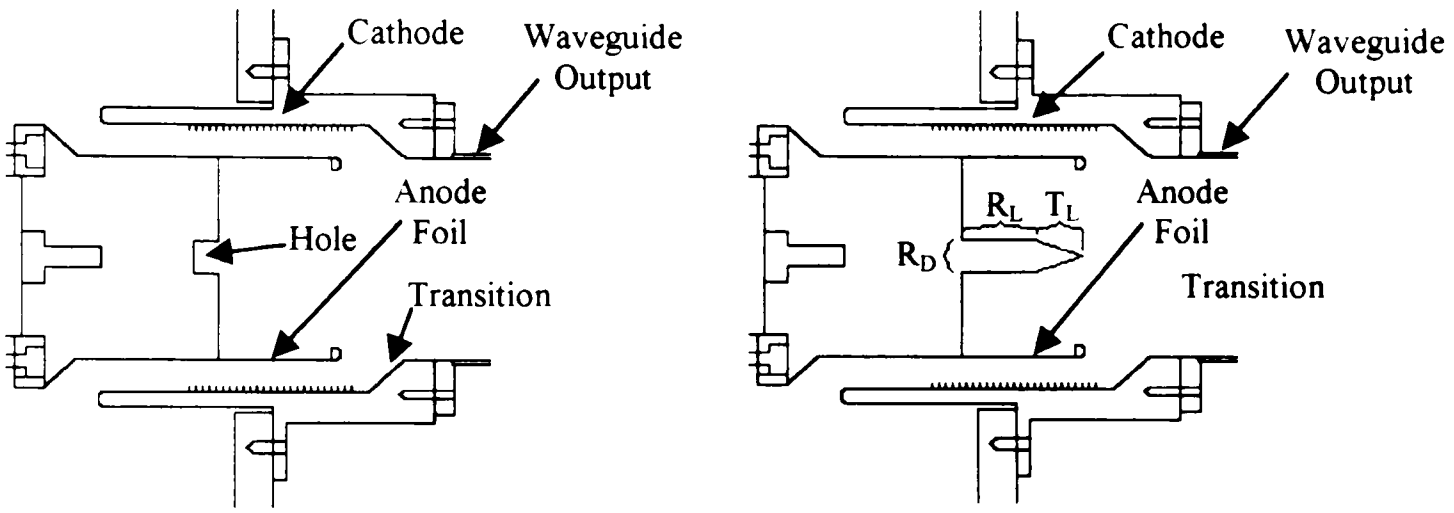

Figure 5.2: Hole and Rod Geometry

Table 5.4: Experimental Results for the Hole and Rod Geometries

	Hole Low Voltage	Hole High Voltage	Rod #1 Low Voltage	Rod #1 High Voltage	Rod #2 Low Voltage	Rod #2 High Voltage
V_{peak} (kV)	441.65	544.73	430.93	522.19	408.82	437.06
I_{peak} (kA)	44.39	59.73	45.60	58.01	44.77	59.70
Z_{diode} (Ω)	9.95	9.12	9.45	9.00	9.13	7.32
f_{peak} (GHz)	1.70	1.67	1.70	1.87	1.71	1.70
BW (GHz)	0.42	0.50	0.38	0.51	0.27	0.30
P_{mw} (MW)	307.98	224.76	247.80	199.18	180.35	172.35
E_{mw} (J)	15.24	13.62	11.72	11.45	8.96	10.10
P_{beam} (GW)	19.30	32.18	19.23	30.07	18.15	25.63
E_{beam} (J)	446.30	672.52	453.01	640.44	432.19	569.18
η_{power} (%)	1.60	0.70	1.29	0.66	1.00	0.67
η_{energy} (%)	3.41	2.03	2.59	1.79	2.07	1.77

The final experiments conducted include the variation of the size of the velvet lining the cathode and the placement of the velvet. The impetus for this work came from communication with people from Lawrence Livermore National Labs who reported high output power with narrow emitters [18]. Again, for each of these cases two different voltages were applied, one high and one low. Figure 5.3 shows the geometry of the diode with the placement of the velvet on the cathode. The distance of the center of the velvet lining the cathode to the transition to the waveguide is D_t and D_s is the width of the velvet lining the cathode. The anode is a cylindrical stainless steel mesh screen with a 70% transparency, 3.5 inches long, the same anode as the standard geometry. Table 5.5 contains the six different geometry parameters and Table 5.6 contains the results. The standard geometry is included as Test 1 for ease of comparison.

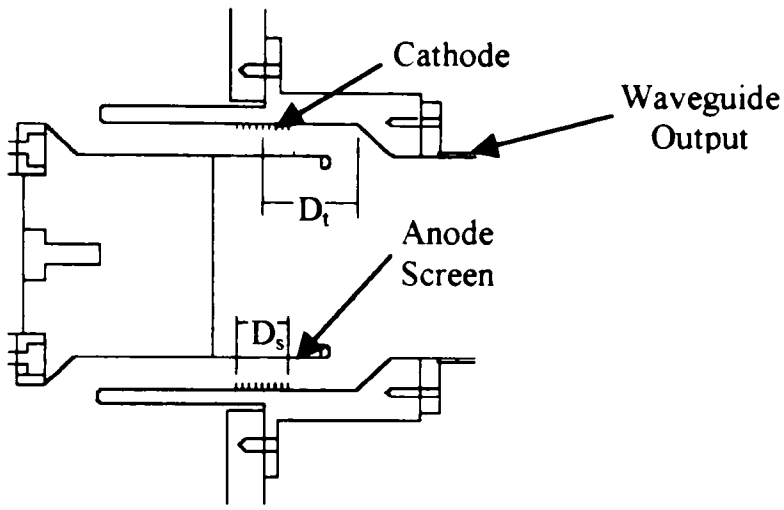

Figure 5.3: Coaxial Vircator Geometry for Narrow Strip

Table 5.5: Coaxial Vircator Geometry Parameters for Narrow Strip

	Test 1	**Test 2**	**Test 3**	**Test 4**	**Test 5**	**Test 6**
D_s (in.)	4.5	2.0	0.625	1.25	1.25	1.25
D_t (in.)	3.25	2.75	2.75	3.375	2.75	2.125

These results are the averages of three separate shots. But these data can hide singular shots that have extremely good results that might give some insight into how the physics of the vircator works and provide clues on how to make the vircator more efficient. Since the current results have shown high efficiencies, Table 5.7 contains the best efficiency case for each of these latest geometries.

Table 5.6: Coaxial Vircator Experimental Results with Narrow Strip (average of 3 shots)

	Test 1 Low Voltage	Test 1 High Voltage	Test 2 Low Voltage	Test 2 High Voltage	Test 3 High Voltage
V_{peak} (kV)	421.92	531.97	480.07	598.27	747.66
I_{peak} (kA)	43.81	57.44	37.78	48.20	37.99
Z_{diode} (Ω)	9.63	9.26	12.71	12.41	19.68
f_{peak} (GHz)	1.87	1.69	1.64	1.692	1.65
BW (GHz)	0.35	0.42	0.25	0.213	0.125
P_{MW} (MW)	293.88	214.22	554.09	701.80	980.63
E_{MW} (J)	14.29	12.45	22.56	30.72	38.84
P_{beam} (GW)	18.33	30.39	17.57	28.18	27.38
E_{beam} (J)	458.35	669.57	469.04	791.27	993.61
η_{power} (%)	1.60	0.70	3.15	2.49	3.58
η_{energy} (%)	3.12	1.86	4.81	3.88	3.91

Table 5.6: (continued)

	Test 4 Low Voltage	Test 4 High Voltage	Test 5 Low Voltage	Test 5 High Voltage	Test 6 Low Voltage	Test 6 High Voltage
V_{peak} (kV)	524.70	638.07	509.40	706.93	563.17	714.13
I_{peak} (kA)	34.97	45.28	34.04	44.92	32.17	41.69
Z_{diode} (Ω)	15.00	14.09	14.96	15.74	17.51	17.13
f_{peak} (GHz)	2.44	2.425	1.56	1.675	1.457	1.68
BW (GHz)	Large	Large	Large	0.15	0.245	0.41
P_{MW} (MW)	836.85	684.15	478.50	1162.69	429.95	760.37
E_{MW} (J)	30.95	29.40	19.87	45.68	19.42	35.78
P_{beam} (GW)	17.31	27.80	16.61	30.29	17.00	28.57
E_{beam} (J)	498.30	843.99	476.29	894.41	536.51	937.68
η_{power} (%)	4.83	2.46	2.88	3.84	2.53	2.66
η_{energy} (%)	6.21	3.48	4.17	5.11	3.62	3.82

The peak frequencies used in the tables are the frequencies with the highest peak in the FFT of the rf radial electric field waveform discussed in section 4.2. Three of the geometries tested had frequency spectra with many peaks of comparable size and were labeled "Large" in the tables. The peak frequency for these large spectra was the

frequency with the largest value and it should be noted that the given peak frequency is not necessarily an accurate picture of the operating frequency.

Table 5.7: Best Cases for the Narrow Strip Geometry

	Test 1 Low Voltage	Test 1 High Voltage	Test 2 Low Voltage	Test 2 High Voltage	Test 3 High Voltage
V_{peak} (kV)	424.16	526.43	455.20	602.50	765.90
I_{peak} (kA)	44.22	55.74	38.12	48.93	39.56
Z_{diode} (Ω)	9.59	9.44	11.94	12.31	19.36
f_{peak} (GHz)	1.9	1.70	1.64	1.695	1.65
BW (GHz)	0.35	0.4	0.25	0.22	0.125
P_{MW} (MW)	306.09	226.38	609.76	807.78	1095.25
E_{MW} (J)	15.58	12.14	21.38	32.67	40.30
P_{beam} (GW)	18.63	29.17	16.56	29.05	28.99
E_{beam} (J)	456.36	643.27	439.37	784.18	1036.41
η_{power} (%)	1.64	0.78	3.68	2.78	3.78
η_{energy} (%)	3.42	1.89	4.87	4.17	3.89

Table 5.7: (continued)

	Test 4 Low Voltage	Test 4 High Voltage	Test 5 Low Voltage	Test 5 High Voltage	Test 6 Low Voltage	Test 6 High Voltage
V_{peak} (kV)	497.60	655.20	498.80	634.50	563.30	726.50
I_{peak} (kA)	33.64	46.82	33.73	44.92	32.04	43.00
Z_{diode} (Ω)	14.79	13.99	14.79	14.13	17.58	16.90
f_{peak} (GHz)	2.44	2.43	1.59	1.68	1.48	1.70
BW (GHz)	Large	Large	Large	0.15	0.245	0.41
P_{MW} (MW)	1015.98	989.38	535.58	1149.77	441.60	822.36
E_{MW} (J)	33.76	42.61	19.47	45.07	20.75	37.65
P_{beam} (GW)	15.62	29.29	15.87	27.33	17.08	30.04
E_{beam} (J)	426.63	856.29	451.18	805.17	535.90	962.71
η_{power} (%)	6.50	3.38	3.37	4.21	2.58	2.74
η_{energy} (%)	7.91	4.98	4.32	5.60	3.87	3.91

Figures 5.4 to 5.6 contain the diode voltage and diode current for the best case for each of the geometries. Figures 5.7 to 5.9 contain the beam power and microwave power

waveforms that correspond to the waveforms in Figures 5.4 to 5.6. The start of one waveform may occur at a slightly different time than the waveform of another geometry. The cause for this is the variation in the current. Since the timing mark is triggered by the current waveform and the timing mark is constructed with flip-flops that trigger at a given level, the timing mark generator may occur later in geometries with lower current. This is because the current level needed to trigger the timing mark generator occurs later for lower current geometries than for geometries with higher currents. The current level was so low in one geometry, that it never reached a large enough value to trigger the timing mark generator. But the timing mark generator places a temporal mark at the same time in all of the waveforms for a given shot, thus what is important is the relative occurance of waveforms of a single shot.

As seen in the figures, the diode voltage and current waveforms are all very similar. The main pulse width is approximately 50 ns. As can be seen in the diode voltage waveform, there is a large signal starting around 38 ns which stays on for about 25 ns, then a lower level pulse of 25 ns due to reflections from the load, followed by an exponential decay. The only difference in the voltage waveforms is that the voltage becomes negative in some of the geometries. The voltage is not really negative and the cause for this is that the measured voltage is given by the relation of Eq (4.3) and in certain geometries where the current is large, the inductance term becomes significant. So when the current becomes negative due to reflections, the inductance term has a negative value large enough to dominate the diode voltage and the measured voltage appears negative. This is seen in the voltage waveforms where the geometries with wider emitting surfaces have a larger current and show negative voltages.

In the beam and microwave power waveforms it can be seen that microwaves are starting to be produced about 10 to 15 ns after the beam waveform in all of the tests, due to propagation delay down the waveguide, but the peak of the produced microwaves occurs at different times. It is believed that this is caused by subtle changes in either the geometry or operating parameters, specifically the applied potential. This effect can be seen in the simulations, making small changes in the geometry creates drastic changes in the operation of the device.

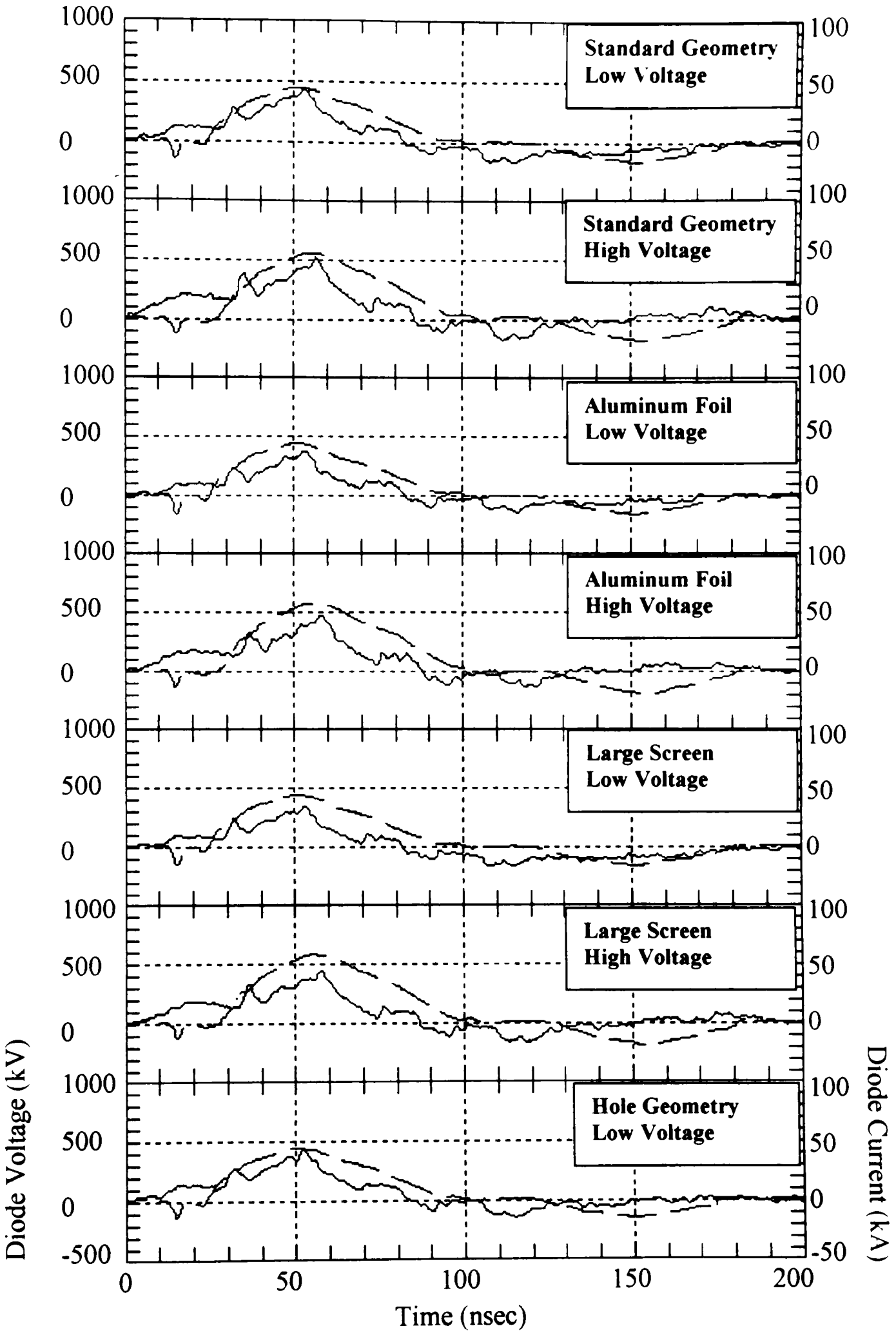

Figure 5.4: Diode Voltage (solid line) and Diode Current (dashed line) for the Best Case of the Tested Coaxial Vircator Geometries.

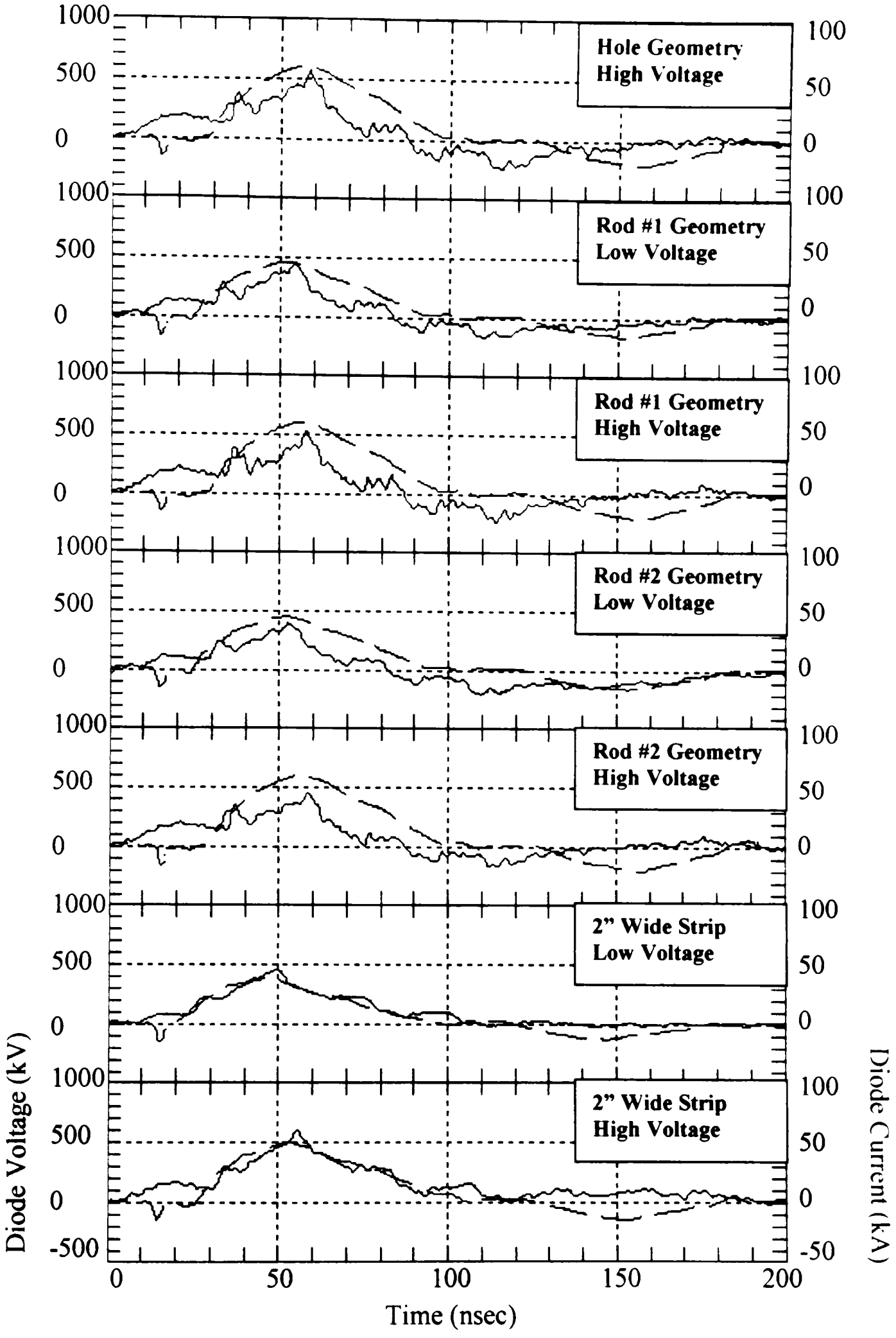

Figure 5.4: (continued).

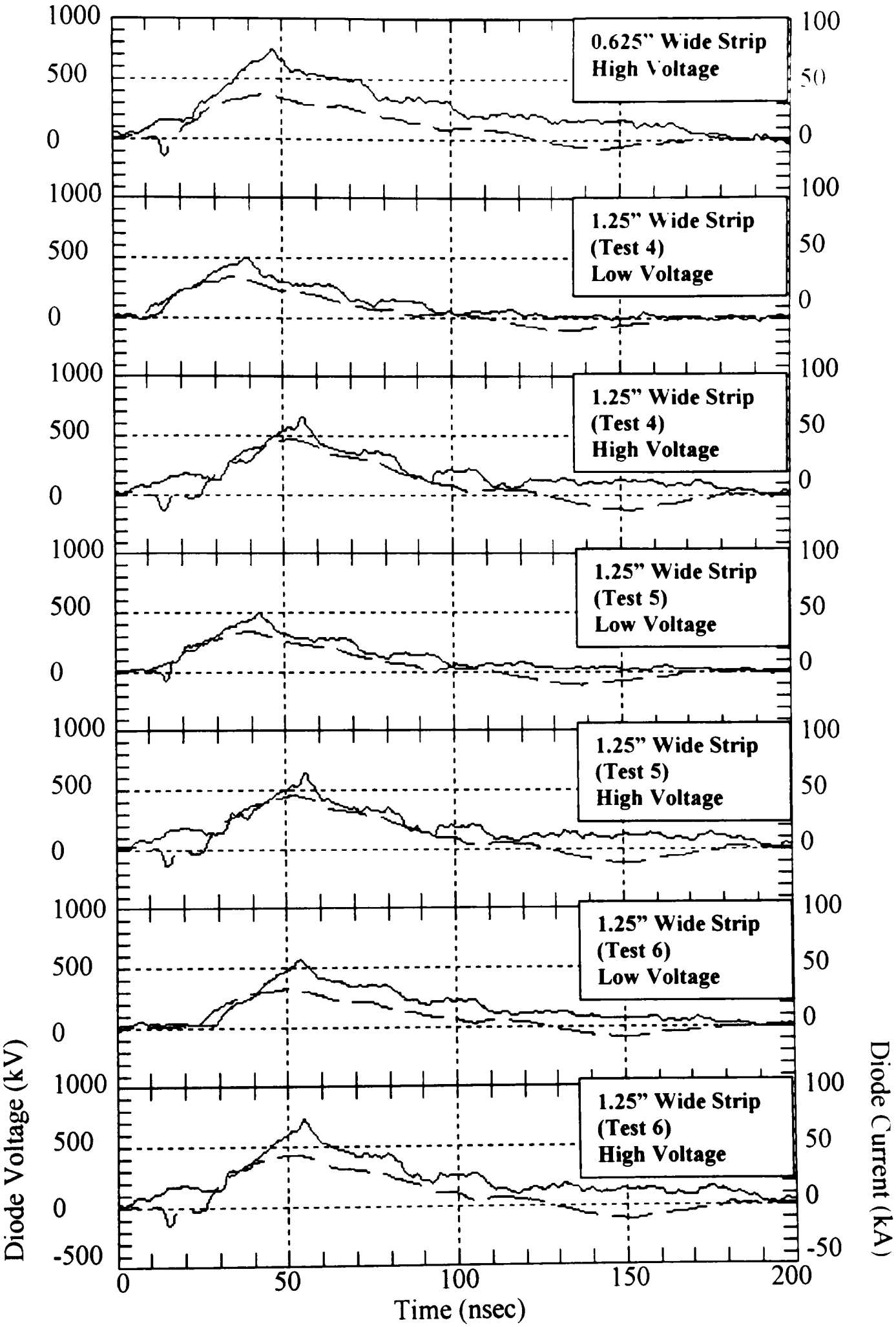

Figure 5.4: (continued).

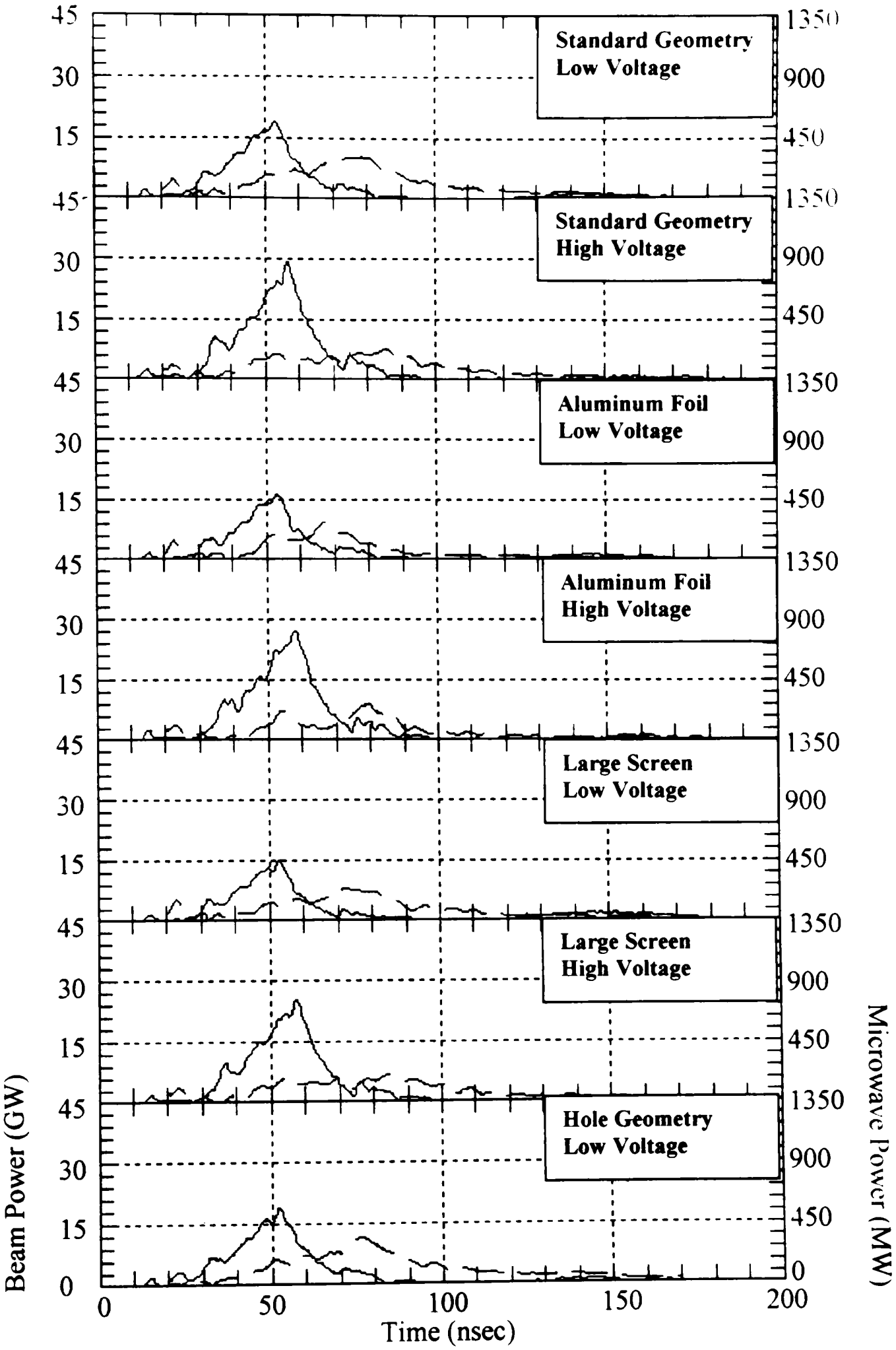

Figure 5.5: Electron Beam Power (solid line) and Microwave Power (dashed line) for the Best Case of the Tested Coaxial Vircator Geometries.

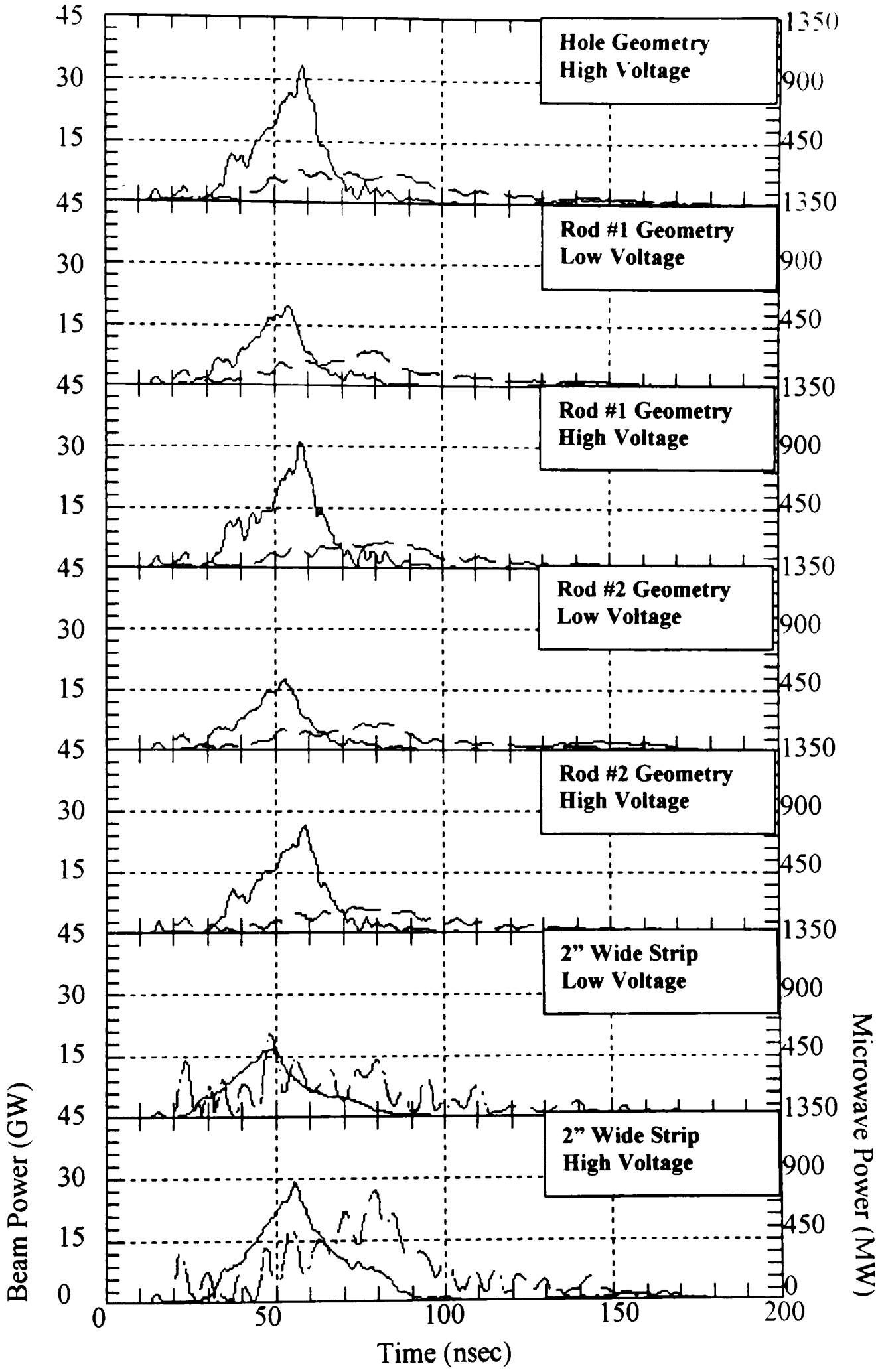

Figure 5.5: (continued).

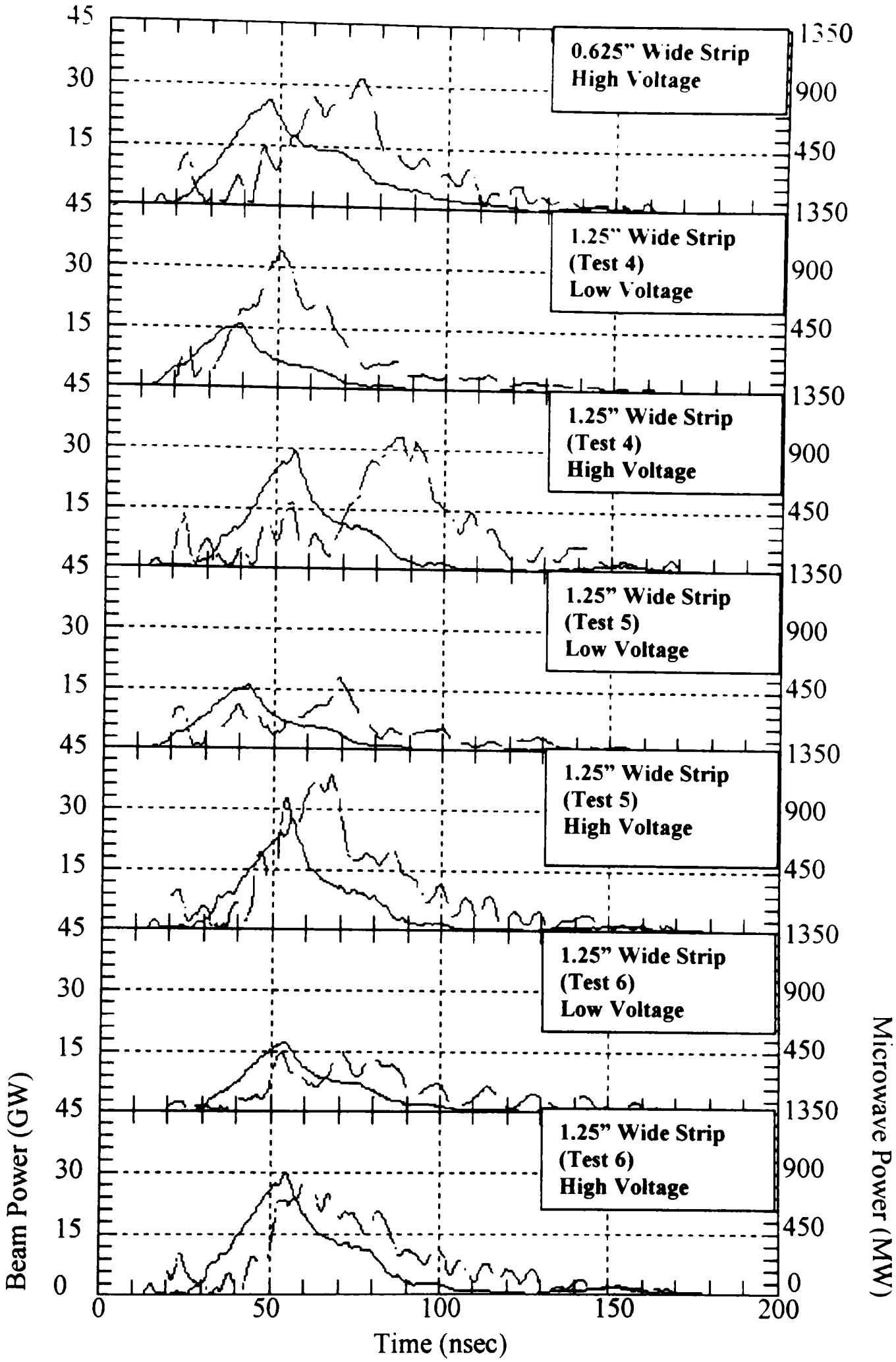

Figure 5.5: (continued).

The exact effect of each little change is also difficult to characterize without extensive experimentation, but one interesting result from the experiments is the increased efficiency with narrow emitting surfaces. The cause of increased output for narrow emitting surfaces is uncertain and would also require extensive experimentation to determine the cause. A possible explanation for a higher output to be produced with narrow emitters can be obtained from simulation. With the aid of MAGIC simulations, it can be seen that as the current increases, a pinching of the electrons occurs. Beam pinching in a coaxial vircator has been seen before [19]. The beam pinching creates a non-uniform beam that will have large phase variations which decreases the output. A result is that as the current increases, the pinching increases, reducing the output power. Due to beam pinching, higher output would be created at higher potentials where the current decreases due to an increase in diode impedance. Figures 5.6 and 5.7 show particle position plots from MAGIC of simulations of the high voltage Test 1 and Test 5 at 15 ns, respectively.

The pinching is easily seen and is caused by the self-magnetic field of the accelerating charges. It is also seen that the beam in Figure 5.6 pinches much more significantly than the beam in Figure 5.7. The larger the pinching, the larger the phase variations that decrease the output power. In the figures, a "smearing" of the virtual cathode is seen. This is caused by the positive ions in these regions. Since macroparticles can represent a variable number of particles, it is believed the smeared macroparticles do not represent a large number of particles since a self-magnetic field large enough to cause the degree of pinching seen would keep most electrons in this region.

MAGIC simulations are the main method of determining the results of a given geometry of the coaxial vircator. The simulations were presented in Chapter 3. The diode impedance, operating frequency, and the efficiency from the simulation are compared to the corresponding experiment. These results are shown in Figures 5.8, 5.9 and 5.10. For the simulations and experiments being compared, the tests described in Table 5.8 correspond to the tests in Figures 5.8 to 5.10 (labeled A through L).

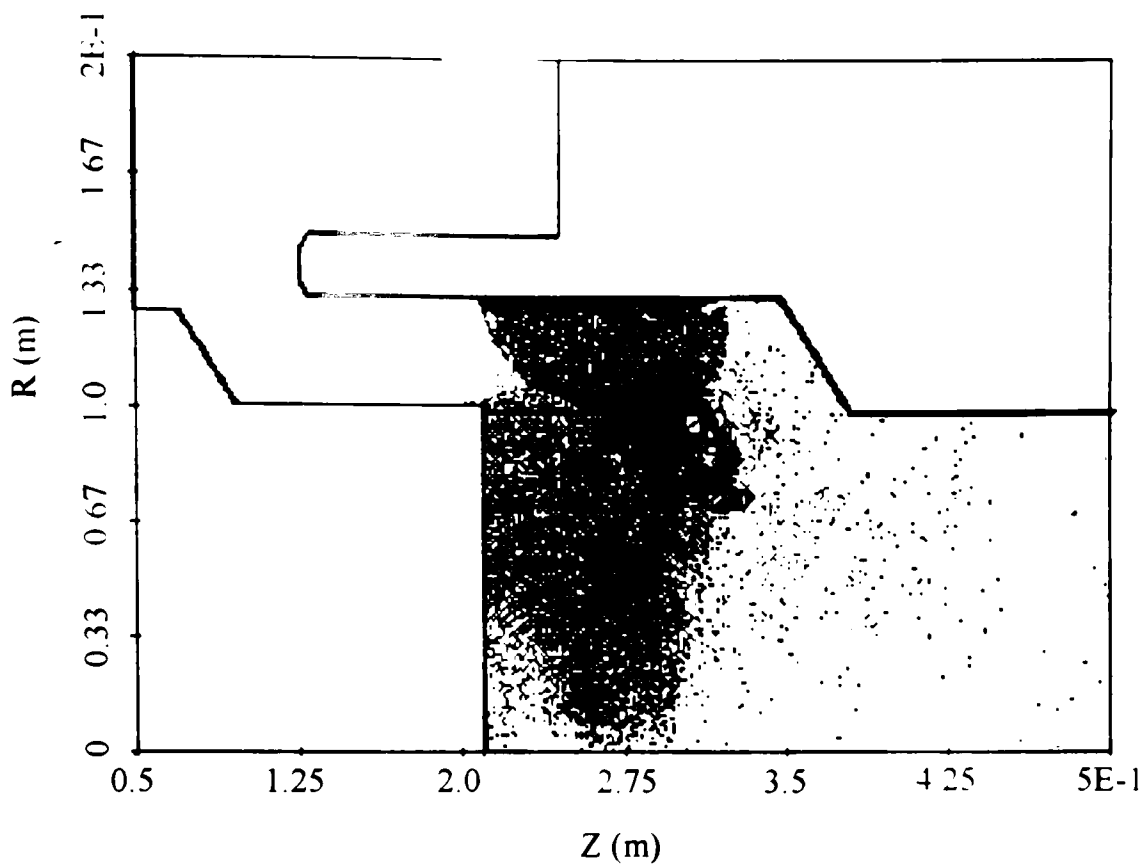

Figure 5.6: Test 1 Particle Position Plot at 15 ns

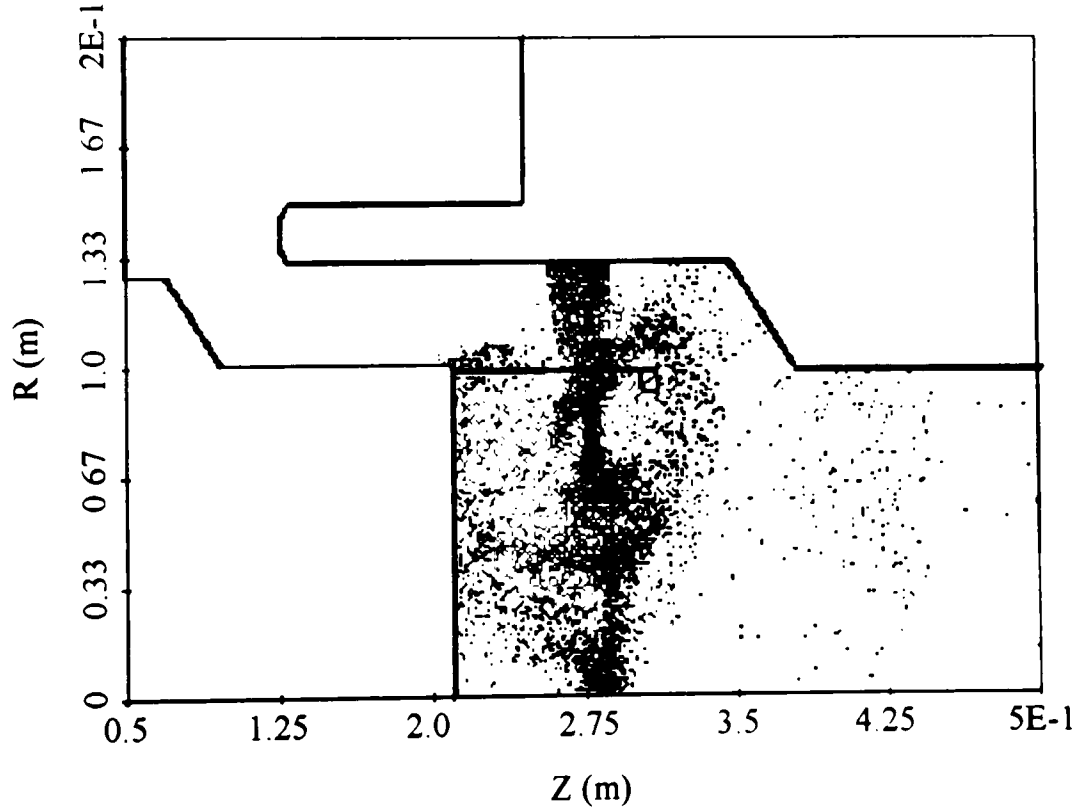

Figure 5.7: Test 5 Particle Position at 15 ns

Table 5.8: Comparisons of Simulations and Experiments

Test Label	Description
A	Standard Geometry High Charging Voltage
B	Standard Geometry Low Charging Voltage
C	Geometry with Aluminum Foil High Charging Voltage
D	Geometry with Aluminum Foil Low Charging Voltage
E	Geometry with Small Collection Rod High Charging Voltage
F	Geometry with Small Collection Rod Low Charging Voltage
G	Geometry with Large Collection Rod High Charging Voltage
H	Geometry with Large Collection Rod Low Charging Voltage
I	Geometry with a Hole High Charging Voltage
J	Geometry with a Hole Low Charging Voltage
K	Geometry with 1.25" Strip High Charging Voltage
L	Geometry with 1.25" Strip Low Charging Voltage

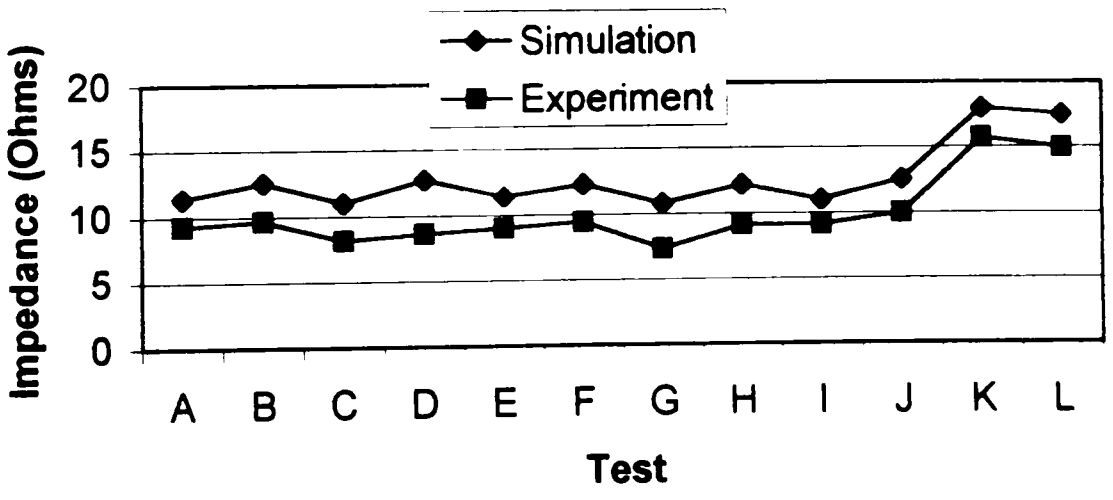

Figure 5.8: Comparison of Simulation and Experimental Impedance

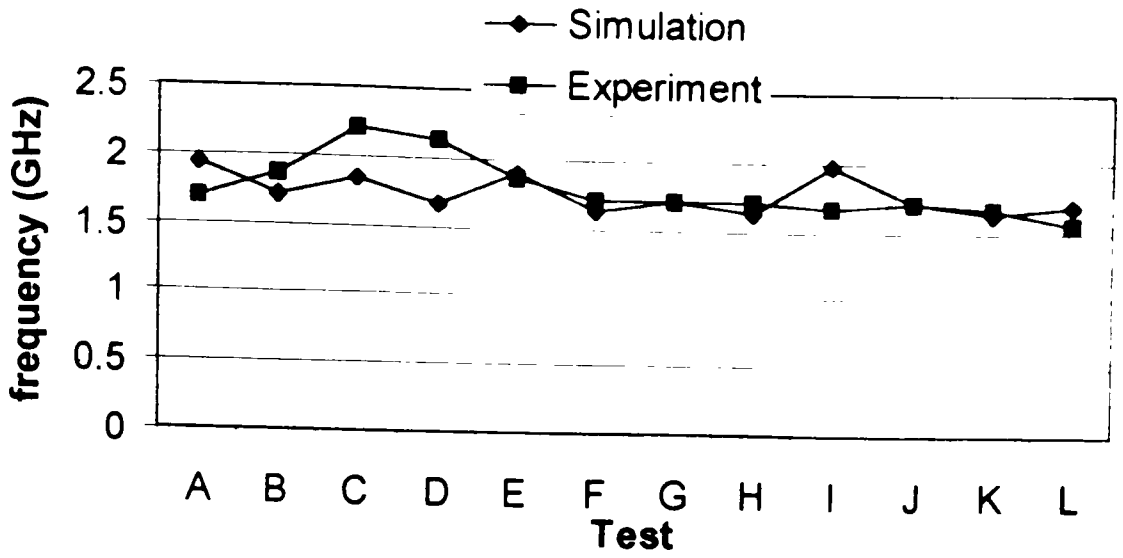

Figure 5.9: Comparison of Simulation and Experimental Frequency

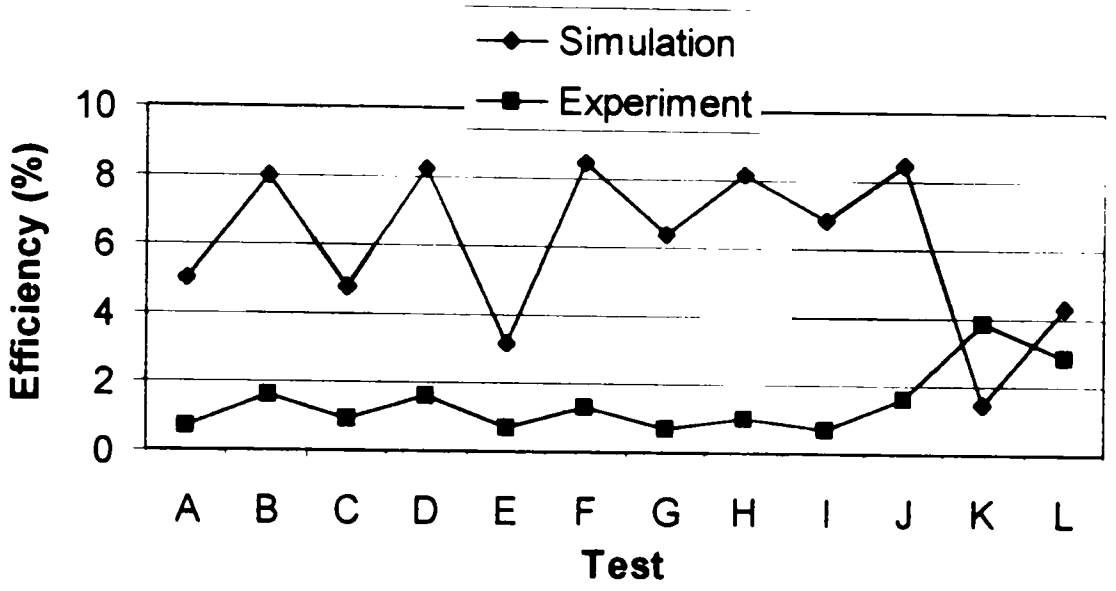

Figure 5.10: Comparison of Simulation and Experimental Efficiency

In the figures of the comparisons of simulation to experiment, the impedance and frequency comparisons are in very good agreement. But the comparison of efficiencies is not very close. Even though the efficiencies from case to case, excluding the last two, show an increased power efficiency for the lower voltage case, the compared values are not close. Also, simulations of the last two cases show that a narrow strip would cause a significant decrease in output power, the opposite of the experimental results. The conclusion from this simulation would be not to even try this geometry that yielded the best results. This leads to the belief that something in the experiment is not being simulated for the calculation of output power but determination of the other parameters are being simulated correctly. Thus, the simulation should be used for the general

operation of the vircator but numerical results for the output power may not be very accurate.

An interesting feature of the coaxial vircator is that the energy efficiency is larger than the power efficiency. The cause for this can be seen in the waveforms of beam power versus microwave power (Figure 5.5). As the beam power dies off, the output power stays at a high level. The cause for this is probably that even though the beam power is low, there is still an applied voltage across the diode. Though the voltage is low, a cloud of electrons has already been created and can still supply electrons to the beam. This supply of electrons and the inward motion allows the electrons to bunch without a large potential, as is needed for the planar geometry, thus producing microwaves and a higher energy efficiency. Also, the power efficiency is calculated at peak microwave power which is not necessarily the best efficiency case for the beam power pulse in this experiment. A flat (rectangular) power pulse would obviously be more desirable.

Another method of computing the efficiencies was to consider only the microwaves produced during the main pulse, believing the exponential decay did not represent true power but reflections caused by mismatches in the system. Calculations with only the main pulse taken into account were performed and had the change in efficiency was negligible compared to the previous efficiency calculations. The energy efficiency still remained larger than the power efficiency.

5.2 Negative Polarity Geometry

The final geometry tested has been termed the negative polarity geometry. The typical polarity arrangement for the vircator at Texas Tech is with the cathode grounded (machine ground) with a positive potential applied to the anode. The negative polarity geometry, shown in Figure 5.11, is pulsed with the anode grounded and a negative potential applied to the cathode. The impetus for this geometry came from the initial testing of the vircator. During the investigation, experimental and simulation, the need for a loss mechanism for electrons was shown to exist for the creation of high output power. If no electrons are dissipated, electrons become permanently trapped in the

virtual cathode, all of the incoming electrons will be reflected and the virtual cathode will never drop below the space charge limit and no oscillations will occur [10]. This may also be a factor in why narrow strips produce higher output powers. With smaller strips, fewer electrons are caught between the ends of the virtual cathode and it is the electrons at the ends that are lost or collected in the vircator structure. The negative polarity case was also suggested to us by Prof. A. G. Zherlitsyn of Tomsk Polytechnic University [20].

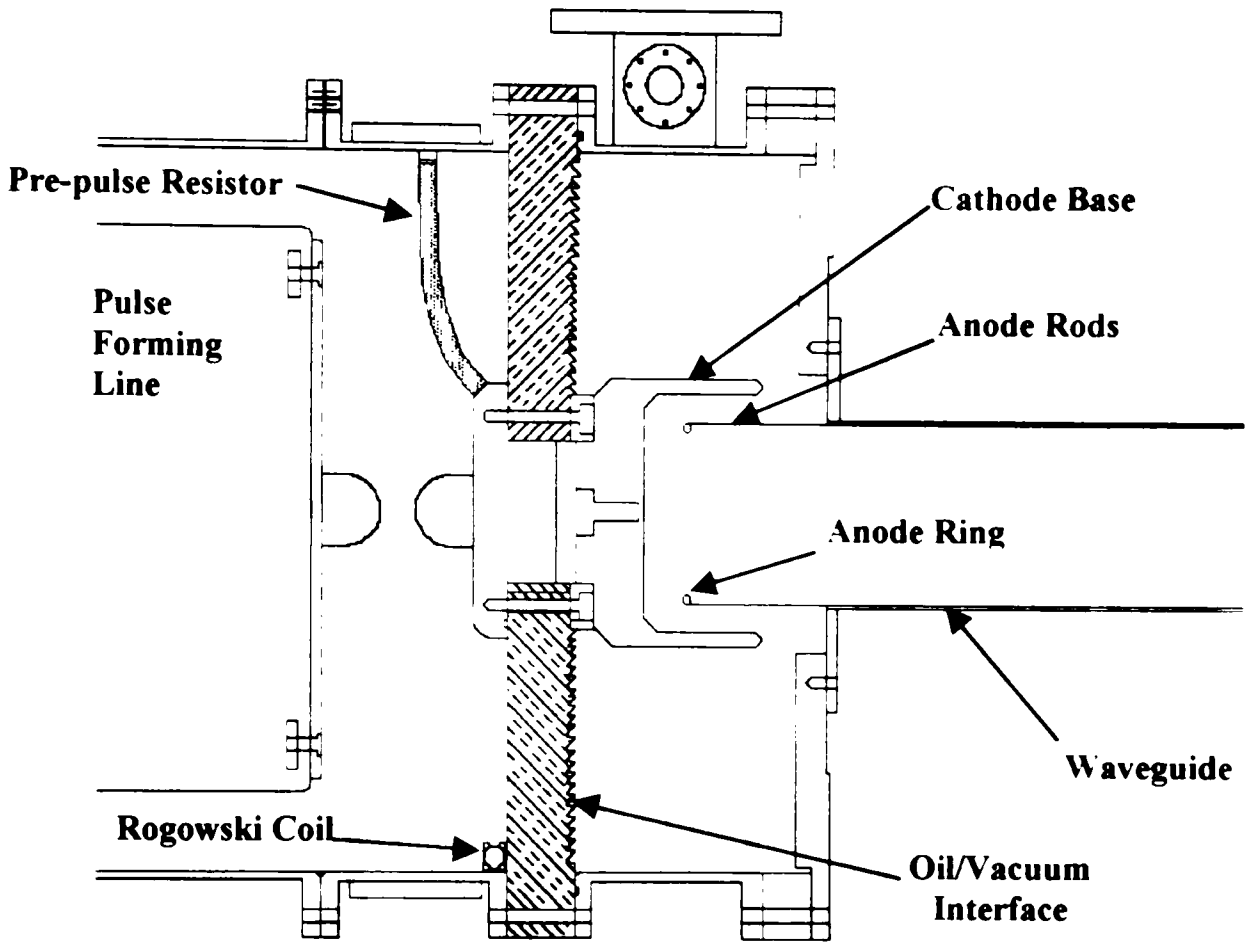

Figure 5.11: Negative Polarity Geometry

The negative polarity geometry provides a mechanism for electrons to be dissipated. The fields are such that, electrons are pushed away from the virtual cathode and into the waveguide. This repulsion of electrons probably only affects the lower energy electrons, which is a further benefit since the less energetic electrons have probably given up their energy to the microwave field. This is an improvement to the positive polarity geometry where the positive polarity on the anode base keeps all electrons in the virtual cathode region.

The coupling of power out of the vircator is also important. Due to the proximity of the virtual cathode to the output waveguide in the negative polarity geometry, more power will be coupled out whereas in the positive polarity geometry, the distance of the virtual cathode from the output waveguide is much larger and discontinuous. A close-up view of the negative polarity geometry is shown in Figure 5.12.

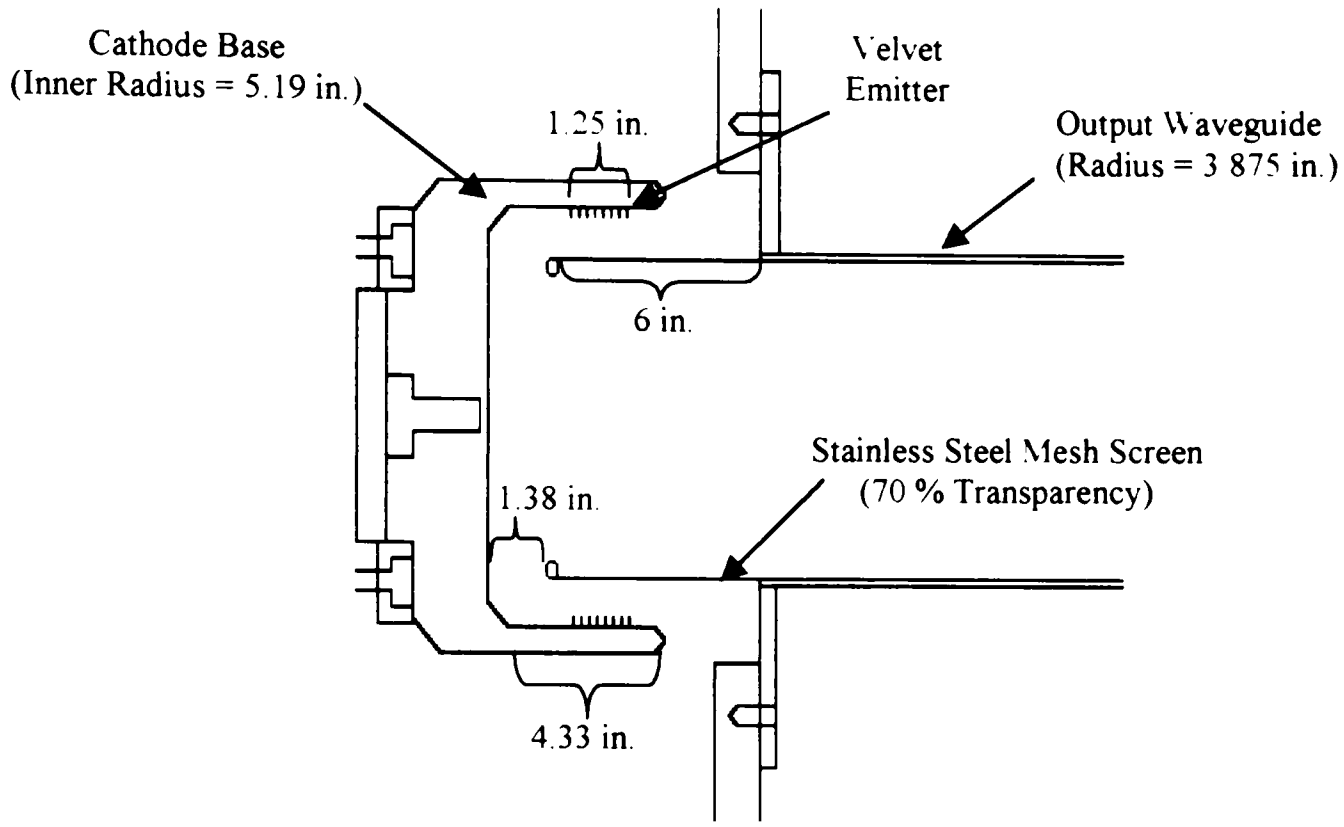

Figure 5.12: Diode Region of the Negative Polarity Geometry

The results from the negative polarity geometry, at two voltage levels, are shown in Table 5.9. The values given are the averages from three separate shots. Table 5.10 contains the best cases for the two voltage levels. Figure 5.13 shows the voltage and current waveforms for the best high and low voltage level shot and Figure 5.14 shows the corresponding beam and output power waveforms. It is easily seen that the high voltage, negative polarity geometry has given the best results of any reported here with an output power approximately 2.852 GW with a power efficiency of 11.57 %. The parameters in Tables 5.9 and 5.10 are the same as those for the positive polarity geometry tables. Calculations are also identical to those in section 5.1.

Table 5.9: Coaxial Vircator Experimental Results with Negative Polarity (avg. of 3 shots)

Test	Negative Polarity Low Voltage	Negative Polarity High Voltage
V_{peak} (kV)	525.80	621.05
I_{peak} (kA)	33.08	41.51
Z_{diode} (Ω)	15.89	14.96
f_{peak} (GHz)	1.95	2.03
BW (GHz)	0.37	0.225
P_{mw} (MW)	1164.67	2755.50
E_{mw} (J)	53.71	89.24
P_{beam} (GW)	16.58	24.63
E_{beam} (J)	442.42	683.44
η_{power} (%)	7.02	11.19
η_{energy} (%)	12.41	13.06

Table 5.10: Coaxial Vircator Experimental Results with Negative Polarity, Best Case

Test	Negative Polarity Low Voltage	Negative Polarity High Voltage
V_{peak} (kV)	518.10	625.20
I_{peak} (kA)	33.22	41.40
Z_{diode} (Ω)	15.60	15.10
f_{peak} (GHz)	1.95	2.04
BW (GHz)	0.37	0.225
P_{mw} (MW)	1236	2852
E_{mw} (J)	55.91	87.62
P_{beam} (GW)	16.35	24.64
E_{beam} (J)	413.67	677.31
η_{power} (%)	7.56	11.57
η_{energy} (%)	13.52	12.94

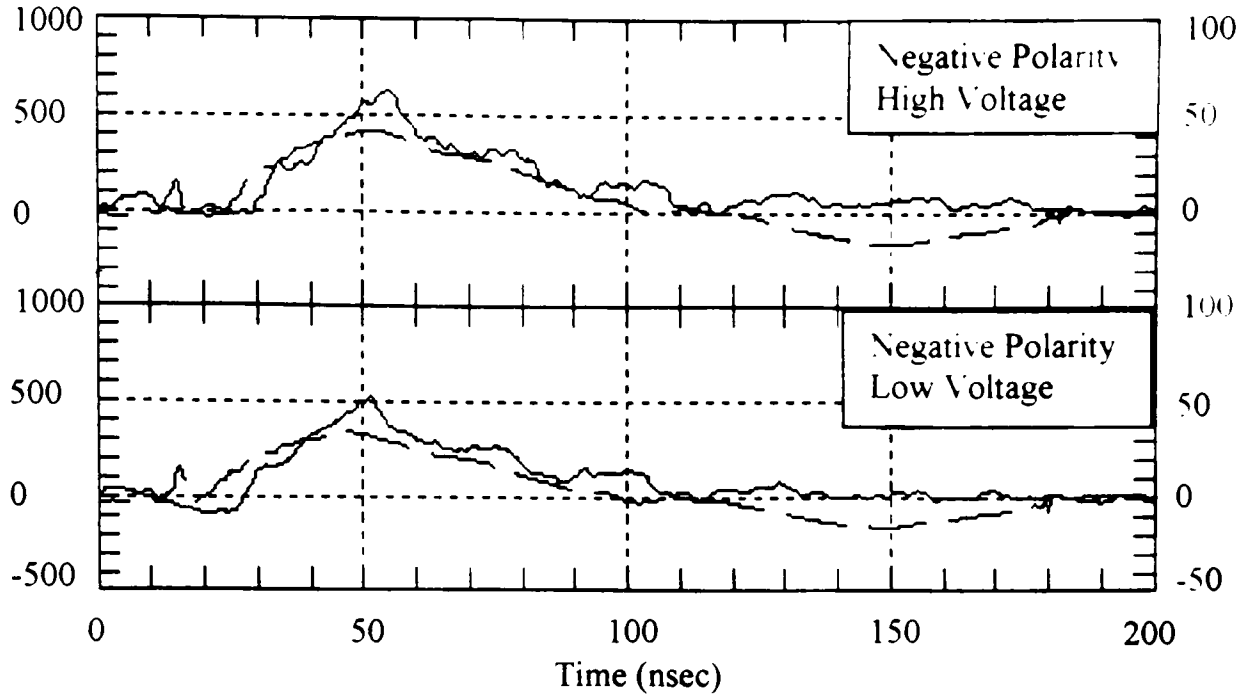

Figure 5.13: Diode Voltage (solid line) and Diode Current (dashed line) for the Best Case of the Negative Geometry Coaxial Vircator

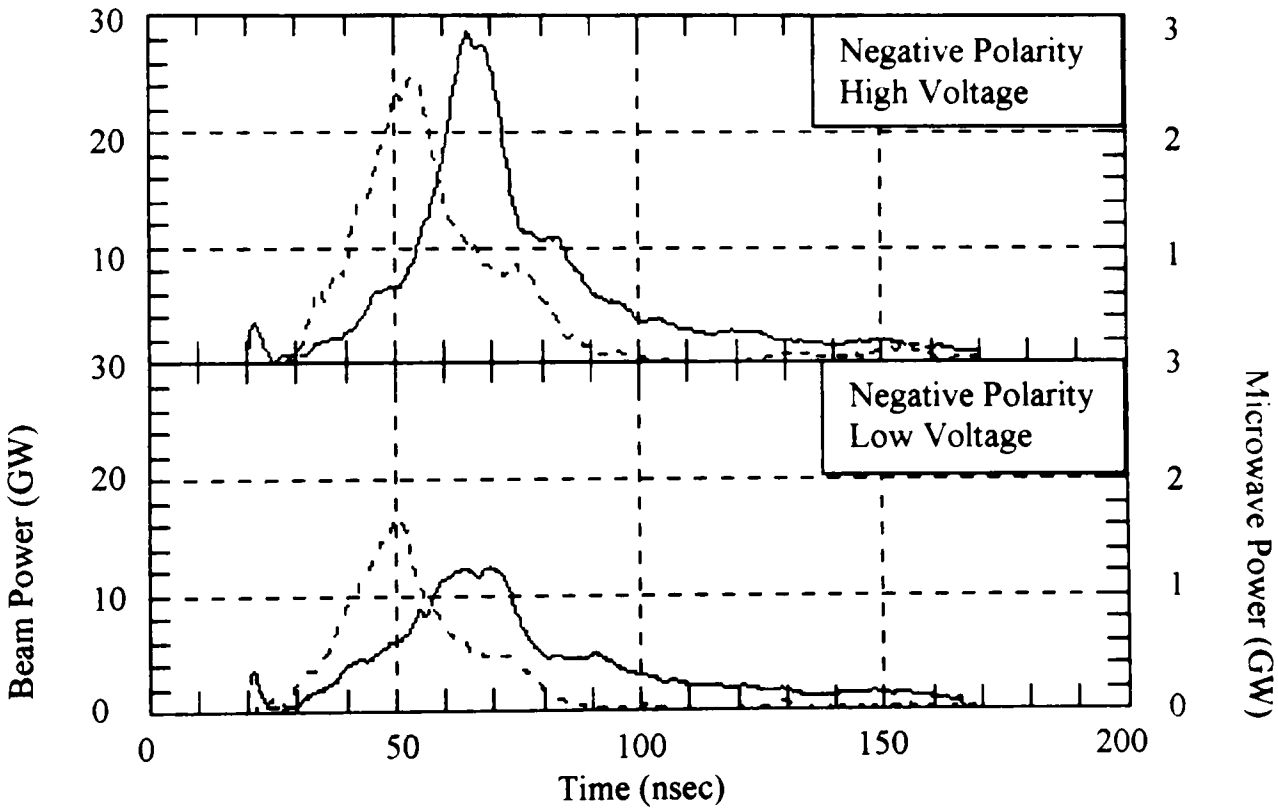

Figure 5.14: Electron Beam Power (dashed line) and Microwave Power (solid line) for the Best Case of the Negative Geometry Coaxial Vircator

With such a large increase in measured power it was believed that window breakdown must be occurring. To verify window breakdown, a camera was placed inside the anechoic chamber with the shutter open while the vircator was fired. Any breakdown

would be captured on film as light. The film showed light and gave proof that the window was breaking down. The effect and timing of breakdown at the waveguide output, with respect to the measured signal in the waveguide, needed to be determined since window breakdown would cause the microwaves to be reflected back into the waveguide, and depending upon the standing wave created from the reflections, can give false readings. To determine the effect of the reflections from breakdown, a plastic bag with SF_6 enclosed was placed over the end of the waveguide to inhibit breakdown. Then the vircator was fired. The resulting waveform was captured and a camera was used to take a picture of the waveguide output to see if any breakdown occurred. The picture showed no light which indicating no breakdown. The waveform obtained was identical to shots without bagged SF_6. This indicated that the waveforms obtained are not being affected by breakdown.

To understand why breakdown did not significantly alter the measured waveform, the timing of the breakdown needed to be determined. This was accomplished with the aid of a fiber optic cable placed at the output of the waveguide. Then taking the propagation delay of the microwave signal from the measuring probes to the fiber optic cable into account, the time of breakdown with respect to the measured signal could be determined. The test showed that breakdown did not occur until after the main pulse had already passed. This supports the previous results that breakdown was not causing significant changes to the waveform.

CHAPTER 6
CONCLUSIONS AND SUGGESTIONS

The MAGIC computer code has been used to formulate numerical results of subtle changes made in the standard geometry. The standard geometry is the previously designed coaxial vircator at Texas Tech University as discussed in Ref [10]. These simulations were performed to create a set of experiments to be performed that would increase the output power, power efficiency and energy efficiency of the standard vircator geometry. One of the observations from the simulations is that minor changes in the geometry can have large effects in the operation of the vircator. It was also shown that the simulations are good at generating certain parameters, such as frequency and impedance, but poor at generating the output power and this is the main parameter used to determine if a simulated geometry will be tested. On the other hand, the simulations are good at general characterizations. The existence of bipolar current flow is an example.

Increasing the output power, which will result in an increased efficiency, is the main focus of the tests performed. It was shown that by decreasing the applied voltage, the reflexing and plasma frequencies could be matched, causing an increase in output power and increased efficiency. But from the various experiments performed, the best results were obtained from narrow emitting surfaces. The cause for this is currently not well understood but a possible explanation has been presented. Also, in Chapter 2 the wrong-phased electrons and their effect on the output power were discussed. Some of the geometries tested were aimed at reducing the effect of these wrong phased electrons, these include the hole and rod geometries.

Each of these tested cases used only one of the methods of increasing the output power and efficiency. A further increase in efficiency could be obtained if a geometry were designed that used a narrow velvet strip but the gap distance changed such that the applied voltage would cause the plasma and reflexing frequencies to coincide. But this is not very easy. By decreasing the width of the strip, the electron density decreases and the applied potential increases. This causes the plasma frequency to decrease and the

reflexing frequency to increase according to Equations (2.6) and (2.4), respectively.

The best way to increase the efficiency and output of the vircator is to match the system parameters previously discussed. The procedure would be a simultaneous combination of using a narrow strip, adjusting the applied potential such that the plasma and reflexing frequencies match for a given gap distance and avoid beam pinching. Also, the length of the anode foil should be chosen such that the resonant frequency created by the screen, as discussed in Chapter 2, matches the plasma and reflexing frequencies. In this situation, a high output and high efficiency should be obtained. This is a very promising avenue to pursue in future work on the coaxial vircator.

A TE_{11} mode is produced and the cause for this mode was discussed in Chapter 2. The frequency generated has also been discussed in Chapter 2. Much of the results are geometry specific, meaning that small changes in the geometry create large changes in the operation of the vircator. An example of this is the frequency produced by the 1.25" strip at various locations. Two of the positions produced a frequency at approximately the resonant frequency of the cavity while the third position produced a wide band of frequencies. To be able to exactly determine what is happening would require extensive experimentation and this could also be future work on the vircator.

The experimentation on the coaxial vircator at Texas Tech has shown it capable of producing high output powers. The negative polarity geometry performed the best of all the geometries tested with energy efficiencies of over 13% and power efficiencies over 11.5% at output powers approaching 3 GW. It should be noted that due to impedance mismatch at the output window, the created standing wave could lead to measurement errors. Also, during the experiments it was assumed that only one mode occurred at the main frequency, the TE_{11} mode. However, if another mode simultaneously exists at the same frequency, specifically a TE_{11} and TM_{01}, the field pattern across a plane in the waveguide would be significantly different than the field pattern of only a TE_{11} mode. Since the microwave power is based upon the field pattern, calculations based upon an incorrect field pattern could lead to significant errors. Determining how many modes exist at a given frequency is very important for accurate power calculations and experiments are currently being performed. Also, free-field B-dot

probe measurement experiments are being conducted to verify the previously produced results.

In view of the results, continued research on the coaxial vircator is highly recommended. Also, since the tests performed on the system did not have a matched load, further testing with a matched horn antenna would be desirable for more accurate data. Another avenue of research would be on a virtode geometry, which would require a longer pulse-forming line to allow the microwave signal time to propagate back into the acceleration region and could provide even better results.

REFERENCES

1. J. Benford and L. Swegle, *High-Power Microwaves*, Boston: Artech House, Inc. 1992.

2. N. P. Gadetskii, I. I. Magda, L. I. Naisteter, Yu. V. Prokopenko and V. I. Chumakov, "The virtode: a generator using supercritical REB current with controlled feedback," *Plasma Physics Rep.*, Vol. 19, No. 4, 1993

3. R. H. Fowler and L. W. Nordheim, *Proc. Roy. Soc. Lodon*, A119, 1928.

4. S. T. Pai and Q. Zhang, *Introduction to High Power Pulse Technology*, Singapore: World Scientific Publishing Co. Pte. Ltd., 1995.

5. F. Rohrbach, *CERN Report*, 71-5/TC-L, 1971.

6. I. Langmuir and K. Blodgett, "Currents Limited by Space Charge Between Coaxial Cylinders," *Phys. Rev.*, Vol. 22, 1925.

7. C. S. Hwang, M. W. Wu, P. S. Song, and W. S. Hou, "High Power Microwave Generation from a Tunable Radially Extracted Vircator," *J. Appl. Phys.*, Vol. 69, No. 3, 1991.

8. A. Kadish, R. Gaehl and C. Snell, "Analysis and Simulation of Virtual Cathode Oscillations," *Phys. Fluids*, Vol. 29, No. 12, 1986.

9. A. N. Didenko, A. G. Zherlitsyn, A. S. Sulakshin, G. P. Fomenko, V. I. Tsvetkov, and Yu. G. Shtein, "Electron beam in a triode system," *Sov. Tech. Phys. Lett.*, Vol. 9, No. 12, 1983.

10. M. Crawford, "A Coaxial Virtual Cathode Oscillator High-Powered Microwave Source", Ph.D. Dissertation, Texas Tech University, 1994.

11. John D. Jackson, *Classical Electrodynamics*, 2nd Ed., John Wiley and Sons, New York, 1975.

12. B. Augsburger, "The Design of a High Power Electron Beam Generator", Master's Thesis, Texas Tech University, 1989.

13. H. A. Davis, R. R. Bartsch, J. T. Kwan, E. G. Sherwood and R. M. Stringfield, "Experimental Confirmation of the Reditron Concept," *IEEE Trans. On Plasma Science*, Vol. 16, No.2, 1988.

14. D. Young, "Effects of Diode Gap Closure and Bipolar Flow on Vircator Microwave Generation", Master's Thesis, Texas Tech University, 1996.

15. M. Yatsuzuka, M. Nakayama, M. Tanigawa, S. Nobuhara, D. Young and O. Ishihara, "Plasma Effects on Electron Beam Focusing and Microwave Emission in a Virtual Cathode Oscillator," Submitted to *IEEE Trans. on Plasma Science, 7th Special Issue on High Power Microwave Generation*, 1998.

16. M. Crawford, "Electrical Diagnostics on a High-Power Microwave Generator", Master's Thesis, Texas Tech University, 1991.

17. S. Burkhart, "Coaxial E-field Probe for High-Power Microwave Measurements," *IEEE Transactions on Microwave Theory and Techniques*, Vol MIT-33, No. 3, March, 1985.

18. Jay Chase and Roger Minich, Personal Communication.

19. L. Guozhi, Q. Shi, W. Hongjun, H. Wenhua, and W. Feng, "Study on Coaxial Diode and Vircator", SPIE Proceedings, Vol. 3158, San Diego, 1997.

20. A. G. Zherlitsyn, Personal Communication.

APPENDIX

INPUT COMMAND DECKS FOR MAGIC SIMULATIONS
ALL INPUT DECKS RUN IN MAGIC40

Initial Simulation Input Deck from Section 3.1

```
TITLE "COAXIAL VIRCATOR MODEL WITH LONG ANODE;
SYSTEM CYLINDER-THETA;
X1GRID FUNCTION 226 2 0 8 10.0E-3 50.0E-3
                152 2.22E-3 337.44E-3
                10 2.22E-3 58.0E-3
                54 10E-3 540.0E-3;
X2GRID FUNCTION 98 2 0 10 4E-3 31.825E-3
          56 2.22E-3 124.32E-3
          30 2.22E-3 233.9E-3;
SYMMETRY AXIAL ALIGN 2 2 226 2;
DIAGNOSE COURANT 1 0 0;
FIELDS ALL HI-Q 3000 5.0E-12;
CONDUCTOR OUTER1 ANTI-ALIGN 2 98
                98 98
                98 65
                46 65
                44 63
                44 59
                46 57
                81 57;
CONDUCTOR EMSURF ANTI-ALIGN 81 57
                133 57;
CONDUCTOR OUTER2 ANTI-ALIGN 133 57
                144 57
                159 42
                226 42;
CONDUCTOR INNER1 ALIGN 2 93
                10 93
                10 55
                19 55
                31 43
                82 43
                82 2;
CONDUCTOR INNER2 ALIGN 124 42
                127 42
                128 41
                128 39
```

```
                125 39
                124 40
                124 42;
MATERIAL SS304 MASS 26 55.847 7.87E3;
FOIL SS304 1E-6 82 42
        124 42;
DISPLAY REAL 0.0 1.0 0.0 0.5;
LOOKBACK FIELDS ALL 1.23 1.0 ANTI-ALIGN 226 2 226 42;
FUNCTION "VOFT(T)=-400E3*TANH(0.5E9*T)";
FUNCTION "RADIAL(X)=1.0/X";
VOLTAGE FIELDS TM VOFT RADIAL 1.0 0.0 1.0 ALIGN 2 93 2 98;
EMISSION ELECTRNS ELECTRON 5 1
        FIELD 1 0.9E7 0.0 0.0 0.0
        SPACING RANDOM 1.0E-5 RANDOM
        GAMMAV 1E6;
EMIT ELECTRNS EMSURF;
FUNCTION "STEP(T,X1,X2)=4.0*MAX(STEP(ABS(OBS1),0.0)-0.75, 0.0)";
KINEMATICS ELECTRON 1 YES NO YES EM 1 1;
KINEMATICS PROTON 1 YES NO YES EM 1 1;
FORCES 0.5 1.0 1.0;
CURRENTS LCC NO NO 0.0 1.0;
TAGGING 0.125;
TIMER FOR_FLUX PERIODIC 0 99999 1;
FLUX ELECRNT FOR_FLUX ELECTRON
        INDICES ANTI-ALIGN 82 42 124 42;
OBSERVE FLUX ELECRNT CURRENT;
FLUX TEST FOR_FLUX ELECTRON
        INDICES ANTI-ALIGN 82 55 124 55;
C DIODE CURRENT MEASUREMENT
OBSERVE FLUX TEST CURRENT;
OBSERVE FIELD E2 2 93 2 98 FFT 5 WINDOW FREQUENCY 0.0 5.0E9;
OBSERVE FIELD B3 5 95 5 95 FFT 5 WINDOW FREQUENCY 0.0 5.0E9;
TIMER STTIME PERIODIC 25 99999 25;
STATISTICS STTIME;
TIMER PHTIME PERIODIC 1000 3000 1000;
C PARTICLE PLOTS
PHASESPACE PHTIME AXES X1 X2
      AXIS X 0.05 0.50 0.05
      AXIS Y 0.0 0.20 0.05
      SPECIES ALL SELECT TAG;
PHASESPACE PHTIME AXES X2 P2
      AXIS X 0.00 0.20 0.05
      AXIS Y -1.0E9 1.0E9 0.25E9
      SPECIES ALL SELECT TAG;
PHASESPACE PHTIME AXES X1 P1
```

```
        AXIS X 0.05 0.50 0.05
        AXIS Y -1.0E9 1.0E9 0.25E9
        SPECIES ALL SELECT TAG;
C DIODE VOLTAGE AND FIELDS
OBSERVE FIELD E1 218 41 218 41 FFT 5 WINDOW FREQUENCY 0.0 5.0E9;
OBSERVE FIELD E2 218 41 218 41 FFT 5 WINDOW FREQUENCY 0.0 5.0E9;
OBSERVE FIELD B3 218 41 218 41 FFT 5 WINDOW FREQUENCY 0.0 5.0E9;
C OUTPUT POWER WAVE
OBSERVE POYNTING ALL ANTI-ALIGN 218 2 218 42;
OBSERVE POYNTING TM ANTI-ALIGN 218 2 218 42;
OBSERVE POYNTING TE ANTI-ALIGN 218 2 218 42;
VECTOR PHTIME FIELD E1 E2
                NUMBER 20 20
                SCALE LINEAR
                AXIS X 0.05 0.5 0.075
                AXIS Y 0.0 0.2 0.0333;
OUTPUT COLOR;
OUTPUT SYSTEM TEST12.PLT GPRINT3;
C OUTPUT THE PARAMETERS TO A FILE
DUMP NAME "TEST12";
DUMP FORMAT ASCII;
DUMP TYPE OBSERVE;
DUMP TYPE PHASESPACE;
START;
STOP;
```

Simulation Input Deck With Bipolar Flow

```
TITLE "COAXIAL VIRCATOR MODEL WITH LONG ANODE AND BIPOLAR
FLOW";
SYSTEM CYLINDER-THETA;
X1GRID FUNCTION 226 2 0 8 10.0E-3 50.0E-3
                152 2.22E-3 337.44E-3
                10 2.22E-3 58.0E-3
                54 10E-3 540.0E-3;
X2GRID FUNCTION 98 2 0 10 4E-3 31.825E-3
          56 2.22E-3 124.32E-3
          30 2.22E-3 233.9E-3;
SYMMETRY AXIAL ALIGN 2 2 226 2;
DIAGNOSE COURANT 1 0 0;
FIELDS ALL HI-Q 3000 5.0E-12;
CONDUCTOR OUTER1 ANTI-ALIGN 2 98
                98 98
                98 65
                46 65
                44 63
                44 59
                46 57
                81 57;
 CONDUCTOR EMSURF ANTI-ALIGN 81 57
                133 57;
CONDUCTOR OUTER2 ANTI-ALIGN 133 57
                144 57
                159 42
                226 42;
CONDUCTOR INNER1 ALIGN 2 93
                10 93
                10 55
                19 55
                31 43
                82 43
                82 2;
CONDUCTOR INNER2 ALIGN 124 42
                127 42
                128 41
                128 39
                125 39
                124 40
                124 42;
MATERIAL SS304 MASS 26 55.847 7.87E3;
FOIL SS304 1E-6 82 42
```

```
                124 42;
DISPLAY REAL 0.0 1.0 0.0 0.5;
LOOKBACK FIELDS ALL 1.23 1.0 ANTI-ALIGN 226 2 226 42;
C CHANGE –400 TO –300 FOR THE LOW VOLTAGE CASE
FUNCTION "VOFT(T)=-400E3*TANH(0.5E9*T)";
FUNCTION "RADIAL(X)=1.0/X";
VOLTAGE FIELDS TM VOFT RADIAL 1.0 0.0 1.0 ALIGN 2 93 2 98;
EMISSION ELECTRNS ELECTRON 5 1
        FIELD 1 0.9E7 0.0 0.0 0.0
        SPACING RANDOM 1.0E-5 RANDOM
        GAMMAV 1E6;
EMIT ELECTRNS EMSURF;
FUNCTION "STEP(T,X1,X2)=4.0*MAX(STEP(ABS(OBS1),0.0)-0.75, 0.0)";
EMISSION ANEMT PROTON 1 2
        FIELD STEP 0.0 0.0 0.0 0.0
        SPACING RANDOM 1.0E-5 RANDOM
        GAMMAV 1E6;
EMIT ANEMT SS304FOIL;
KINEMATICS ELECTRON 1 YES NO YES EM 1 1;
KINEMATICS PROTON 1 YES NO YES EM 1 1;
FORCES 0.5 1.0 1.0;
CURRENTS LCC NO NO 0.0 1.0;
TAGGING 0.125;
TIMER FOR_FLUX PERIODIC 0 99999 1;
FLUX ELECRNT FOR_FLUX ELECTRON
        INDICES ANTI-ALIGN 82 42 124 42;
OBSERVE FLUX ELECRNT CURRENT;
FLUX TEST FOR_FLUX ELECTRON
        INDICES ANTI-ALIGN 82 55 124 55;
C DIODE CURRENT MEASUREMENT
OBSERVE FLUX TEST CURRENT;
OBSERVE FIELD E2 2 93 2 98 FFT 5 WINDOW FREQUENCY 0.0 5.0E9;
OBSERVE FIELD B3 5 95 5 95 FFT 5 WINDOW FREQUENCY 0.0 5.0E9;
TIMER STTIME PERIODIC 25 99999 25;
STATISTICS STTIME;
TIMER PHTIME PERIODIC 1000 6000 1000;
C PARTICLE PLOTS
PHASESPACE PHTIME AXES X1 X2
      AXIS X 0.05 0.50 0.05
      AXIS Y 0.0 0.20 0.05
      SPECIES ALL SELECT TAG;
PHASESPACE PHTIME AXES X2 P2
      AXIS X 0.00 0.20 0.05
      AXIS Y -1.0E9 1.0E9 0.25E9
      SPECIES ALL SELECT TAG;
```

```
PHASESPACE PHTIME AXES X1 P1
        AXIS X 0.05 0.50 0.05
        AXIS Y -1.0E9 1.0E9 0.25E9
        SPECIES ALL SELECT TAG;
C DIODE VOLTAGE AND FIELDS
OBSERVE FIELD E1 218 41 218 41 FFT 5 WINDOW FREQUENCY 0.0 5 0E9;
OBSERVE FIELD E2 218 41 218 41 FFT 5 WINDOW FREQUENCY 0.0 5.0E9;
OBSERVE FIELD B3 218 41 218 41 FFT 5 WINDOW FREQUENCY 0.0 5.0E9;
C OUTPUT POWER WAVE
OBSERVE POYNTING ALL ANTI-ALIGN 218 2 218 42;
OBSERVE POYNTING TM ANTI-ALIGN 218 2 218 42;
OBSERVE POYNTING TE ANTI-ALIGN 218 2 218 42;
VECTOR PHTIME FIELD E1 E2
                NUMBER 20 20
                SCALE LINEAR
                AXIS X 0.05 0.5 0.075
                AXIS Y 0.0 0.2 0.0333;
OUTPUT COLOR;
OUTPUT SYSTEM TEST21.PLT GPRINT3;
DUMP NAME "TEST21";
DUMP FORMAT ASCII;
DUMP TYPE OBSERVE;
DUMP TYPE PHASESPACE;
START;
STOP;
```

Simulation Input Deck With Bipolar Flow and Aluminum Foil

```
TITLE "COAXIAL VIRCATOR MODEL WITH LONG ANODE, BIPOLAR FLOW
AND ALUMINUM FOIL";
SYSTEM CYLINDER-THETA;
X1GRID FUNCTION 226 2 0 8 10.0E-3 50.0E-3
                152 2.22E-3 337.44E-3
                10 2.22E-3 58.0E-3
                54 10E-3 540.0E-3;
X2GRID FUNCTION 98 2 0 10 4E-3 31.825E-3
          56 2.22E-3 124.32E-3
          30 2.22E-3 233.9E-3;
SYMMETRY AXIAL ALIGN 2 2 226 2;
DIAGNOSE COURANT 1 0 0;
FIELDS ALL HI-Q 3000 5.0E-12;
CONDUCTOR OUTER1 ANTI-ALIGN 2 98
                98 98
                98 65
                46 65
                44 63
                44 59
                46 57
                81 57;
CONDUCTOR EMSURF ANTI-ALIGN 81 57
                133 57;
CONDUCTOR OUTER2 ANTI-ALIGN 133 57
                144 57
                159 42
                226 42;
CONDUCTOR INNER1 ALIGN 2 93
                10 93
                10 55
                19 55
                31 43
                82 43
                82 2;
CONDUCTOR INNER2 ALIGN 124 42
                127 42
                128 41
                128 39
                125 39
                124 40
                124 42;
MATERIAL ALUM MASS 13 26.98154 2.7E3;
FOIL ALUM 10E-6 82 42
```

```
                124 42;
DISPLAY REAL 0.0 1.0 0.0 0.5;
LOOKBACK FIELDS ALL 1.23 1.0 ANTI-ALIGN 226 2 226 42;
C CHANGE –400 TO –300 FOR THE LOW VOLTAGE CASE
FUNCTION "VOFT(T)=-400E3*TANH(0.5E9*T)";
FUNCTION "RADIAL(X)=1.0/X";
VOLTAGE FIELDS TM VOFT RADIAL 1.0 0.0 1.0 ALIGN 2 93 2 98;
EMISSION ELECTRNS ELECTRON 5 1
        FIELD 1 0.9E7 0.0 0.0 0.0
        SPACING RANDOM 1.0E-5 RANDOM
        GAMMAV 1E6;
EMIT ELECTRNS EMSURF;
FUNCTION "STEP(T,X1,X2)=4.0*MAX(STEP(ABS(OBS1),0.0)-0.75, 0.0)";
EMISSION ANEMT PROTON 1 2
        FIELD STEP 0.0 0.0 0.0 0.0
        SPACING RANDOM 1.0E-5 RANDOM
        GAMMAV 1E6;
EMIT ANEMT ALUMFOIL;
KINEMATICS ELECTRON 1 YES NO YES EM 1 1;
KINEMATICS PROTON 1 YES NO YES EM 1 1;
FORCES 0.5 1.0 1.0;
CURRENTS LCC NO NO 0.0 1.0;
TAGGING 0.125;
TIMER FOR_FLUX PERIODIC 0 99999 1;
FLUX ELECRNT FOR_FLUX ELECTRON
        INDICES ANTI-ALIGN 82 42 124 42;
OBSERVE FLUX ELECRNT CURRENT;
FLUX TEST FOR_FLUX ELECTRON
        INDICES ANTI-ALIGN 82 55 124 55;
C DIODE CURRENT MEASUREMENT
OBSERVE FLUX TEST CURRENT,
OBSERVE FIELD E2 2 93 2 98 FFT 5 WINDOW FREQUENCY 0.0 5.0E9;
OBSERVE FIELD B3 5 95 5 95 FFT 5 WINDOW FREQUENCY 0.0 5.0E9;
TIMER STTIME PERIODIC 25 99999 25;
STATISTICS STTIME;
TIMER PHTIME PERIODIC 1000 6000 1000;
C PARTICLE PLOTS
PHASESPACE PHTIME AXES X1 X2
      AXIS X 0.05 0.50 0.05
      AXIS Y 0.0 0.20 0.05
      SPECIES ALL SELECT TAG;
PHASESPACE PHTIME AXES X2 P2
      AXIS X 0.00 0.20 0.05
      AXIS Y -1.0E9 1.0E9 0.25E9
      SPECIES ALL SELECT TAG;
```

```
PHASESPACE PHTIME AXES X1 P1
        AXIS X 0.05 0.50 0.05
        AXIS Y -1.0E9 1.0E9 0.25E9
        SPECIES ALL SELECT TAG;
C DIODE VOLTAGE AND FIELDS
OBSERVE FIELD E1 218 41 218 41 FFT 5 WINDOW FREQUENCY 0.0 5.0E9;
OBSERVE FIELD E2 218 41 218 41 FFT 5 WINDOW FREQUENCY 0.0 5.0E9;
OBSERVE FIELD B3 218 41 218 41 FFT 5 WINDOW FREQUENCY 0.0 5.0E9;
C OUTPUT POWER WAVE
OBSERVE POYNTING ALL ANTI-ALIGN 218 2 218 42;
OBSERVE POYNTING TM ANTI-ALIGN 218 2 218 42;
OBSERVE POYNTING TE ANTI-ALIGN 218 2 218 42;
VECTOR PHTIME FIELD E1 E2
                NUMBER 20 20
                SCALE LINEAR
                AXIS X 0.05 0.5 0.075
                AXIS Y 0.0 0.2 0.0333;
OUTPUT COLOR;
OUTPUT SYSTEM TEST24.PLT GPRINT3;
DUMP NAME "TEST24";
DUMP FORMAT ASCII;
DUMP TYPE OBSERVE;
DUMP TYPE PHASESPACE;
START;
STOP;
```

Simulation Input Deck With Bipolar Flow and Small Collection Rod

```
TITLE "COAXIAL VIRCATOR MODEL WITH LONG ANODE, BIPOLAR FLOW
AND SMALL ROD";
SYSTEM CYLINDER-THETA;
X1GRID FUNCTION 226 2 0 8 10.0E-3 50.0E-3
                152 2.22E-3 337.44E-3
                10 2.22E-3 58.0E-3
                54 10E-3 540.0E-3;
X2GRID FUNCTION 98 2 0 10 4E-3 31.825E-3
          56 2.22E-3 124.32E-3
          30 2.22E-3 233.9E-3;
SYMMETRY AXIAL ALIGN 2 2 226 2;
DIAGNOSE COURANT 1 0 0;
FIELDS ALL HI-Q 3000 5.0E-12;
CONDUCTOR OUTER1 ANTI-ALIGN 2 98
                98 98
                98 65
                46 65
                44 63
                44 59
                46 57
                81 57;
CONDUCTOR EMSURF ANTI-ALIGN 81 57
                133 57;
CONDUCTOR OUTER2 ANTI-ALIGN 133 57
                144 57
                159 42
                226 42;
CONDUCTOR INNER1 ALIGN 2 93
                10 93
                10 55
                19 55
                31 43
                82 43
                82 5
                110 5
                113 2;
CONDUCTOR INNER2 ALIGN 124 42
                127 42
                128 41
                128 39
                125 39
                124 40
                124 42;
```

```
MATERIAL SS304 MASS 26 55.847 7.87E3;
FOIL SS304 1E-6 82 42
        124 42;
DISPLAY REAL 0.0 1.0 0.0 0.5;
LOOKBACK FIELDS ALL 1.23 1.0 ANTI-ALIGN 226 2 226 42.
C CHANGE –400 TO –300 FOR THE LOW VOLTAGE CASE
FUNCTION "VOFT(T)=-400E3*TANH(0.5E9*T)";
FUNCTION "RADIAL(X)=1.0/X";
VOLTAGE FIELDS TM VOFT RADIAL 1.0 0.0 1.0 ALIGN 2 93 2 98;
EMISSION ELECTRNS ELECTRON 5 1
        FIELD 1 0.9E7 0.0 0.0 0.0
        SPACING RANDOM 1.0E-5 RANDOM
        GAMMAV 1E6;
EMIT ELECTRNS EMSURF;
FUNCTION "STEP(T,X1,X2)=4.0*MAX(STEP(ABS(OBS1),0.0)-0.75, 0.0)";
EMISSION ANEMT PROTON 1 2
        FIELD STEP 0.0 0.0 0.0 0.0
        SPACING RANDOM 1.0E-5 RANDOM
        GAMMAV 1E6;
EMIT ANEMT SS304FOIL;
KINEMATICS ELECTRON 1 YES NO YES EM 1 1;
KINEMATICS PROTON 1 YES NO YES EM 1 1;
FORCES 0.5 1.0 1.0;
CURRENTS LCC NO NO 0.0 1.0;
TAGGING 0.125;
TIMER FOR_FLUX PERIODIC 0 99999 1;
FLUX ELECRNT FOR_FLUX ELECTRON
        INDICES ANTI-ALIGN 82 42 124 42;
OBSERVE FLUX ELECRNT CURRENT;
FLUX TEST FOR_FLUX ELECTRON
        INDICES ANTI-ALIGN 82 55 124 55;
C DIODE CURRENT MEASUREMENT
OBSERVE FLUX TEST CURRENT;
OBSERVE FIELD E2 2 93 2 98 FFT 5 WINDOW FREQUENCY 0.0 5.0E9;
OBSERVE FIELD B3 5 95 5 95 FFT 5 WINDOW FREQUENCY 0.0 5.0E9;
TIMER STTIME PERIODIC 25 99999 25;
STATISTICS STTIME;
TIMER PHTIME PERIODIC 1000 6000 1000;
C PARTICLE PLOTS
PHASESPACE PHTIME AXES X1 X2
      AXIS X 0.05 0.50 0.05
      AXIS Y 0.0 0.20 0.05
      SPECIES ALL SELECT TAG;
PHASESPACE PHTIME AXES X2 P2
      AXIS X 0.00 0.20 0.05
```

```
        AXIS Y -1.0E9 1.0E9 0.25E9
        SPECIES ALL SELECT TAG;
PHASESPACE PHTIME AXES X1 P1
        AXIS X 0.05 0.50 0.05
        AXIS Y -1.0E9 1.0E9 0.25E9
        SPECIES ALL SELECT TAG;
C DIODE VOLTAGE AND FIELDS
OBSERVE FIELD E1 218 41 218 41 FFT 5 WINDOW FREQUENCY 0.0 5.0E9;
OBSERVE FIELD E2 218 41 218 41 FFT 5 WINDOW FREQUENCY 0.0 5.0E9;
OBSERVE FIELD B3 218 41 218 41 FFT 5 WINDOW FREQUENCY 0.0 5.0E9;
C OUTPUT POWER WAVE
OBSERVE POYNTING ALL ANTI-ALIGN 218 2 218 42;
OBSERVE POYNTING TM ANTI-ALIGN 218 2 218 42;
OBSERVE POYNTING TE ANTI-ALIGN 218 2 218 42;
VECTOR PHTIME FIELD E1 E2
                NUMBER 20 20
                SCALE LINEAR
                AXIS X 0.05 0.5 0.075
                AXIS Y 0.0 0.2 0.0333;
OUTPUT COLOR;
OUTPUT SYSTEM TEST26.PLT GPRINT3;
DUMP NAME "TEST26";
DUMP FORMAT ASCII;
DUMP TYPE OBSERVE;
DUMP TYPE PHASESPACE;
START;
STOP;
```

Simulation Input Deck With Bipolar Flow and Large Collection Rod

```
TITLE "COAXIAL VIRCATOR MODEL WITH LONG ANODE, BIPOLAR FLOW
AND LARGE ROD";
SYSTEM CYLINDER-THETA;
X1GRID FUNCTION 226 2 0 8 10.0E-3 50.0E-3
                152 2.22E-3 337.44E-3
                10 2.22E-3 58.0E-3
                54 10E-3 540.0E-3;
X2GRID FUNCTION 98 2 0 10 4E-3 31.825E-3
          56 2.22E-3 124.32E-3
          30 2.22E-3 233.9E-3;
SYMMETRY AXIAL ALIGN 2 2 226 2;
DIAGNOSE COURANT 1 0 0;
FIELDS ALL HI-Q 3000 5.0E-12;
CONDUCTOR OUTER1 ANTI-ALIGN 2 98
                98 98
                98 65
                46 65
                44 63
                44 59
                46 57
                81 57;
CONDUCTOR EMSURF ANTI-ALIGN 81 57
                133 57;
CONDUCTOR OUTER2 ANTI-ALIGN 133 57
                144 57
                159 42
                226 42;
CONDUCTOR INNER1 ALIGN 2 93
                10 93
                10 55
                19 55
                31 43
                82 43
                82 10
                105 10
                124 2;
CONDUCTOR INNER2 ALIGN 124 42
                127 42
                128 41
                128 39
                125 39
                124 40
                124 42;
```

```
MATERIAL SS304 MASS 26 55.847 7.87E3;
FOIL SS304 1E-6 82 42
        124 42;
DISPLAY REAL 0.0 1.0 0.0 0.5;
LOOKBACK FIELDS ALL 1.23 1.0 ANTI-ALIGN 226 2 226 42.
C CHANGE –400 TO –300 FOR THE LOW VOLTAGE CASE
FUNCTION "VOFT(T)=-400E3*TANH(0.5E9*T)";
FUNCTION "RADIAL(X)=1.0/X";
VOLTAGE FIELDS TM VOFT RADIAL 1.0 0.0 1.0 ALIGN 2 93 2 98;
EMISSION ELECTRNS ELECTRON 5 1
        FIELD 1 0.9E7 0.0 0.0 0.0
        SPACING RANDOM 1.0E-5 RANDOM
        GAMMAV 1E6;
EMIT ELECTRNS EMSURF;
FUNCTION "STEP(T,X1,X2)=4.0*MAX(STEP(ABS(OBS1),0.0)-0.75, 0.0)";
EMISSION ANEMT PROTON 1 2
        FIELD STEP 0.0 0.0 0.0 0.0
        SPACING RANDOM 1.0E-5 RANDOM
        GAMMAV 1E6;
EMIT ANEMT SS304FOIL;
KINEMATICS ELECTRON 1 YES NO YES EM 1 1;
KINEMATICS PROTON 1 YES NO YES EM 1 1;
FORCES 0.5 1.0 1.0;
CURRENTS LCC NO NO 0.0 1.0;
TAGGING 0.125;
TIMER FOR_FLUX PERIODIC 0 99999 1;
FLUX ELECRNT FOR_FLUX ELECTRON
        INDICES ANTI-ALIGN 82 42 124 42;
OBSERVE FLUX ELECRNT CURRENT;
FLUX TEST FOR_FLUX ELECTRON
        INDICES ANTI-ALIGN 82 55 124 55;
C DIODE CURRENT MEASUREMENT
OBSERVE FLUX TEST CURRENT;
OBSERVE FIELD E2 2 93 2 98 FFT 5 WINDOW FREQUENCY 0.0 5.0E9;
OBSERVE FIELD B3 5 95 5 95 FFT 5 WINDOW FREQUENCY 0.0 5.0E9;
TIMER STTIME PERIODIC 25 99999 25;
STATISTICS STTIME;
TIMER PHTIME PERIODIC 1000 6000 1000;
C PARTICLE PLOTS
PHASESPACE PHTIME AXES X1 X2
    AXIS X 0.05 0.50 0.05
    AXIS Y 0.0 0.20 0.05
    SPECIES ALL SELECT TAG;
PHASESPACE PHTIME AXES X2 P2
    AXIS X 0.00 0.20 0.05
```

```
        AXIS Y -1.0E9 1.0E9 0.25E9
        SPECIES ALL SELECT TAG;
PHASESPACE PHTIME AXES X1 P1
        AXIS X 0.05 0.50 0.05
        AXIS Y -1.0E9 1.0E9 0.25E9
        SPECIES ALL SELECT TAG;
C DIODE VOLTAGE AND FIELDS
OBSERVE FIELD E1 218 41 218 41 FFT 5 WINDOW FREQUENCY 0.0 5.0E9;
OBSERVE FIELD E2 218 41 218 41 FFT 5 WINDOW FREQUENCY 0.0 5.0E9;
OBSERVE FIELD B3 218 41 218 41 FFT 5 WINDOW FREQUENCY 0.0 5.0E9;
C OUTPUT POWER WAVE
OBSERVE POYNTING ALL ANTI-ALIGN 218 2 218 42;
OBSERVE POYNTING TM ANTI-ALIGN 218 2 218 42;
OBSERVE POYNTING TE ANTI-ALIGN 218 2 218 42;
VECTOR PHTIME FIELD E1 E2
                NUMBER 20 20
                SCALE LINEAR
                AXIS X 0.05 0.5 0.075
                AXIS Y 0.0 0.2 0.0333;
OUTPUT COLOR;
OUTPUT SYSTEM TEST28.PLT GPRINT3;
DUMP NAME "TEST28";
DUMP FORMAT ASCII;
DUMP TYPE OBSERVE;
DUMP TYPE PHASESPACE;
START;
STOP;
```

Simulation Input Deck With Bipolar Flow and a Hole on Axis

```
TITLE "COAXIAL VIRCATOR MODEL WITH LONG ANODE, BIPOLAR FLOW
AND A HOLE ON AXIS";
SYSTEM CYLINDER-THETA;
X1GRID FUNCTION 226 2 0 8 10.0E-3 50.0E-3
                152 2.22E-3 337.44E-3
                10 2.22E-3 58.0E-3
                54 10E-3 540.0E-3;
X2GRID FUNCTION 98 2 0 10 4E-3 31.825E-3
          56 2.22E-3 124.32E-3
          30 2.22E-3 233.9E-3;
SYMMETRY AXIAL ALIGN 2 2 226 2;
DIAGNOSE COURANT 1 0 0;
FIELDS ALL HI-Q 3000 5.0E-12;
CONDUCTOR OUTER1 ANTI-ALIGN 2 98
                98 98
                98 65
                46 65
                44 63
                44 59
                46 57
                81 57;
 CONDUCTOR EMSURF ANTI-ALIGN 81 57
                133 57;
CONDUCTOR OUTER2 ANTI-ALIGN 133 57
                144 57
                159 42
                226 42;
CONDUCTOR INNER1 ALIGN 2 93
                10 93
                10 55
                19 55
                31 43
                82 43
                82 5
                73 5
                73 2;
CONDUCTOR INNER2 ALIGN 124 42
                127 42
                128 41
                128 39
                125 39
                124 40
                124 42;
```

```
MATERIAL SS304 MASS 26 55.847 7.87E3;
FOIL SS304 1E-6 82 42
        124 42;
DISPLAY REAL 0.0 1.0 0.0 0.5;
LOOKBACK FIELDS ALL 1.23 1.0 ANTI-ALIGN 226 2 226 42;
C CHANGE –400 TO –300 FOR THE LOW VOLTAGE CASE
FUNCTION "VOFT(T)=-400E3*TANH(0.5E9*T)";
FUNCTION "RADIAL(X)=1.0/X";
VOLTAGE FIELDS TM VOFT RADIAL 1.0 0.0 1.0 ALIGN 2 93 2 98;
EMISSION ELECTRNS ELECTRON 5 1
        FIELD 1 0.9E7 0.0 0.0 0.0
        SPACING RANDOM 1.0E-5 RANDOM
        GAMMAV 1E6;
EMIT ELECTRNS EMSURF;
FUNCTION "STEP(T,X1,X2)=4.0*MAX(STEP(ABS(OBS1),0.0)-0.75, 0.0)";
EMISSION ANEMT PROTON 1 2
        FIELD STEP 0.0 0.0 0.0 0.0
        SPACING RANDOM 1.0E-5 RANDOM
        GAMMAV 1E6;
EMIT ANEMT SS304FOIL;
KINEMATICS ELECTRON 1 YES NO YES EM 1 1;
KINEMATICS PROTON 1 YES NO YES EM 1 1;
FORCES 0.5 1.0 1.0;
CURRENTS LCC NO NO 0.0 1.0;
TAGGING 0.125;
TIMER FOR_FLUX PERIODIC 0 99999 1;
FLUX ELECRNT FOR_FLUX ELECTRON
        INDICES ANTI-ALIGN 82 42 124 42;
OBSERVE FLUX ELECRNT CURRENT;
FLUX TEST FOR_FLUX ELECTRON
        INDICES ANTI-ALIGN 82 55 124 55;
C DIODE CURRENT MEASUREMENT
OBSERVE FLUX TEST CURRENT;
OBSERVE FIELD E2 2 93 2 98 FFT 5 WINDOW FREQUENCY 0.0 5.0E9;
OBSERVE FIELD B3 5 95 5 95 FFT 5 WINDOW FREQUENCY 0.0 5.0E9;
TIMER STTIME PERIODIC 25 99999 25;
STATISTICS STTIME;
TIMER PHTIME PERIODIC 1000 6000 1000;
C PARTICLE PLOTS
PHASESPACE PHTIME AXES X1 X2
    AXIS X 0.05 0.50 0.05
    AXIS Y 0.0 0.20 0.05
    SPECIES ALL SELECT TAG;
PHASESPACE PHTIME AXES X2 P2
    AXIS X 0.00 0.20 0.05
```

```
        AXIS Y -1.0E9 1.0E9 0 25E9
        SPECIES ALL SELECT TAG;
PHASESPACE PHTIME AXES X1 P1
        AXIS X 0.05 0.50 0.05
        AXIS Y -1.0E9 1.0E9 0.25E9
        SPECIES ALL SELECT TAG;
C DIODE VOLTAGE AND FIELDS
OBSERVE FIELD E1 218 41 218 41 FFT 5 WINDOW FREQUENCY 0.0 5.0E9;
OBSERVE FIELD E2 218 41 218 41 FFT 5 WINDOW FREQUENCY 0.0 5.0E9;
OBSERVE FIELD B3 218 41 218 41 FFT 5 WINDOW FREQUENCY 0.0 5.0E9;
C OUTPUT POWER WAVE
OBSERVE POYNTING ALL ANTI-ALIGN 218 2 218 42;
OBSERVE POYNTING TM ANTI-ALIGN 218 2 218 42;
OBSERVE POYNTING TE ANTI-ALIGN 218 2 218 42;
VECTOR PHTIME FIELD E1 E2
                NUMBER 20 20
                SCALE LINEAR
                AXIS X 0.05 0.5 0.075
                AXIS Y 0.0 0.2 0.0333;
OUTPUT COLOR;
OUTPUT SYSTEM TEST29.PLT GPRINT3;
DUMP NAME "TEST29";
DUMP FORMAT ASCII;
DUMP TYPE OBSERVE;
DUMP TYPE PHASESPACE;
START;
STOP;
```

Simulation Input Deck With Bipolar Flow and Narrow Strip

```
TITLE "COAXIAL VIRCATOR MODEL WITH LONG ANODE AND BIPOLAR
FLOW
AND SMALL STRIP";
SYSTEM CYLINDER-THETA;
X1GRID FUNCTION 226 2 0 8 10.0E-3 50.0E-3
                152 2.22E-3 337.44E-3
                10 2.22E-3 58.0E-3
                54 10E-3 540.0E-3;
X2GRID FUNCTION 98 2 0 10 4E-3 31.825E-3
          56 2.22E-3 124.32E-3
          30 2.22E-3 233.9E-3;
SYMMETRY AXIAL ALIGN 2 2 226 2;
DIAGNOSE COURANT 1 0 0;
FIELDS ALL HI-Q 3000 5.0E-12;
CONDUCTOR OUTER1 ANTI-ALIGN 2 98
                98 98
                98 65
                46 65
                44 63
                44 59
                46 57
                103 57;
CONDUCTOR EMSURF ANTI-ALIGN 103 57
                117 57;
CONDUCTOR OUTER2 ANTI-ALIGN 117 57
                144 57
                159 42
                226 42;
CONDUCTOR INNER1 ALIGN 2 93
                10 93
                10 55
                19 55
                31 43
                82 43
                82 2;
CONDUCTOR INNER2 ALIGN 124 42
                127 42
                128 41
                128 39
                125 39
                124 40
                124 42;
CONDUCTOR INNER3 NONE 82 42
```

```
                103 42;
CONDUCTOR INNER4 NONE 117 42
                124 42;
MATERIAL SS304 MASS 26 55.847 7.87E3;
FOIL SS304 1E-6 103 42
        117 42;
DISPLAY REAL 0.0 1.0 0.0 0.5;
LOOKBACK FIELDS ALL 1.23 1.0 ANTI-ALIGN 226 2 226 42;
C CHANGE –475 TO –375 FOR THE LOW VOLTAGE CASE
FUNCTION "VOFT(T)=-475E3*TANH(0.5E9*T)";
FUNCTION "RADIAL(X)=1.0/X";
VOLTAGE FIELDS TM VOFT RADIAL 1.0 0.0 1.0 ALIGN 2 93 2 98;
EMISSION ELECTRNS ELECTRON 5 1
        FIELD 1 0.9E7 0.0 0.0 0.0
        SPACING RANDOM 1.0E-5 RANDOM
        GAMMAV 1E6;
EMIT ELECTRNS EMSURF;
FUNCTION "STEP(T,X1,X2)=4.0*MAX(STEP(ABS(OBS1),0.0)-0.75, 0.0)";
EMISSION ANEMT PROTON 1 2
        FIELD STEP 0.0 0.0 0.0 0.0
        SPACING RANDOM 1.0E-5 RANDOM
        GAMMAV 1E6;
EMIT ANEMT SS304FOIL;
KINEMATICS ELECTRON 1 YES NO YES EM 1 1;
KINEMATICS PROTON 1 YES NO YES EM 1 1;
FORCES 0.5 1.0 1.0;
CURRENTS LCC NO NO 0.0 1.0;
TAGGING 0.125;
TIMER FOR_FLUX PERIODIC 0 99999 1;
FLUX ELECRNT FOR_FLUX ELECTRON
        INDICES ANTI-ALIGN 82 42 124 42;
OBSERVE FLUX ELECRNT CURRENT;
FLUX TEST FOR_FLUX ELECTRON
        INDICES ANTI-ALIGN 82 55 124 55;
C DIODE CURRENT MEASUREMENT
OBSERVE FLUX TEST CURRENT;
OBSERVE FIELD E2 2 93 2 98 FFT 5 WINDOW FREQUENCY 0.0 5.0E9;
OBSERVE FIELD B3 5 95 5 95 FFT 5 WINDOW FREQUENCY 0.0 5.0E9;
TIMER STTIME PERIODIC 25 99999 25;
STATISTICS STTIME;
TIMER PHTIME PERIODIC 1000 6000 1000;
C PARTICLE PLOTS
PHASESPACE PHTIME AXES X1 X2
    AXIS X 0.05 0.50 0.05
    AXIS Y 0.0 0.20 0.05
```

```
        SPECIES ALL SELECT TAG;
PHASESPACE PHTIME AXES X2 P2
        AXIS X 0.00 0.20 0.05
        AXIS Y -1.0E9 1.0E9 0.25E9
        SPECIES ALL SELECT TAG;
PHASESPACE PHTIME AXES X1 P1
        AXIS X 0.05 0.50 0.05
        AXIS Y -1.0E9 1.0E9 0.25E9
        SPECIES ALL SELECT TAG;
C DIODE VOLTAGE AND FIELDS
OBSERVE FIELD E1 218 41 218 41 FFT 5 WINDOW FREQUENCY 0.0 5.0E9;
OBSERVE FIELD E2 218 41 218 41 FFT 5 WINDOW FREQUENCY 0.0 5.0E9;
OBSERVE FIELD B3 218 41 218 41 FFT 5 WINDOW FREQUENCY 0.0 5.0E9;
C OUTPUT POWER WAVE
OBSERVE POYNTING ALL ANTI-ALIGN 218 2 218 42;
OBSERVE POYNTING TM ANTI-ALIGN 218 2 218 42;
OBSERVE POYNTING TE ANTI-ALIGN 218 2 218 42;
VECTOR PHTIME FIELD E1 E2
                NUMBER 20 20
                SCALE LINEAR
                AXIS X 0.05 0.5 0.075
                AXIS Y 0.0 0.2 0.0333;
OUTPUT COLOR;
OUTPUT SYSTEM STRIP6.PLT GPRINT3;
DUMP NAME "STRIP6";
DUMP FORMAT ASCII;
DUMP TYPE OBSERVE;
DUMP TYPE PHASESPACE;
START;
STOP;
```